Iodine stabilized diode laser using Noise-Immune Cavity-Enhanced Optical Heterodyne Molecular Spectroscopy for the practical realisation of the meter at 633 nm

Von der QUEST-Leibniz-Forschungsschule

der Gottfried Wilhelm Leibniz Universität Hannover

zur Erlangung des Grades

Doktor der Naturwissenschaften

Dr. rer. nat.

genehmigte Dissertation von

M. Sc. Florian Krause

2022

Referent   PD Dr. Christian Lisdat (Leibniz Universität Hannover)

Korreferent   Prof. Dr. Piet O. Schmidt (Leibniz Universität Hannover)

Korreferent   Assoc. Prof. Dr. Jörg H. Müller (University of Copenhagen)

Tag der Promotion: 28.03.2022

Abstract

In this thesis a new practical realization of the meter at a wavelength of 633 nm with a diode laser stabilized on iodine is investigated, with the aim of replacing the old technology of He-Ne lasers with more effective diode lasers. The frequency of an external cavity diode laser is stabilized to the Doppler-free hyperfine transitions of iodine ($^{127}I_2$) using noise-immune cavity-enhanced optical heterodyne molecular spectroscopy (NICE-OHMS) technique. The performance of the system was investigated in comparison to a primary Cs atomic clock via a frequency comb. The diode laser is stabilized by using the NICE-OHMS method to a 14 cm external cavity containing a 10 cm long iodine cell. It achieves a short time frequency instability of $1.4 \cdot 10^{-12}$ for an averaging time of 1 s, an improvement by a factor of four compared to an iodine stabilized He-Ne laser, which is widely used as practical realization of the meter. The uncertainty of the NICE-OHMS system is 28 kHz. Practical experiments as well as simulations are performed to identify effects that influence the frequency of the laser. To replace two-mode or Zeeman-stabilized He-Ne lasers, also a shoe box size diode laser system stabilized to Doppler broadened iodine lines is investigated. This system, which uses a 3 cm iodine cell, covers a frequency range of several 100 GHz, and achieves an output power of 5 mW. It automatically stabilizes to iodine lines and has a frequency instability of $2 \cdot 10^{-10}$ for averaging times of 1 s, which is adequate for industrial interferometry applications.

Keywords:

- diode laser, optical cavity, Pound-Drever-Hall

- NICE-OHMS, fm-spectroscopy, saturation spectroscopy

- iodine, SI-unit meter

Contents

Chapter 1

Introduction

At the end of the 18th century, the length SI unit meter was defined for the first time to introduce a uniform system of measurement for European trade. The meter was supposed to be traced back to the natural constant of the earth's meridian. For this purpose, a section of the Paris meridian between Dunkirk and Barcelona was measured by means of elaborate trigonometric measurements at the time of the French Revolution. In 1799 the ten-millionth part of the earth's meridian was then defined as one meter in the form of a gauge block made of platinum, which is called "mètre des Archives" [1].

Over time it turned out that the circumference of the earth did not represent a real constant and the "mètre des Archives" was not sufficiently accurate any more for the accuracy of the contemporary measuring techniques. For this reason, in 1889, several x-shaped copies based on the "mètre des Archives" were made of a better platinum iridium alloy. Thus one meter corresponded to the distance of the center lines at 0 °C of the "mètre des Archives" [2]. Until 1960, the meter was defined on the basis of these prototypes.

The first ideas on a meter convention based on light came in 1887 from Michelson, using optical interferometers to measure units of length. Because of the short wavelength, visible light provides a much higher resolution and can be transferred to scales using interferometry.

In 1960, the meter was redefined to the natural constant of an atomic transition using a krypton vapor lamp. The length of a meter corresponded to $1\,650\,763.73$ times of the wavelength of the light emitted by a ^{86}Kr atom [3].

The development of the laser resulted in a new light source with high spatial and temporal coherence, which is excellent for the application of interferometry. The possibility of stabilization on atomic/molecular transitions enabled the development of

frequency stable lasers with high reproducibility and stability, that led to a further redefinition of the meter. To avoid the pitfall of choosing a certain transition that soon would be replaced by an even better one, it was was decided to define the meter by fitting a fundamental constant. Since 1983 the length of a meter corresponds to the length which light in vacuum travels within a time of $1/(299\,792\,458)$ s [4], thus relating the meter to the definition of the second via defined speed of light $c_0 = 299\,792\,458\,\frac{\text{m}}{\text{s}}$. According to the "Mise en Pratique of the definition of the meter" [5] the meter can be realized on the basis of three possibilities:

- by means of the defined vacuum speed of light c_0 and a measurement of the time t, which light needs in vacuum for a distance: $L = c_0 \cdot t$,

- by determining the wavelength λ of a laser by measuring the optical frequency ν: $\lambda = c_0/\nu$,

- by means of a recommended reference wavelength or reference frequency of an atomic/molecular transition (18 different atomic/molecular absorbing transition including the iodine stabilized He-Ne laser at 633 nm with $2.5 \cdot 10^{-11}$ uncertainty and two radiations of spectral lamps) [4].

Especially the third possibility makes it possible to practical realize the length of the meter without having to resort to complex measurements of the speed of light or frequency of a laser, if used carefully.

In 2019 the meter definition was reworded to [6]:

$$1\,\text{m} = \frac{9\,192\,631\,770}{299\,792\,458}\frac{c_0}{\Delta\nu_{\text{Cs}}} \tag{1.1}$$

with $\Delta\nu_{\text{Cs}} = 9\,192\,631\,770\,\text{Hz}$ defined hyperfine transition of Cs-Atom and $c_0 = 299\,792\,458\,\frac{\text{m}}{\text{s}}$ defined vacuum light speed. However, thus did not change the physical content of the 1983 definition.

Iodine stabilized helium-neon (He-Ne) lasers are a widely used length standard at the wavelength of 633 nm [7, 8, 9]. Because of the simple and reliable technique, He-Ne lasers with the wavelength of 633 nm are used in the field of interferometry [10, 11] and metrology [4] even nowadays [12]. A frequency instability of $2.1 \cdot 10^{-11}$ at averaging times of 1 s and an uncertainty of 10 kHz can be achieved with iodine stabilized He-Ne lasers [13]. However, there are several problems with the use of He-Ne lasers. Firstly, the know-how of the production of suitable gas tubes and the maintenance is lost over time. In addition, due to the design of He-Ne lasers, higher powers are not possible

with a compact construction. Likewise, He-Ne lasers can only be tuned in a small frequency range.

A promising alternative to He-Ne lasers are diode lasers (DL) stabilized to an atomic/molecular reference [14]. In the wavelength range of 633 nm, iodine is used as a reference [4, 15, 16]. Diode lasers are more compact, more flexible in wavelength and more powerful than He-Ne lasers. Stabilized by saturation spectroscopy on hyperfine components of the iodine line P(33)6-3, DL achieved a frequency instability of $7 \cdot 10^{-12}$ to $5 \cdot 10^{-11}$ with an averaging time of 1 s and an uncertainty of some ten kHz [17].

The project "Frequenzstabilisierte Diodenlaser der nächsten Generation für Metrologie und Life Science" (FinDLinNG) was funded by the german Federal Ministry of Education and Research (BMBF), completed after 3 years and had addressed precisely this approach. The aim of the project was to replace the current technology of He-Ne lasers with frequency-stabilized diode lasers. Within the project diode laser of the wavelength 633 nm were developed in different scales and instabilities. Small compact hand-size systems, which are used directly applied in the industry for length measurements [18, 19]. A laser system the size of a shoe box for use in the laboratory (see chapter 4), which was evaluated in the course of this thesis. However, the highest frequency stability in this project was achieved by the system of this thesis, based on a DL stabilized by an external iodine resonator and the noise-immune cavity enhanced optical-heterodyne molecular spectrometry (NICE-OHMS) sensitive absorption method.

The NICE-OHMS method was developed in the late 1990s by John Hall, Jun Ye and Long-Sheng Ma at JILA to very precisely detect weak and spectral narrow transitions at the shot-noise limit [20, 21, 22]. The combination of power enhancement and increased effective absorption length by a cavity and simultaneous use of frequency modulation spectroscopy was exploited. After only laser systems with a narrow tuning frequency range were used at the beginning, attempts were made in the following years to establish NICE-OHMS with DL with a broader tunable frequency range [23].

The aim of this work is to investigate a possible alternative of iodine-stabilized He-Ne laser with the wavelength of 633 nm as a practical realization of the meter. The wavelength 633 nm was chosen to allow a one-to-one replacement and integration into current interferometer setups. For the first time the NICE-OHMS method is used with a wavelength of 633 nm to stabilize a DL onto hyperfine lines of iodine transitions. For this purpose, the DL is used with an external resonator with an integrated iodine

cell. The advantages of NICE-OHMS technique compared to iodine stabilized He-Ne lasers are manifold. By the combination of a cavity and frequency modulation technique, the noise of the laser diode can be suppressed. DL also allows higher output powers with smaller and more compact designs than He-Ne lasers. The rugged set up of cavity enhancement spectroscopy also eliminates the alignment sensitivities of free space saturation spectroscopy.

The experimental results are compared to simulation of the iodine spectra and the NICE-OHMS signals. Based on these simulations, it is then possible to transfer frequency deviations for other possible iodine lines.

Chapter 2 describes both the theoretical basis of iodine spectra and the NICE-OHMS technique, as well as the setup of the simulations performed in this thesis. In the 3rd chapter, the experimental setups for measuring the frequency of the laser referencing to an iodine-stabilized He-Ne laser or to Cs atomic clocks using a frequency comb are presented. In the following chapter 4, the performance of a DL stabilized on Doppler broadened iodine lines (Toptica beta demonstrator) that shall be be able to replace conventional He-Ne lasers without iodine reference is investigated. In the last chapter 5, the construction of a DL stabilized on Doppler free hyperfine components of iodine transitions using the NICE-OHMS method is presented in detail. The frequency instability over time and the accuracy are investigated. Subsequently, the experimentally obtained data are analyzed and examined for systematic effects that influence the frequency of the DL. These results are compared with theoretical simulations. Finally, a short conclusion and an outlook with possible optimizations of the system are given.

Chapter 2

Theoretical Description and Simulation of NICE-OHMS

2.1 Iodine

To stabilize laser frequency, fundamental references in the form of atomic or molecular transitions are used. In the optical wavelength range of 633 nm iodine $^{127}I_2$ vapor is used as reference standard [13]. Iodine at room temperature is a bluish black solid that volatilizes into blue violet gas. The isotope ^{127}I is the only natural occurring and the heaviest stable halogen [24].

2.1.1 Energy Structure

The spectroscopic transitions of iodine $^{127}I_2$ studied in this work are transitions between roto-vibrational levels between different electronic states of the molecule. Figure 2.1 shows the potential scheme of the lower energetic states of iodine. The potential energy is displayed over the distance of the two iodine nuclear. Transitions between the ground state X to and the electronically excited state B are in the visible range of 500-700 nm. These transitions have been studied for decades and thus have been carefully analyzed. $^1\Sigma_{0g}^+$ describes the electronic ground state X that correlates to two atoms in the electrical ground state configuration ($^2P_{3/2}$) at large inter nuclear distance. The next higher state with an attractive potential $^3\Pi_{0u}^+$ is labeled B and correlates to one of the atoms in the electronic ground state $^2P_{3/2}$ and the other in the excited state $^2P_{1/2}$. The exact theoretical relations between the molecular structure and the energy structure can be found in common textbooks like [25]. In the case of

the iodine molecule $^{127}I_2$ a detailed description of the energy structure is given in [26], to which this work refers.
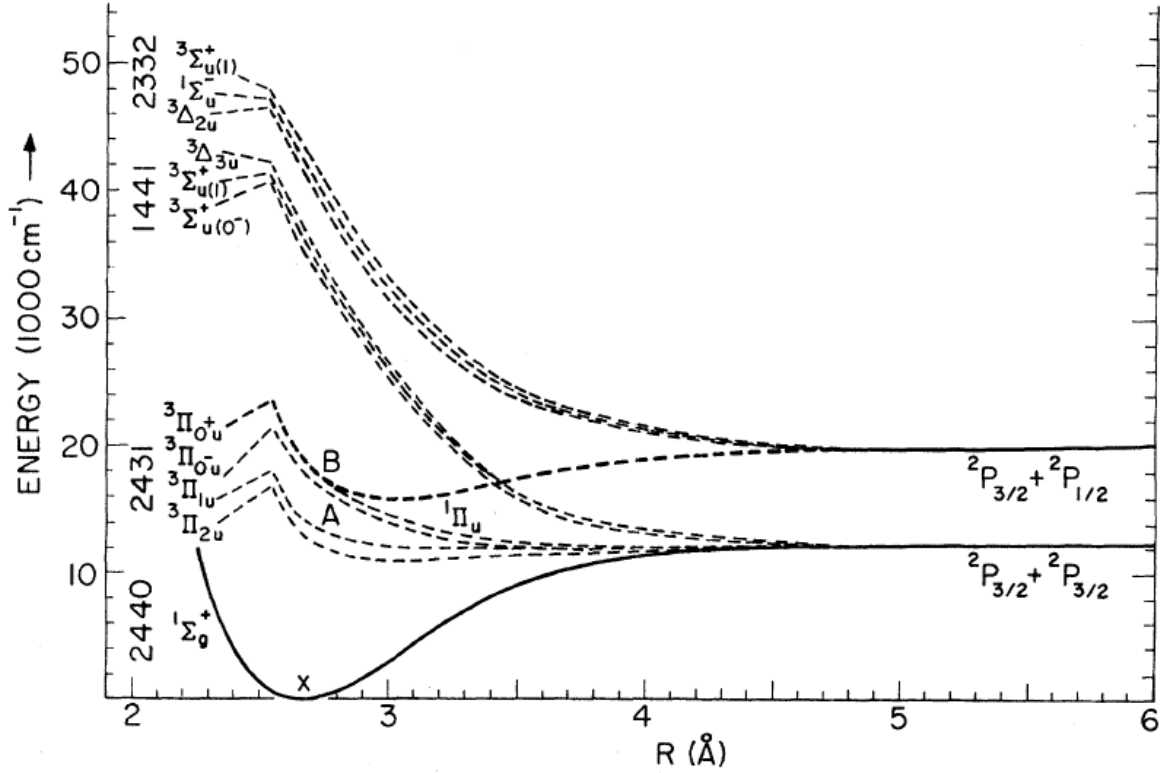
Figure 2.1: Thermal scheme of the energetic states of iodine $^{127}I_2$. In this work, transitions between the electronically excited molecule state B and ground state X are of concern. [27]

2.1.2 Rotation-Vibration Lines

Due to the large number of possible combinations of rotation and vibration states, several thousand different transitions are possible [28]. To calculate the energy of the individual molecular states, the semi classical Dunham approximation is used [29]. Thereby, data obtained from molecular spectroscopy are used to numerically approximate the molecular constants. The following notation is introduced to describe the energy levels:

- $E_X(v'', J'')$: energy of the ground level,

- $E_B(v', J')$: energy of the exited level,

- J is the rotational quantum number,

- v is the vibrational quantum number.

The selection rules for optical dipole transitions allow two types of rotations and vibrations transitions ($J'' - J' = \Delta J = \pm 1$), which follow the following notation:

- P transition: $\Delta J = +1$,

- R transition: $\Delta J = -1$.

This results in a notation of R/P(J')v'-v'' to describe the transitions. As an example, the following iodine transitions studied in this work are given:

- P(33)6-3   ($v'' = 3, J'' = 33$) $\rightarrow$ ($v' = 6, J' = 32$),

- R(127)11-5   ($v'' = 5, J'' = 127$) $\rightarrow$ ($v' = 11, J' = 128$).

The probability of a transition and thus the strength of the absorption line is determined by 3 factors [30]. The first factor depends on the occupation of the roto-vibrational level in the ground state and thus depends on the temperature. The second factor is the Hönl-London rotational line strength, which can be assumed to be constant for high J. The Franck-Condon factor (FCF) is the third factor and describes the transition probability between the vibrational levels based on the Franck-Condon principle. Thereby the FCF depends on the vibrational v and rotational J quantum number.

2.1.3 Hyperfine Structure

The electromagnetic interaction between the nuclei and the electron shell leads to the hyperfine splitting of the roto-vibrational energie levels [31]. Here the total angular momentum $\vec{F}$ of the molecule is given by the sum of angular momentum $\vec{J}$ of the molecule electrons and nucleus rotation spin $\vec{I}$ [26]:

$$\vec{F} = \vec{J} + \vec{I} \tag{2.1}$$

The nuclei of $^{127}I_2$ with a spin of $I = 5/2$ couple to a total spin of [32]:

$$\vec{I} = \vec{I_1} + \vec{I_2}, \tag{2.2}$$

which can take values of $I = 0, 1, 2, 3, 4, 5$. Additionally, due to the half-integer spin of the nucleus, the following selection rules apply:

- odd J'' couple with odd total spin ($I = 5, 3, 1$) in the ground X $^1\Sigma_{0g}^+$ state,

- even J' couple with odd total spin ($I = 5, 3, 1$) in the excited B $^3\Pi_{0u}^+$ state,

- even J'' couple with even total spin ($I = 4, 2, 0$) in the ground X $^1\Sigma_{0g}^+$ state,

- odd J' couple with even total spin ($I = 4, 2, 0$) in the excited B $^3\Pi_{0u}^+$ state.

Duo to the interaction for $J > I$, each roto-vibrational level splits into $N = (2I + 1)$ hyperfine level. When the angular momentum is much larger than the nuclear spin ($J \gg I$), which is the case for the investigated lines in this work, the following additional selection rules apply [27]:

- $\Delta J = \pm 1$,

- $\Delta I = 0$,

- $\Delta F = \Delta J$.

Thus each roto-vibrational line is split into the following number of hyperfine transitions:

- even J'' has 15 HFS components,

- odd J'' has 21 HFS components.

2.1.4 Simulation of Hyperfine Spectrum

This section introduces the "Iodine Spectrum" program [33], which can be used to simulate the frequencies and intensities of a variety of possible iodine transitions. Using these data, simulations of the absorption spectra of $^{127}I_2$ were performed in this work. The program uses precisely measured frequency data in the NIR range and measurements in the visible range known from the literature to calculate the rotational and vibrational levels and energies. The hyperfine splitting in a wide frequency range is calculated by means of an interpolation formula [34] for the four relevant hyperfine interactions:

- nuclear electric quadrupole (eqQ),

- nuclear spin-rotation (Csr),

- scalar part of the nuclear spin-spin interaction δ,

- tensorial part of the nuclear spin-spin interaction d.

It achieves a predictive uncertainty of $2\sigma < 30\,\mathrm{MHz}$ [35]. By entering the desired frequency range and temperature, the frequency and relative intensity of all the lines lying above a defined minimum intensity are calculated. For the calculation of the intensity of the absorption lines, as mentioned in 2.1.2, the occupation of the ground state as a function of temperature (Boltzman distribution), the Franck-Condon factors and the Hoenl-London factors are taken into account. As a result, the program provides a table listing the frequency and intensities for the respective rotational vibration lines and their hyperfine splitting. In table 2.1 are the frequencies ν_{IS} of the HFS components of the iodine line P(33)6-3 calculated with "Iodine Spectrum" compared to the absolute frequency ν_{BIPM} of the BIPM [13], that are based on optical frequency measurements.

The table shows that the calculated values differ from the experimentally determined values by less than 0.4 MHz. According to [34], the reported uncertainty of the individual HFS components is linear to the root of the rotational quantum number in the ground state $\sqrt{J''}$. It is also indicated that for $J'' = 0$ the frequency inaccuracy corresponds to approx. $\Delta\nu = \pm100\,\mathrm{kHz}$ and for $J'' = 140$ approx. $\Delta\nu = \pm1\,\mathrm{MHz}$. From this, the frequency inaccuracy $\Delta\nu$ as a function of the rotational quantum number for the frequencies determined by "Iodine Spectrum" is estimated as:

$$\Delta\nu \approx \frac{900\,\mathrm{kHz}}{\sqrt{140}} \cdot \sqrt{J''} + 100\,\mathrm{kHz} \tag{2.3}$$

This results in an uncertainty of $\Delta\nu \approx \pm0.5\,\mathrm{MHz}$ for the HFS components of line P(33), which is consistent with the deviation shown in Table 2.1.

Line	ν_{BIPM} / kHz	ν_{IS} / kHz	$(\nu_{\mathrm{BIPM}} - \nu_{\mathrm{IS}})$ / kHz
a	473 611 821 184	473 611 821 535	-351
b	473 611 799 204	473 611 799 559	-355
c	473 611 784 454	473 611 784 807	-353
d	473 611 702 956	473 611 703 305	-349
e	473 611 667 242	473 611 667 586	-344
f	473 611 641 872	473 611 642 208	-336
g	473 611 606 654	473 611 606 984	-330
h	473 611 557 596	473 611 557 939	-343
i	473 611 510 884	473 611 511 219	-335
j	473 611 473 830	473 611 474 152	-322
k	473 611 382 174	473 611 382 510	-336
l	473 611 367 974	473 611 368 303	-329
m	473 611 359 884	473 611 360 223	-339
n	473 611 334 110	473 611 334 430	-320
o	473 611 273 784	473 611 274 118	-334
p	473 611 227 188	473 611 227 514	-326
q	473 611 210 487	473 611 210 813	-326
r	473 611 160 684	473 611 160 987	-303
s	473 610 951 514	473 610 951 841	-327
t	473 610 926 120	473 610 926 434	-314
u	473 610 898 613	473 610 898 906	-293

Table 2.1: Listing of all hyperfine transitions of molecular iodine of the line P(33)6-3. The absolute frequency according to the BIPM ν_{BIPM} [13], the frequency ν_{IS} simulated with the "Iodine Spectrum" program, the difference of both $(\nu_{\mathrm{BIPM}} - \nu_{\mathrm{IS}})$ and the wavelength λ_{BIPM} calculated from the frequency ν_{BIPM} are given.

2.1.5 Saturation Pressure

The cells used in this work contained sufficient amount of iodine, that the iodine pressure is given as the saturation vapor pressure at the coldest point in the cell. The pressure can be easily changed or stabilized by controlling the temperature. Table 2.2 shows the measured vapor pressure for some temperatures.

p in Pa	0.133	1.33	13.33	133.33	1333.33
T in K	243	262	285	312	345

Table 2.2: Vapor pressure of molecular iodine I_2 for different temperatures by Honig [36].

Using these measured values, the Antoine equation (2.4) is used to approximate the saturation pressure p as a function of the temperature T [37].

$$p(T) = 10^{A - \frac{B}{C+T}} \tag{2.4}$$

From this approximation, the following fit parameters are obtained:

- $A = 12.155 \pm 0.062$,

- $B = (2989 \pm 45)\,\text{K}$,

- $C = (-14.0 \pm 1.9)\,\text{K}$.

Figure 2.2 shows graphically the fit function and the measured values of [36] in a wide temperature range around the room temperature of $T = 293\,\text{K}$ and agrees well with [38].
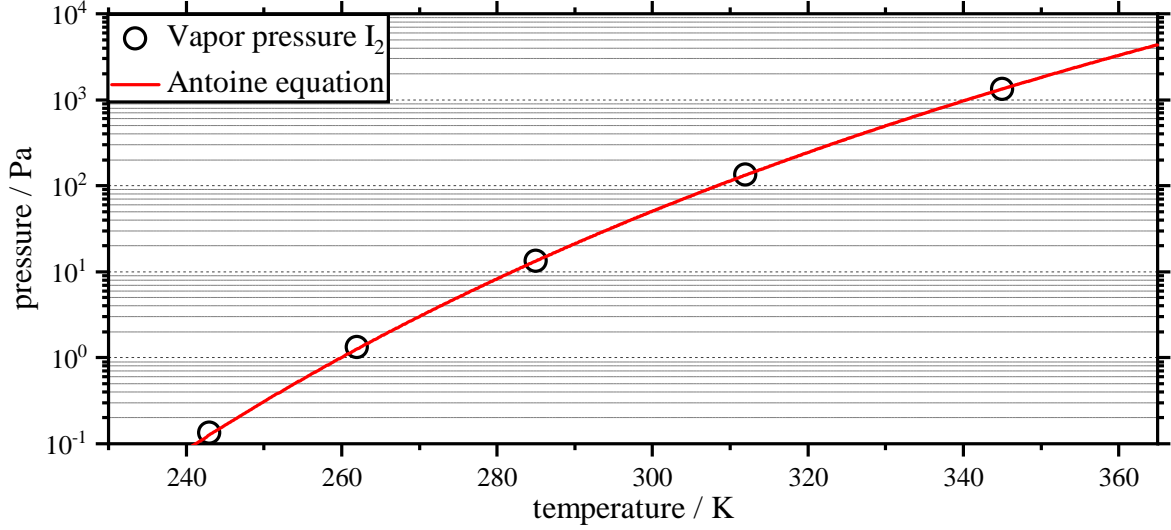
Figure 2.2: Vapor pressure of iodine I_2 as a function of temperature [36] approximated by the Antoine equation (2.4).

2.2 Absorption Spectroscopy

In this section of the paper, we first introduce saturation spectroscopy in general. Special attention is then paid to the broadening effects occurring with iodine. Afterwards the transmission spectrum of iodine is explicitly discussed. The basics and parameters for the simulations used in this work are presented. Finally, frequency modulations (FM)-spectroscopy is shortly introduced.

2.2.1 Saturation Spectroscopy

When an electromagnetic wave interacts with a medium, the frequency of the wave is still the same, but the velocity is slowed down. This results in a different complex wave number $\mathbf{k}_{\mathrm{med}} = k_0 \mathbf{n}$ with k_0 as the wave number in vacuum . The complex refractive index $\mathbf{n} = n_1 + in_2$ depends on the properties of the medium and its density. A plane wave is described by the electric field [39]:

$$E(t,x) = E_0 \, e^{-i(\omega t - \mathbf{k}_{\mathrm{med}}\, x)} = E_0 \, e^{-i2\pi\left(\nu t - \frac{\nu}{c_0}\mathbf{n}x\right)}, \tag{2.5}$$

with E_0 the amplitude of the field, t the time, x the path length and $\omega = 2\pi\nu$. Using the complex refractive index $\mathbf{n}$ gives:

$$E(t,x) = E_0 \, e^{-i2\pi\nu t} \, e^{i2\pi\frac{\nu}{c_0}xn_1} \, e^{-2\pi\frac{\nu}{c_0}xn_2} \tag{2.6}$$

The absorption of the medium is described by the imaginary part $n_2(\nu)$ of the complex refractive index and the dispersion by the real part $n_1(\nu)$. Behind the medium, the transmitted electric field amplitude is given by the transmittance factor:

$$\hat{T} = \frac{E(t, x = L_{\text{med}})}{E(t, x = 0)} \tag{2.7}$$

If instead of the electric field the intensity of a light field is considered ($I \propto |E|^2$), Lambert Beer's law describes the absorption of light passing through a medium with a length of L_{med}.

$$I = I_0 \, e^{-\alpha(\nu) L_{\text{med}}} \tag{2.8}$$

I_0 is the intensity of the incoming electric field and I the transmitted intensity. Comparing the square of the amount of (2.6) with (2.8) results in the definition of the absorption coefficient:
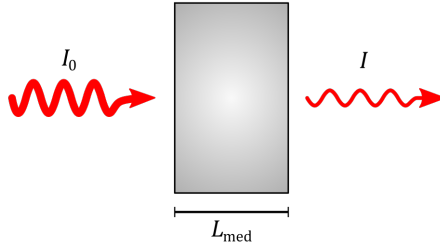
Figure 2.3: Sketch to illustrate the Lambert-Beer law for absorption and transmission of an electromagnetic field through a medium. Here I_0 describes the radiated power, I the transmitted power of the field and L_{med} the length of the medium.

$$\alpha(\nu) = 4\pi n_2 \frac{\nu}{c_0} \tag{2.9}$$

In a classical model of an atomic absorber, a charge q in a damped harmonic oscillator (mass m, eigenfrequency ω_0, damping Γ, particle density N) assumed to be driven by an electric field, which generates a dipole moment P:

$$P = Nqx, \tag{2.10}$$

$$x(\omega) = \frac{qE_0 e^{i\omega t}}{m(\omega_0^2 - \omega^2 + i\Gamma\omega)}. \tag{2.11}$$

The macroscopic polarization is linked to the electric field strength as:

$$P = \epsilon_0(\epsilon - 1)E. \tag{2.12}$$

The relative dielectric constant ϵ and and the relative magnetic permeability μ are connected to the refractive index:

$$\mathbf{n} = \sqrt{\epsilon\mu} \tag{2.13}$$

Since this work does not deal with ferromagnetic materials, the permeability is set to $\mu = 1$. In addition, a thin gaseous medium is assumed in which the refractive index does not deviate significantly from $\mathbf{n} = 1$. For this reason $n^2 - 1 = (n+1)(n-1) \simeq 2(n-1)$ is used and with the upper relations the complex refractive index is [39]:

$$\mathbf{n} = 1 + \frac{Nq^2}{2\epsilon_0 m(\omega_0^2 - \omega^2 + i\Gamma\omega)} \tag{2.14}$$

Because $|\omega - \omega_0| \ll \omega_0$ applies near the resonant frequency, the simplification $\omega_0^2 - \omega^2 \approx 2\omega_0(\omega_0 - \omega)$ is used.

$$\mathbf{n} = 1 + \frac{Nq^2}{4\epsilon_0 m\omega_0} \frac{(\omega_0 - \omega) - i\left(\frac{\Gamma}{2}\right)}{(\omega_0 - \omega)^2 + \left(\frac{\Gamma}{2}\right)^2} \tag{2.15}$$

By comparing coefficients and separating the real and imaginary parts of the complex refractive index, the result is:

$$n_1 - 1 = \frac{Nq^2}{16\pi^2\epsilon_0 m\nu_0} \frac{\nu_0 - \nu}{(\nu_0 - \nu)^2 + \left(\frac{\gamma}{2}\right)^2} \tag{2.16}$$

$$\alpha(\nu) = \frac{-Nq^2}{4\pi\epsilon_0 mc_0} \frac{\left(\frac{\gamma}{2}\right)}{(\nu_0 - \nu)^2 + \left(\frac{\gamma}{2}\right)^2} \tag{2.17}$$

These equations are the dispersion relation. They connect the absorption α and dispersion $n_1 - 1$ with each other via the complex refractive index [39]:

$$n_1 - 1 = -\frac{c_0(\nu_0 - \nu)}{2\pi\gamma\nu_0}\alpha(\nu) \tag{2.18}$$

The absorption profile (2.17) has the shape of a Lorentzian with the line width γ (FWHM) in analogy to the natural line width γ_n of atoms or molecules, that are related to the Einstein coefficient of the rate of spontaneous emission A_k or the lifetime τ_k of the excited energy level.

$$\gamma_\mathrm{n} = \frac{A_k}{2\pi} = \frac{1}{2\pi\tau_k} \tag{2.19}$$

Taking into account the dispersion relations ((2.16) and (2.17)) and equation (2.7), the complex transmission of an electric wave through a medium is obtained:

$$\hat{T}^A(\nu, L_{\text{med}}) = e^{ik_0 \mathbf{n} L_{\text{med}}} = e^{i2\pi \frac{\nu}{c_0} L_{\text{med}}} e^{i2\pi \frac{\nu}{c_0} L_{\text{med}}(n_1 - 1)} e^{-\frac{1}{2}\alpha(\nu) L_{\text{med}}} \tag{2.20}$$

Up to this point, only absorbers at rest were assumed. In this work, however, the spectroscopy of iodine takes place in gas phase. Due to the motion of the molecules, and the Doppler effect, the center frequencies of the transitions are shifted and the spectroscopic lines are Doppler broadened. In thermal equilibrium the velocity distribution of the molecules is Maxwell-Boltzmann distributed. For the Doppler broadened absorption profile, it results in a Gaussian profile:

$$\alpha_G(\nu) = \alpha^0(\nu_0) \exp\left[-\frac{4(\nu - \nu_0)^2 \ln 2}{\gamma_D{}^2}\right]. \tag{2.21}$$

The FWHM width of the Doppler broadened line profile is described with γ_D:

$$\gamma_D = \frac{\nu_0}{c}\sqrt{\frac{8k_B T \ln 2}{m}}. \tag{2.22}$$

The corresponding dispersion function D_G can be described with the help of the imaginary error function $\text{erfi}(x)$ [40].

$$D_G = n_1 - 1 = -\alpha^0(\nu_0) \exp\left[-\frac{4(\nu - \nu_0)^2 \ln 2}{\gamma_D{}^2}\right] \text{erfi}\left[\frac{\sqrt{4 \ln 2}(\nu - \nu_0)}{\gamma_D}\right] \tag{2.23}$$

In saturation spectroscopy, high optical intensities are generated to make single lines of atomic transitions visible despite Doppler broadening [41]. Due to the high optical intensity, the pump rate of an absorbing transition becomes much greater than the relaxation rate. As a result of the saturation of the transition, the absorption α becomes smaller and the medium becomes more transparent. The saturated absorption $\alpha_S(\nu)$ coefficient is then:

$$\alpha_S = \frac{\alpha_0}{1 + S} \tag{2.24}$$

Where S is the saturation parameter and α_0 is the non-saturated absorption coefficient. The saturation parameter is defined as ratio of the pumping rate P and the average relaxation rate $\bar{R}$:

$$S = \frac{P}{\bar{R}} \tag{2.25}$$

For a homogeneous absorption profile like a Lorentzian, the following saturated absorption profile will be obtained:

$$\alpha_{S,L}(\nu) = \alpha_L(\nu_0) \frac{\left(\frac{\gamma_S}{2}\right)^2}{(\nu - \nu_0)^2 + \left(\frac{\gamma_S}{2}\right)^2} \tag{2.26}$$

Owing to saturation, the line width at the FWHM increases.

$$\gamma_{\mathrm{S}} = \gamma_L \sqrt{1 + S_0} \tag{2.27}$$

For an inhomogeneously Doppler broadened transition the saturation parameter S no longer depends on the frequency ($S(\nu_0) = S_0$), and because of the increased width, the absorption is:

$$\alpha_{\mathrm{S,G}}(\nu) = \frac{\alpha_G}{\sqrt{1 + S_0}}. \tag{2.28}$$

The saturation causes hole burning in the velocity distribution, but this effect is not visible in the absorption profile. With an additional beam or a colinearly back reflected single laser beam (i.e. a standing wave) the hole can be made visible in the absorption spectra. For a standing wave the saturated absorption profile is [41]:

$$\alpha_{\mathrm{S,G}}(\nu) = \alpha_G(\nu) \frac{\gamma/2}{B \left[1 - \left(\frac{2(\nu - \nu_0)}{A+B} \right)^2 \right]^{1/2}} \tag{2.29}$$

$$A = \sqrt{(\nu - \nu_0)^2 + \left(\frac{\gamma}{2} \right)^2} \qquad \text{and} \qquad B = \sqrt{(\nu - \nu_0)^2 + (1 + 2S_0) \cdot \left(\frac{\gamma}{2} \right)^2} \tag{2.30}$$

Equation (2.29) is a Doppler broadened profile with a dip (Lamb-dip) at the center frequency ν_0 of the transition. The Lamb-dip is explained by the fact that at the resonant frequency $\nu = \nu_0$ the forward and backward running beams interacts with molecules of the same velocity component. Whereas at a frequency other than resonance $\nu \neq \nu_0$, due to the Doppler effect, both beams interact with molecules with velocity components of opposite sign. Especially at the resonance frequency, the intensity and saturation is twice as high, leading to less absorption.

Figure 2.4 shows the Doppler broadened saturated absorption profile of a transition with a Lamb-dip at the resonance frequency.
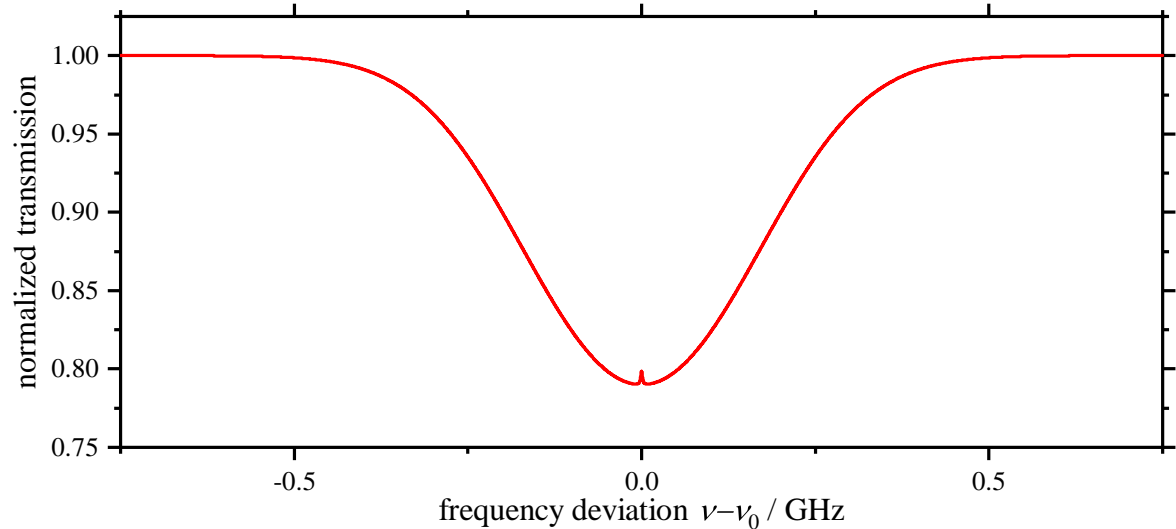
Figure 2.4: Simulated Doppler broadened transmission spectrum with Lamb-dip of a single transition line.

2.2.2 Broadening Effects

In this section, the relevant spectroscopic broadening effects for the experiments in this work with iodine are presented and discussed.

Natural linewidth (homogeneous):

The spontaneous decay of excited electronic states with a radiative lifetime τ within the molecule results in a Lorentian line profile due to the uncertainty principle (compare 2.2.1), lines corresponding to the natural line width $\gamma_n = \frac{1}{2\pi\tau}$. The excited states of the iodine $^{127}I_2$ lines that were investigated in this thesis have lifetimes in a range of 300-400 ns [42], which in turn corresponds to a FWHM width of 400-500 kHz (see equation (2.19)).

Collision broadening (homogeneous):

In the case of collision or pressure broadening, the lifetime of the excited energy levels is shortened due to state- and phase changing collisions between the particles. This results in a addition broadening to the natural linewidth. The total pressure-dependent linewidth can be described by the sum of collision broadening γ_{col} at the pressure p of the particle gas and the natural linewidth γ_n:

$$\gamma = \gamma_n + \gamma_{col} = \frac{1}{2\pi}\left(\frac{1}{\tau} + Kp\right). \tag{2.31}$$

Here $K \propto 1/\sqrt{T}$ is the pressure coefficient depending on the temperature. In [43] the pressure coefficient at a temperature of 300 K of line R(127)11-5 is given as $K(300\,\text{K}) = 2\pi \cdot 0.131 \frac{1}{\text{s}\cdot\text{Pa}}$. To specify the collision broadening at a different temperature T, the pressure coefficient can be scalled with the collision rate as:

$$K(T) = 2\pi \cdot 0.131 \frac{1}{\text{s} \cdot \text{Pa}} \cdot \sqrt{\frac{300\,\text{K}}{T}}. \tag{2.32}$$

In order to estimate the magnitude of the collision broadening γ_{col} for lines in the wavelength range around 633 nm, this pressure coefficient $K(T)$ is assumed for all investigated lines. A cold finger temperature of 15 °C for the NICE-OHMS experiment (see chapter 5.1.1) gives a vapor pressure of $p = 17.9\,\text{Pa}$ within the cell according to equation (2.4). With a wall temperature of 20 °C, that determines the gas temperature, collision broadening of $\gamma_{\text{col}} = 2.4\,\text{MHz}$ (FWHM) is obtained. In comparison, the cell is heated to 60 °C in the Toptica Beta Demonstrator studies ($p = 616\,\text{Pa}$ see chapter 4.1.1). This leads to a collision broadening of $\gamma_{\text{col}} = 76.7\,\text{MHz}$.

Power broadening and saturation intensity:

The saturation of the absorption at higher light intensities I leads to power broadening. As described in chapter 2.2.1 and equation (2.27), the pressure broadened linewidth is multiplied by $\sqrt{1+S}$ with the saturation parameter $S = \frac{I}{I_S}$ defined by the saturation intensity I_S and the intensity I. It follows the total homogeneous linewidth [44]:

$$\gamma = (\gamma_{\text{n}} + \gamma_{\text{col}}) \cdot \sqrt{1+S} = \frac{1}{2\pi}\left(\frac{1}{\tau} + Kp\right) \cdot \sqrt{1 + \frac{I}{I_S}}. \tag{2.33}$$

The saturation intensity I_S can be determined by the collision broadening and the dipole moment d of the transition as [43]:

$$I_S = \frac{\epsilon_0 c \hbar^2}{8 d^2}\left(\frac{1}{\tau} + Kp\right)^2. \tag{2.34}$$

Here ϵ_0 is the vacuum permitivity, c the speed of light and $\hbar$ the reduced Planck constant. For the NICE-OHMS experiment, a dipole moment of $d = 4 \cdot 10^{-31}\,\text{Cm}$ (for transition R(127)11-5 as given in [43]) gives a saturation intensity of $I_S = 0.77\,\text{W/cm}^2$. This would imply a broadening factor of $\sqrt{1+S} = 2.05$ for a typical measured intensity of $I = \frac{P}{2\pi\omega_0^2} = 17.5\,\text{W/cm}^2$ with ω_0 as beam radius within the cavity at NICE-OHMS. The resulting width of about $\gamma = 64\,\text{MHz}$ is an order of magnitude larger than the observed widths of a few MHz. For this reason, it is assumed that the specified dipole moment d is too large and the resulting saturation intensity I_S is too small. Typical

saturation intensities around 6 W/cm^2 are given in the literature [45, 46], which in turn correspond to a dipole moment around $d = 1.5 \cdot 10^{-31}$ Cm. In the experiment with the Toptica Beta Demonstrator, power broadening does not play a role due to the low laser power and the high pressure.

Doppler-broadening (inhomogeneous):
For low pressure gases in the visible spectrum, broadening due to the Doppler effect is the dominant effect (see equation (2.22)). It is $\gamma_{\mathrm{D}} = 365$ MHz at a wavelength of 633 nm and at room temperature of 20 °C. At a temperature of 60 °C (see chapter 4, Toptica Demonstrator) the Doppler width results in $\gamma_{\mathrm{D}} = 388$ MHz.

Time of flight broadening (homogeneous):
Due to the motion of the particles in the gas, they interact with the light only for the transit time through the width of the laser beam. Assuming a Gaussian beam with a beam diameter $(1/e^2)$ of d, the corresponding Fourier width leads to transit time broadening γ_{tr} [39]:

$$\gamma_{\mathrm{tr}} = \frac{2\bar{v}}{\pi d}\sqrt{2\ln 2}. \tag{2.35}$$

Here $\bar{v}$ is the root mean square velocity of the particles:

$$\bar{v} \approx \sqrt{\langle v^2\rangle} = \sqrt{\frac{3k_{\mathrm{B}}T}{m}}. \tag{2.36}$$

In the NICE-OHMS setup, a beam waist radius $(1/e^2)$ of $w_0 = 236\,\mu$m inside the cavity (see chapter 5.1.1) and a temperature of 20 °C results in a time of flight broadening of $\gamma_{\mathrm{tr}} = 280$ kHz. Here it is assumed that the beam waist inside the cavity changes only minimally and can be assumed as constant for this calculation. For the Toptica Beta Demonstrator (see chapter 4.1.1), a beam diameter of approx. 2 mm at a temperature of 60 °C results in a time of flight broadening of $\gamma_{\mathrm{tr}} = 27$ kHz. For both the NICE-OHMS setup and the Toptica Beta demonstrator, the time of flight broadening can be neglected compared to the collision broadened linewidth.

2.2.3 Transmission Spectra of Iodine $^{127}\mathrm{I}_2$

Due to the collision broadening introduced in chapter 2.2.2, at high pressures and/or temperatures of the gas, the broadening of the natural linewidth compared to the Doppler width can no longer be neglected. The absorption profile can then be described

by a convolution of Lorentz and Doppler profile. Such a profile is described with a Voigt profile [47]:

$$\alpha_{\mathrm{V}}(\nu) = V_0 \int_{-\infty}^{\infty} \frac{y\,e^{-t^2}}{y^2 + (x-t)^2}\,\mathrm{d}t, \tag{2.37}$$

with

$$x = \frac{\nu - \nu_0}{\sigma\sqrt{2}} \qquad \text{and} \qquad y = \frac{\gamma_{\mathrm{L}}}{2\sigma\sqrt{2}}. \tag{2.38}$$

Here is

$$V_0 = \frac{\alpha^0(\nu_0)}{\sigma\sqrt{2\pi}} \tag{2.39}$$

with the absorption $\alpha^0(\nu_0)$ at resonance frequency of a HFS component and the root-mean square (rms) width of the Gaussian

$$\sigma = \frac{\gamma_{\mathrm{D}}}{2\sqrt{2\ln(2)}}. \tag{2.40}$$

In the investigations with the TBD, the iodine is heated ($T = 60\,^\circ\mathrm{C}$, $\gamma_{\mathrm{D}} = 388\,\mathrm{MHz}$, $\gamma_{\mathrm{col}} = 76.7\,\mathrm{MHz}$), so that a Voigt profile is used for the described transmission spectra in chapter 4. Also, because of the high pressure in the cell due to the high temperature and the low power within the cell, saturation effects are negligible. Since the Voigt profile can not be expressed by analytic function, it is numerically calculated as the real part of the Faddeeva function $w(z)$ with $z = x + iy$ [48]:

$$\alpha_{\mathrm{V}}(\nu) = V_0 \cdot \mathrm{Re}\left[w\left(\frac{(\nu - \nu_0) + i\frac{\gamma_{\mathrm{L}}}{2}}{\sigma\sqrt{2}}\right)\right] \tag{2.41}$$

When using the NICE-OHMS method in Chapter 5, the iodine gas is at room temperature ($T = 20\,^\circ\mathrm{C}$, $\gamma_{\mathrm{D}} = 365\,\mathrm{MHz}$, $\gamma_{\mathrm{col}} = 2.4\,\mathrm{MHz}$). Thus, the collision broadening is so small compared to the Doppler width that only the Doppler profile is used in the description of the spectra.

For the simulation of the transmission spectra T_{Tr} in this work, the absolute square of the complex transmission factors $\hat{T}^A(\nu, L)$ of the fields from equation (2.20) is formed:

$$T_{\mathrm{Tr}} = \left|\hat{T}^A(\nu, L)\right|^2. \tag{2.42}$$

In the case of Doppler broadened spectroscopy (see TBD chapter 4), the absorption coefficient $\alpha(\nu)$ is obtained from equation (2.41) using the Voigt function. For saturation spectroscopy in the NICE-OHMS method, the absorption function α_{NO} is described by a saturated Doppler broadened profile with subtracted saturated Lorentz profile:

$$\alpha_{\mathrm{NO}}(\nu) = \alpha_{\mathrm{G,S}}(\nu) - \alpha_{\mathrm{L,S}}(\nu) \tag{2.43}$$

The saturated Doppler absorption profile is obtained from equation (2.28):

$$\alpha_{\mathrm{G,S}}(\nu) = \frac{\alpha^0(\nu_0)}{\sqrt{1+S}} \cdot \exp\left[\frac{-4(\nu-\nu_0)^2}{\gamma_{\mathrm{D}}{}^2}\right] \tag{2.44}$$

and the lamb dip is approximated by

$$\alpha_{\mathrm{L,S}}(\nu) = \left(\frac{1}{\sqrt{1+S}} - \frac{1}{\sqrt{1+2S}}\right) \cdot \alpha^0(\nu_0) \cdot \frac{(\gamma_S/2)^2}{(\nu-\nu_0)^2 + (\gamma_S/2)^2}. \tag{2.45}$$

This differs only minimally from a full theoretical description of equation (2.29) the theory in equation (2.29). For the simulation $\alpha^0(\nu_0)$ is calculated using the absorption values $\alpha_{\mathrm{IS}}(\nu_0)$ of the individual HFS components determined from the program "Iodine Spectrum". The intensity values are multiplied by a scaling factor α^0_{sca} and this factor is chosen in such a way that the intensities are adapted to the experimentally obtained absorption coefficients:

$$\alpha^0(\nu_0) = \alpha^0_{\mathrm{sca}} \cdot \alpha_{\mathrm{IS}}(\nu_0) \tag{2.46}$$

Analogous to the absorption the dispersion $n_1 - 1$ is obtained by subtracting the contribution from the Lamb-dip and from the Doppler background, thus fulfilling the Kramers-Kronig relation:

$$D_{\mathrm{all}}(\nu) = D_{\mathrm{G,S}}(\nu) - D_{\mathrm{L,S}}(\nu) \tag{2.47}$$

The saturated dispersion of the Gaussian part is calculated by using equation (2.9) and (2.23):

$$D_{\mathrm{G,S}}(\nu) = -\alpha_{\mathrm{G,S}}(\nu)\frac{c_0}{2\pi\nu_0} \operatorname{erfi}\left[\frac{\sqrt{4\ln 2}\,(\nu-\nu_0)}{\gamma_{\mathrm{D}}}\right] \tag{2.48}$$

The dispersion for the Lamb-dips based on the Lorentz function is obtained using equation (2.18) and is:

$$D_{\mathrm{L,S}}(\nu) = \frac{c_0(\nu_0-\nu)}{2\pi\gamma_{\mathrm{S}}\nu_0}\alpha_{\mathrm{L,S}}(\nu) \tag{2.49}$$

Up to this point it was assumed that the transmission respectively the absorption spectrum consist only of a single transition. However, due to the hyperfine splitting in iodine, many spectral lines of a transition are located in a narrow range of several 100 MHz. Since the Doppler width of each line is also in the order of a few 100 MHz, the individual HFS components of a transition overlap to a whole spectrum. To simulate the entire spectrum, the individual absorption coefficients and dispersion $n_1 - 1$ of each HFS component are summed:

$$\alpha^{\mathrm{all}}_{\mathrm{NO}}(\nu) = \sum_i \alpha_{\mathrm{NO},i}(\nu) \qquad \text{and} \qquad D^{\mathrm{all}}_{\mathrm{NO}}(\nu) = \sum_i D_{\mathrm{NO},i}(\nu), \tag{2.50}$$

and used to calculate the transmission with equation (2.42). A simple saturation spectroscopy setup is used to compare the simulated transmission with the experiment. Light is sent through a 50 cm long $^{127}I_2$ iodine cell (wall temperature at 20 °C, coldfinger temperature at 15 °C) and reflected back into itself with a mirror. With the help of two lenses in front and behind the cell the beam is focused inside the cell. On the first path through the cell, the iodine is saturated and interrogated with the reflected part. Using a combination of a polarizing beam splitter (in an isolator) in front of the cell and a quarter wave-plate in front of the reflecting mirror, the returned light is filtered out and observed with a photodetector.

Figure 2.5 shows the measured saturation spectrum of line P(33)6-3. Since the output power of the laser changes approximately linearly during the tuning of the optical frequency, the measured transmitted power is corrected with a linear fit at the edges beside the absorption line at higher frequency and then normalized to this baseline. Since the intensity of the laser does not behave linearly over the entire measurement range, normalization of the data with this baseline results in transmission values slightly greater than 1 (plot on left). The transmission spectrum shows a Doppler broadened background with a saturated absorption factor at the point of maximal absorption of $\alpha_{\mathrm{P}(33)6-3} = 0.14 \frac{1}{\mathrm{m}}$ respectively $\alpha_{\mathrm{P}(33)6-3} = 0.0.0082 \frac{1}{\mathrm{m \cdot PA}}$, on which the Lamb-dips of the individual HFS components can be clearly seen. In comparison the simulated transmission spectrum is shown, which is determined using the data from the literature in section 2.2.2, the parameters used in the experiment. To determine the absorption α_{sca}^0 and the saturation factor S the spectrum is fitted to the measurement.

- $P_0 = 8.25\,\mathrm{mW}$ power of light before the cell

- $w = 0.269\,\mathrm{mm}$ average beam radius along the cell

- $I = 3.6 \frac{\mathrm{W}}{\mathrm{cm^2}}$ average intensity of light in the cell

- $S = 0.352$ saturation factor

- $\alpha_{sca}^0 = 797$ scaling absorption factor

- $\alpha_{\mathrm{IS}} = 0.18 \cdot 10^{-4}$ - $0.25 \cdot 10^{-4}$ from "Iodine Spectrum" calculated line intensity of the HFS components of line P(33)6-3

- $T = 293\,\mathrm{K}$ cell wall temperature

- $p = 17.9\,\mathrm{Pa}$ pressure in the cell ($T_{\mathrm{cf}} = 15\,°\mathrm{C}$ coolfinger temperature)

- $\gamma_{\mathrm{n}} = 513.4\,\mathrm{kHz}$ natural line width [42]

- $\gamma_{\mathrm{dip}} = 4.65\,\mathrm{MHz}$ linewidth of the lamb-dips in the experiment
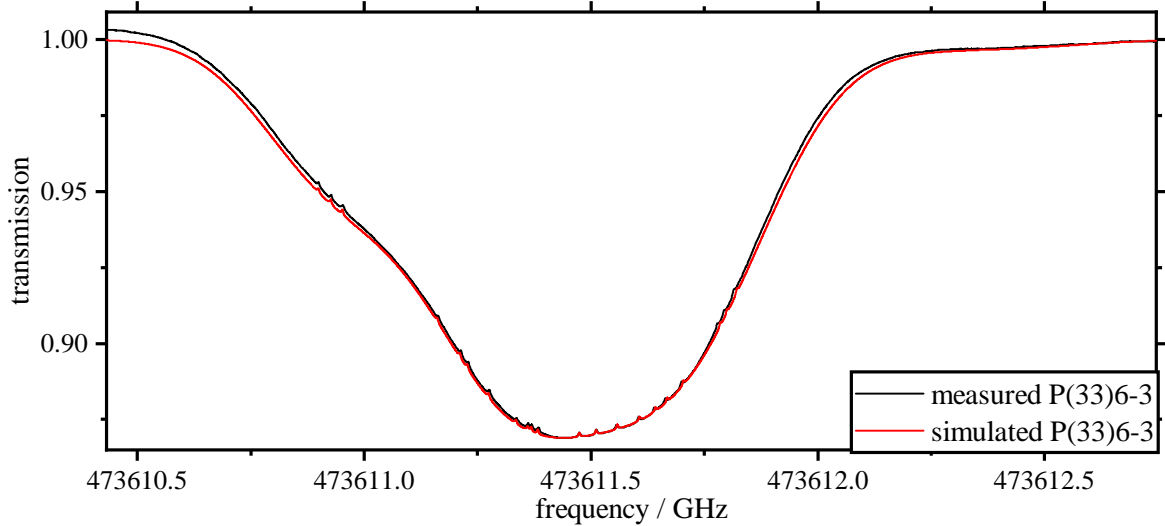

Figure 2.5: Comparison between the normalized measured (black) and simulated saturated transmission spectrum (red) of the iodine line P(33)6-3, where the HFS can be seen in the form of the Lamb-dips.

It can be seen that the simulated transmission spectrum agrees very well with the experimental spectrum. The width of the Doppler broadened spectra does not match exactly. Also the position of the Lamb-dips in the flanks has a slight offset. This can be explained by the determination of the frequency axis of the experimental curve. It can be assumed that the laser does not continuously tune the frequency linearly over the entire spectrum and that this causes errors in the determination of the frequency axes. To see how well the saturation parameter and Lamb-dips match between experiment and simulation. An additional beam was sent through the iodine cell to probe the Doppler broadened spectrum. This Doppler broadened spectrum is subtracted from the saturation spectrum, leaving only the transmission of the Lamb-dips. Figure 2.6 shows the transmission of the Lamb-dips of the HFS components "g"-"j" of the lines P(33)6-3 from the experiment and the simulation. A small vertical offset was added to the simulated spectrum to better compare it with the experimental one.

In addition, a deviation of the frequency of the different lines between simulation and experiment can be seen in the minimum of the Doppler broadened spectrum as well as in the flanks, due to the non linearity of the laser frequency scan.
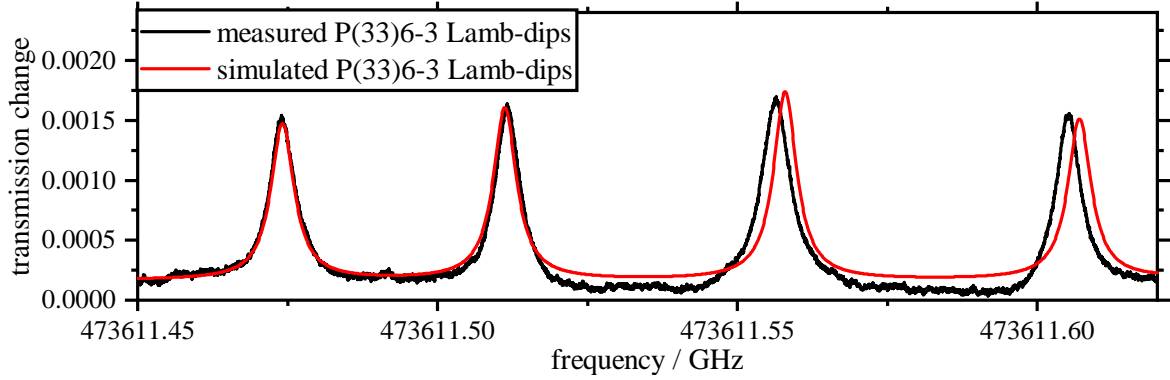
Figure 2.6: Transmission spectrum of some Lamb-dips in the center of the iodine line P(33)6-3 (line "g"-"j") where the Doppler broadened background was subtracted. Comparison between measured data (black) and simulated data (red).

The resulting saturation intensity is calculated from the saturation parameter using the parameters of the setup. Also, based on the measured width of the Lamb-dips, using the theoretical natural line width, the collision broadening is determined and the K-factor is calculated. These quantities are then used for the simulations of the NICE-OHMS experiment later in the thesis. The parameters resulting from the fitting for the iodine line P(33)6-3 are the following:

- $\gamma_{\mathrm{col}} = 3.5\,\mathrm{MHz}$ collision broadening and $\sqrt{1+S} = 1.16$ power broadening factor based on $S = 0.352$ and equation (2.33)

- $K(T) = 1.2 \cdot \sqrt{\frac{293\mathrm{K}}{T}}\,\frac{\mathrm{MHz}}{\mathrm{Pa}}$ K-factor based on equation (2.33) and $p = 17.9\,\mathrm{Pa}$

- $I_{\mathrm{sat}} = 10.3\,\frac{\mathrm{W}}{\mathrm{cm}^2}$ saturation intensity ($P = 8.25\,\mathrm{mW}$ power and $w = 0.269\,\mathrm{mm}$ average Gaussian beam radius)

- $\alpha^0_{\mathrm{P}(33)6-3} = \alpha_{\mathrm{P}(33)6-3} \cdot \sqrt{1+S} = 0.0091\,\frac{1}{\mathrm{m \cdot PA}}$ unsaturated absorption coefficient based on equation (2.28)

- $d = 1.5 \cdot 10^{-31}\,\mathrm{Cm}$ dipole moment based on I_{sat}, $K(T)$ and equation (2.34)

Some of the quantities obtained from experiment and simulation differ slightly from the values of chapter 2.2.2 that were taken from other publications and theory. However, these variations are well attributed to measurement inaccuracies. This is because the nonlinear process of saturation plays a role both in the broadening effects and in the absorption itself. In the simulation here, the saturation S and the resulting saturation

intensity I_{sat} is determined only from the absorption and the dip depth. The saturation intensity I_{sat} in the experiment is then determined by the average intensity I calculated within the cell. In reality, the intensity varies strongly within the 50 cm long cell due to the geometry of the Gaussian beam both along the cell in the propagation direction and the beam profile as a cross section through the beam itself. Thus, the saturation S also differs depending on the beam area within the cell. Since not only the width but also the saturation is used for the determination of the K-factor, the deviations in this and the collision broadening can occur.

2.2.4 FM-Spectroscopy

Since NICE-OHMS is based on a combination of frequency modulated (FM)-spectroscopy and cavity enhanced absorption spectroscopy, FM-spectroscopy will be considered in more detail in this section. By modulating the emitted frequency/phase of a laser, it is possible to perform sensitive optical spectroscopy. As the technical noise of the laser is mostly at low frequencies, modulating and detecting at high frequencies in principle allows detection at the fundamental shot noise limit. The interaction of the frequency modulated light field with a medium leads to an amplitude modulation of the detected signal at the modulation frequency. Any noise that does not occur at the modulation frequency is filtered out [49]. Figure 2.7 shows a typical setup for FM-spectroscopy [50]. The light of a laser is modulated by an electro-optical phase modulator (EOM) and then passes through the medium under investigation. A photodiode detects the transmission of the field through the medium. For the evaluation of the signal, it is mixed with the modulation frequency and low-pass filtered. The phase of the detection frequency can be set so that the signal can be evaluated for either the absorption or dispersion part.

For FM-spectroscopy, the phase of the E-field of the incoming light beam is modulated sinusoidally:

$$E^{\text{FM}}(\nu_{\text{c}}, t) = E_0 \exp\left[i2\pi\nu_{\text{c}}t + i\beta\sin\left(2\pi\nu_{\text{m}}t\right)\right], \tag{2.51}$$

where β is the modulation index and ν_{m} the modulation frequency [49]. This form can be expressed by a series of j-th order Bessel functions $J_j(\beta)$ to describe the individual frequency components of spectrally modulated light [51]:

$$E^{\text{FM}}(\nu_{\text{c}}, t) = E_0\, e^{2i\pi\nu_{\text{c}}t} \sum_{j=-\infty}^{\infty} J_j(\beta)e^{i2\pi j\nu_{\text{m}}t} \tag{2.52}$$
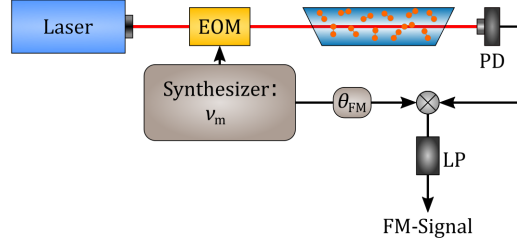
Figure 2.7: Setup sketch of frequency modulation (FM)-spectroscopy, with electro-optical phase modulator (EOM), a gas cell, photodiode (PD), low-pass filter (LP), modulation frequency ν_m and the phase shift of the frequency modulations θ_FM.

Here the zeroth order describes the original carrier frequency ν_c. For a small modulation index $\beta < 1$ only the 0-th and 1-st order of the Bessel function are important. In addition, $J_{-1}(\beta) = -J_1(\beta)$ applies, so that the E-field can be written as:

$$E^\mathrm{FM}(\nu_\mathrm{c}, t) = E_0\, e^{2i\pi\nu_\mathrm{c}t} \left[J_0(\beta) + J_1(\beta)e^{i2\pi\nu_\mathrm{m}t} - J_1(\beta)e^{-i2\pi\nu_\mathrm{m}t} \right] \qquad (2.53)$$

Under these conditions the modulated E-field consists of three frequencies components, the carrier and the two 1-st order side bands $\nu_\mathrm{c} \pm \nu_\mathrm{m}$. This three complex E-field components are shown in figure 2.8.
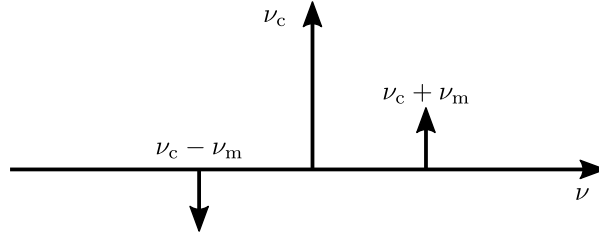

Figure 2.8: Sketch of carrier and sidebands of a complex electric field generated with an EOM.

The three frequency components of the E-Field behind an absorber are described with the complex transmission function ($\hat{T}^\mathrm{A}_{\pm 1} = \hat{T}^\mathrm{A}(\nu_\mathrm{c} \pm \nu_\mathrm{m})$ and $\hat{T}^\mathrm{A}_0 = \hat{T}^\mathrm{A}(\nu_\mathrm{c})$, see (2.20)) as follows:

$$E^\mathrm{FM}_\mathrm{A}(\nu_\mathrm{c}, t) = E_0\, e^{2i\pi\nu_\mathrm{c}t} \left[\hat{T}^\mathrm{A}_0 J_0(\beta) + \hat{T}^\mathrm{A}_1 J_1(\beta)e^{i2\pi\nu_\mathrm{m}t} - \hat{T}^\mathrm{A}_{-1} J_1(\beta)e^{-i2\pi\nu_\mathrm{m}t} \right]. \qquad (2.54)$$

The intensity of the frequency modulated light behind an absorber is given by the

square of the E-field:

$$I_A^{FM}(\nu_c, t) = \left| E_A^{FM}(\nu_c, t) \right|^2. \tag{2.55}$$

$$
\begin{aligned}
I_A^{FM}(\nu_c, t) = I_0 \Big\{ & J_0^2(\beta)\hat{T}_0^A\hat{T}_0^{A*} + J_1^2(\beta)\left(\hat{T}_1^A\hat{T}_1^{A*} + \hat{T}_{-1}^A\hat{T}_{-1}^{A*}\right) \\
& + 2J_0(\beta)J_1(\beta)\mathrm{Re}\left[\left(\hat{T}_1^A\hat{T}_0^{A*} - \hat{T}_0^A\hat{T}_{-1}^{A*}\right)e^{i2\pi\nu_m t}\right] \\
& - 2J_1^2(\beta)\mathrm{Re}\left[\hat{T}_1^A\hat{T}_{-1}^{A*}e^{i4\pi\nu_m t}\right] \Big\}
\end{aligned}
\tag{2.56}
$$

This results in three frequency contributions that determine the intensity of the light: at DC, at the modulation frequency ν_m and at twice the modulation frequency $2\nu_m$. In this thesis only the contributions at the modulation frequency ν_m are of interest:

$$I_A^{FM,\nu_m} = 2I_0J_0(\beta)J_1(\beta)\mathrm{Re}\left[\left(\hat{T}_1^A\hat{T}_0^{A*} - \hat{T}_0^A\hat{T}_{-1}^{A*}\right)e^{i2\pi\nu_m t}\right] \tag{2.57}$$

$$
\begin{aligned}
I_A^{FM,\nu_m} = & 2I_0J_0(\beta)J_1(\beta) \\
& \times \Big\{ \mathrm{Re}\left[\hat{T}_1^A\hat{T}_0^{A*} - \hat{T}_0^A\hat{T}_{-1}^{A*}\right]\cos(2\pi\nu_m t) - \mathrm{Im}\left[\hat{T}_1^A\hat{T}_0^{A*} - \hat{T}_0^A\hat{T}_{-1}^{A*}\right]\sin(2\pi\nu_m t) \Big\}
\end{aligned}
\tag{2.58}
$$

To demodulate the error signal from the transmitted light, the signal detected by a photodiode is mixed with the phase shifted reference modulation frequency ($\sin[2\pi\nu_m t + \theta_{FM}]$) and low-pass filtered. A dual balanced mixer and a low pass filter are used for this purpose (see fig. 2.7) and the FM-signal is:

$$
\begin{aligned}
S_A^{FM,\nu_m} \propto & J_0(\beta)J_1(\beta) \\
& \times \Big\{ \mathrm{Re}\left[\hat{T}_1^A\hat{T}_0^{A*} - \hat{T}_0^A\hat{T}_{-1}^{A*}\right]\cos\theta_{FM} + \mathrm{Im}\left[\hat{T}_1^A\hat{T}_0^{A*} - \hat{T}_0^A\hat{T}_{-1}^{A*}\right]\sin\theta_{FM} \Big\}.
\end{aligned}
\tag{2.59}
$$

Figure 2.9 shows the FM-signal S_A^{FM,ν_m} for one line as an example. The dispersion part ($\theta_{FM} = 0$) for two different modulation frequencies ν_m and the absorption part ($\theta_{FM} = \pi/2$) are illustrated.
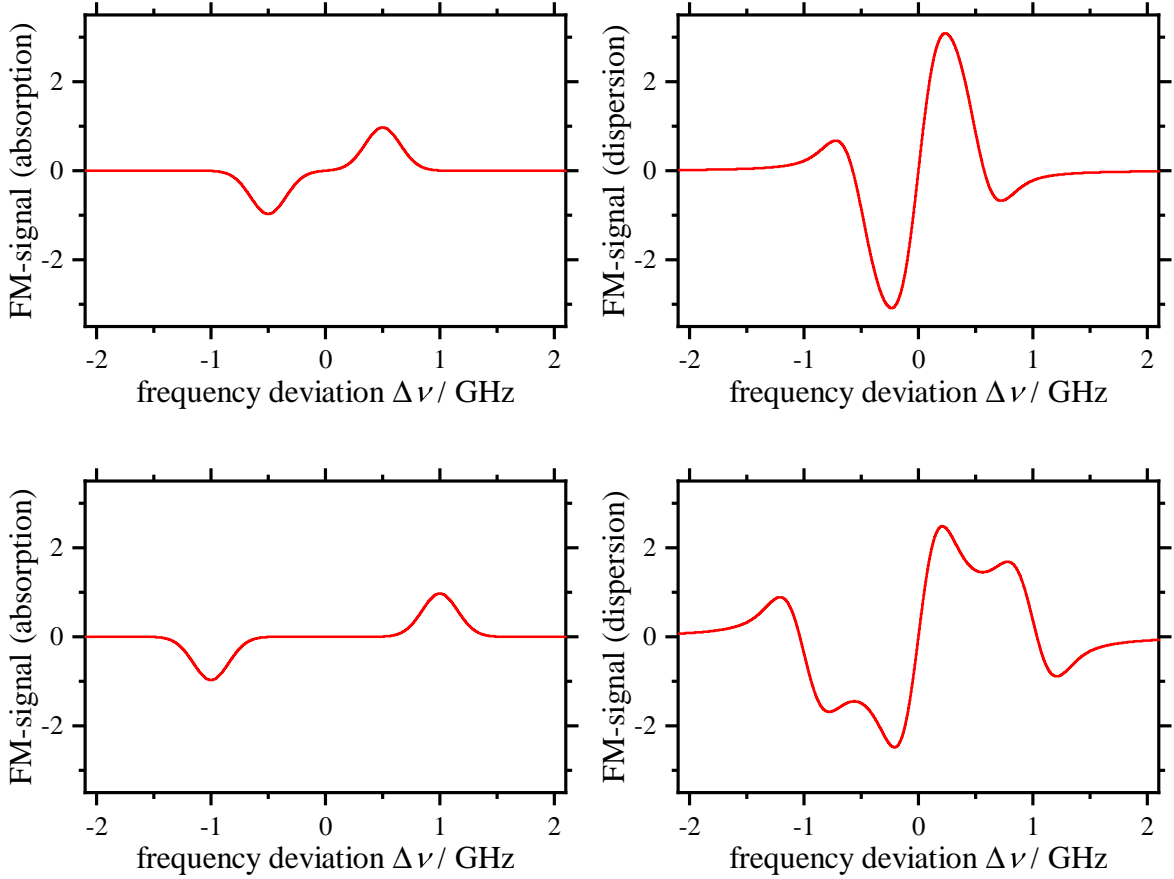
Figure 2.9: Simulated FM-signal $S_{\text{A}}^{\text{FM},\nu_{\text{m}}}$ of a single transition plotted vs the frequency deviation $\Delta\nu$. The left column shows the absorption fraction ($\theta_{\text{FM}} = \pi/2$) and the right column the dispersion fraction ($\theta_{\text{FM}} = 0$). The first line shows a modulation frequency of $\nu_{\text{m}} = 0.5\,\text{GHz}$ and the lower one of $\nu_{\text{m}} = 1\,\text{GHz}$.

2.3 Fabry-Perot Cavities

The frequency of a molecular transition can be determined with the FM-spectroscopy discussed in the previous chapter. With the help of an optical cavity, high intensities can be generated so that a transition of an absorbing medium within the cavity can easily be saturated. This chapter is dedicated to the properties of optical resonators [52].

Figure 2.10 shows a sketch of a simple structure of a Fabry-Perot cavity. An electromagnetic field is traveling between two concave mirrors M, which are positioned at a distance L_{C} from each other. The curvature of the mirrors is described by the radius r_{M}. A mirror's properties are described by the reflection coefficient r, the transmission

coefficient t and the losses l related to the electric field E. The coefficients related to the power are then:$R = r^2$,$T = t^2$ and $L = l^2$. Due to the conservation of energy, the following correlation applies to each mirror:
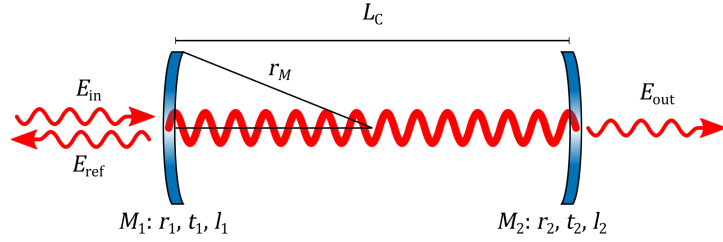
$$1 = R + T + L = r^2 + t^2 + l^2 \tag{2.60}$$

Figure 2.10: Sketch of a Fabry-Perot cavity with corresponding labeling of physical quantities with the length of the cavity L_C, incoming E_{in}, reflected E_{ref} and transmitted E_{out} E-field, radius of curved mirrors r_M, mirrors M and there probabilities: reflection r and transmission t coefficients and losses l.

One part of an incoming E-field E_{in} is reflected E_{ref} at the FPI and another part is transmitted E_{out}. If both mirrors have the same reflectivity ($r_1 = r_2$ and losses are neglected ($l = 0$), the total incoming E-field is transmitted by the FBI under resonance conditions.

2.3.1 Properties of Optical Cavities

In order for light to be transmitted at all by an FPI and for the field inside to be amplified, the fields running back and forth in the cavity must constructively interfere. If the optical path length of the cavity ($n \cdot L_{cav}$) is a multiple of half of the wavelength ($k \cdot \frac{1}{2}\lambda$) of the field, resonance occurs in the cavity. k is defining the longitudinal mode of the FPI. This results in the following resonance condition for the frequency of the E-field [53]:

$$\nu_k = \frac{kc}{2nL_{cav}} \tag{2.61}$$

Figure 2.11 shows the transmission of an FPI where the length and thus the frequency has been changed over a certain range. This is a peridoic sequence of frequency modes.
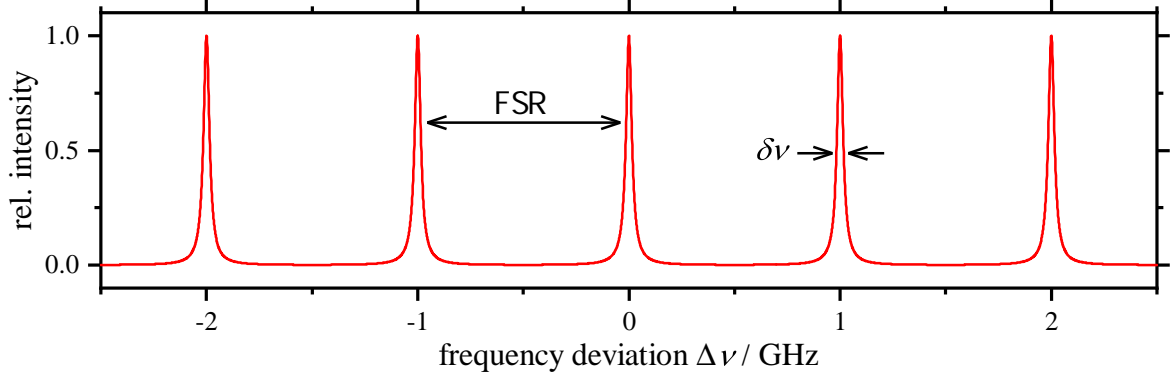
Figure 2.11: Transmission spectrum of a Fabry-Perot interferometer showing the relative transmitted intensity versus frequency deviation due to the change in length of the resonator. Thereby the visual representation of the free spectral range FSR and the full-width half-maximum of the resonance peaks $\delta\nu$ are shown.

In frequency space, the free spectral range (FSR) describes the distance between the mode k and $k+1$:

$$\text{FSR} = \nu_{k+1} - \nu_k = \frac{c}{2nL_{\text{cav}}} \tag{2.62}$$

The finess F is defined by the ratio of the mode width $\delta\nu$ and the FSR and indicates the quality of a resonator:

$$F = \frac{\text{FSR}}{\delta\nu_{\text{cav}}}. \tag{2.63}$$

As the reflectivity of the cavity mirrors improves, less light is lost inside the cavity, increasing the quality of the cavity and thus the finesse. If the reflectivity of the mirror is high ($r \approx 1$), the finesse depends on the reflectivity as follows [54]:

$$F \approx \frac{\pi\sqrt{r_1 r_2}}{1 - r_1 r_2}. \tag{2.64}$$

Using equations (2.63) and (2.64), the linewidth of the cavity is obtained for the case $\delta\nu_{\text{cav}} \ll \text{FSR}$:

$$\delta\nu_{\text{cav}} \approx \text{FSR} \cdot \frac{1 - r_1 r_2}{\pi\sqrt{r_1 r_2}}. \tag{2.65}$$

2.3.2 Transmission, Absorption, Reflection

Next the complex coefficients which describe the change of an electric field incident on a cavity after transmission and reflection. First the transmission field through the

cavity is described as follows:

$$\hat{T}_{\text{cav}}(\nu) = \frac{t_1 t_2 e^{-i\varphi(\nu)/2}}{1 - r_1 r_2 e^{-i\varphi(\nu)}}. \tag{2.66}$$

Here, the transmission of the cavity depends on both the transmission t and the reflection r of the mirrors M, and the round-trip phase φ of the field inside the cavity. The round-trip phase (neglecting phase shifts at the mirrors and the Gouy-phase from diffraction) is described as follows:

$$\varphi(\nu) = \frac{4\pi\nu n L_{\text{cav}}}{c}. \tag{2.67}$$

The resonance condition described requires that the phase must be a whole multiple of 2π:

$$\varphi(\nu_k) = 2k\pi, \tag{2.68}$$

leading to equation (2.61). Compared to the transmission, the complex reflectivity of the cavity depends additionally on losses l of the mirrors M:

$$\hat{R}_{\text{cav}}(\nu) = \frac{r_1 - r_2\sqrt{1 - l_1^2}\,e^{-i\varphi(\nu)}}{1 - r_1 r_2 e^{-i\varphi(\nu)}}. \tag{2.69}$$

Figure 2.12 shows an example of the real and imaginary part of the complex E-field transmission and reflection of a cavity as a function of the frequency shift $\Delta\nu$.

With an absorber like a gas inside the cavity describes how the transmission and reflection of the cavity changes. Due to the change of the refractive index n by the absorber, the resonant frequency is shifted as the optical path length increases and leads to an additional single pass phase shift $\phi(\Delta\nu)$. Also there is an attenuation due to the absorption $\alpha(\Delta\nu)$ within a roundtrip of the field, resulting in the transmission and reflection of a cavity with absorber:

$$\hat{T}_{\text{cav}}^{\text{A}}(\Delta\nu) = \frac{t_1 t_2 e^{-i\varphi(\nu)/2} e^{-\alpha(\Delta\nu)L_{\text{cell}}} e^{-i\phi(\Delta\nu)}}{1 - r_1 r_2 e^{-i\varphi(\nu)} e^{-2\alpha(\Delta\nu)L_{\text{cell}}} e^{-i2\phi(\Delta\nu)}} \tag{2.70}$$

and

$$\hat{R}_{\text{cav}}^{\text{A}}(\Delta\nu) = \frac{r_1 - r_2\sqrt{1 - l_1^2}\,e^{-i\varphi(\nu)} e^{-2\alpha(\Delta\nu)L_{\text{cell}}} e^{-i2\phi(\Delta\nu)}}{1 - r_1 r_2 e^{-i\varphi(\nu)} e^{-2\alpha(\Delta\nu)L_{\text{cell}}} e^{-i2\phi(\Delta\nu)}}. \tag{2.71}$$

For small absorption ($\alpha(\nu) \ll \pi/2F$), the effect of the cavity can be described by an effective path length L_{eff}, on which the light and the absorber interact [54]:

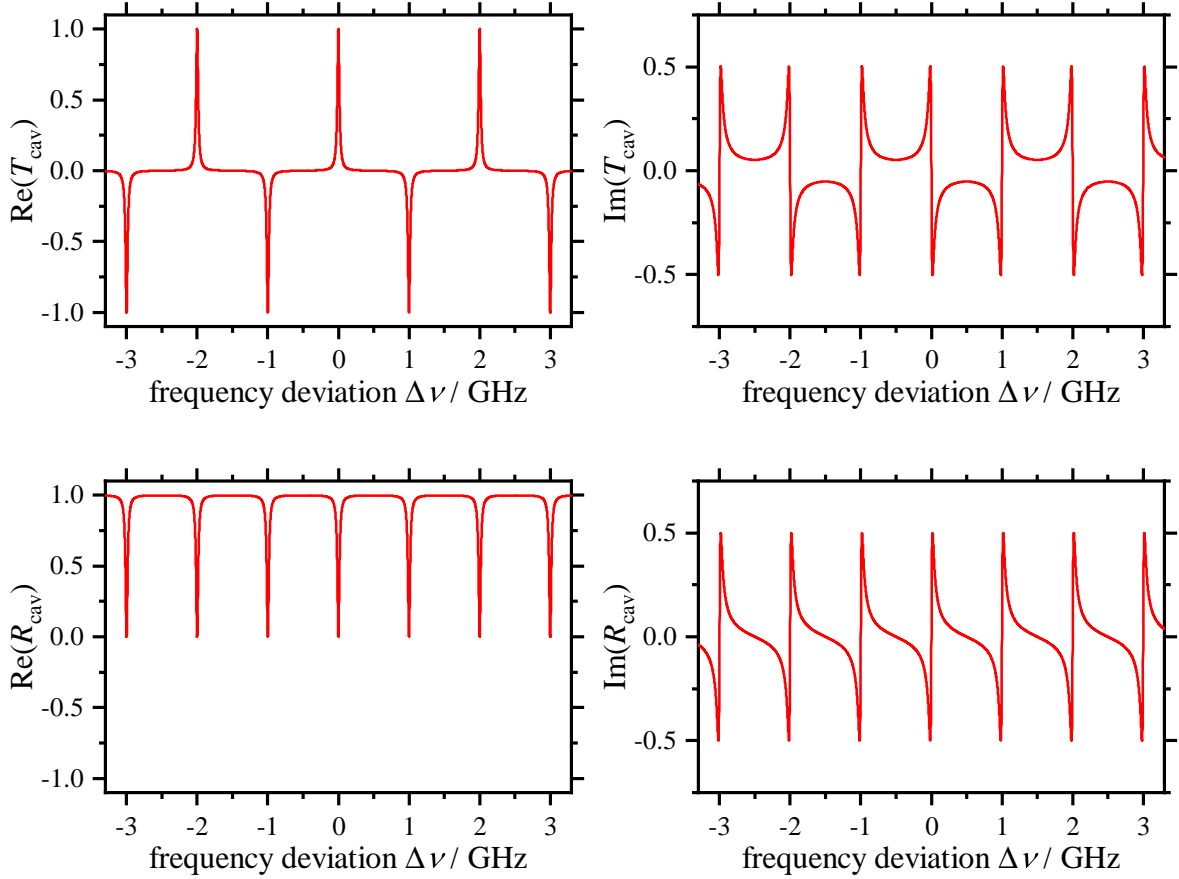$$L_{\text{eff}} = \frac{2F}{\pi} L_{\text{cell}}, \tag{2.72}$$

Figure 2.12: Simulation of the transmission coefficient $\hat{T}_{\mathrm{cav}}(\nu)$ (top) and reflection coefficient $\hat{R}_{\mathrm{cav}}(\nu)$ (bottom) of an empty cavity as a function of the frequency deviation from resonance. On the left the real part and on the right the imaginary part is shown. The following values are used for the cavity: $r_1 = 0.9$, $r_2 = 0.9$, $t_1 = 0.1$, $t_2 = 0.1$, $l_1 = l_2 = 0$, FSR = 1 GHz.

where F is the finesse of the empty cavity and L_{cell} is the length of the cell. This relationship is only valid if the absorption of the absorber does not influence the finesse too much. The finesse with absorber is then as follows [52]:

$$F = \frac{\pi \sqrt{r_1 r_2} e^{-\frac{\alpha}{2} L_{\mathrm{cell}}}}{1 - r_1 r_2 e^{-\alpha L_{\mathrm{cell}}}}. \tag{2.73}$$

2.4 Pound-Drever-Hall (PDH)

As a first step of the NICE-OHMS method, a laser frequency is locked to a Fabry-Perot cavity using the Pound-Drever-Hall (PDH) method. The PDH method generates an error signal proportional to the frequency offset of the laser to the cavity with low noise and high bandwidth. A feedback loop is used to correct frequency fluctuations caused by the laser [55]. Using the PDH method, the stability of the laser frequency can be improved significantly [56].

Figure 2.13 schematically shows the structure of a PDH stabilization. The light of a laser is phase modulated by an electro-optical phase modulator, so that two additional sidebands are generated. This light is coupled into a cavity, and the reflected light from the cavity is detected by a photodiode. The detected signal at the modulation frequency f_{PDH} is mixed with the modulation frequency f_{PDH} and low pass filtered to produce the PDH error signal.
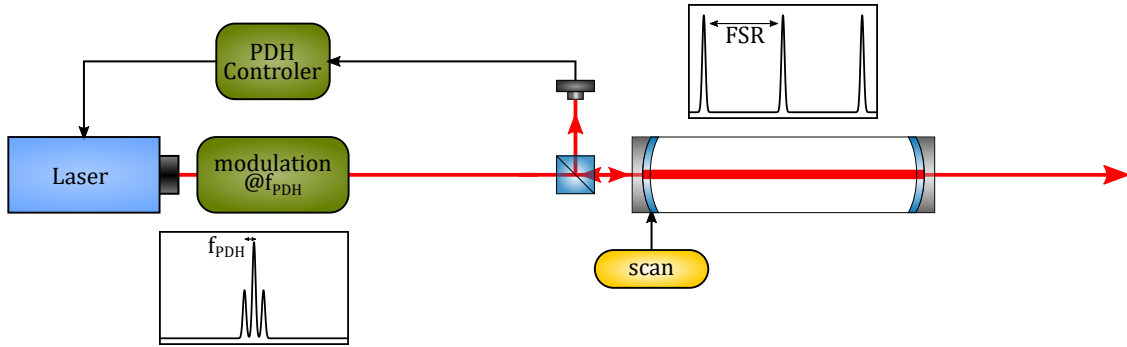

Figure 2.13: Sketch of the experimental setup for stabilizing the frequency of a laser using the PDH method on the resonance of a cavity. Also shown is the modulated laser spectrum (left) and the transmission spectrum of the cavity with free spectral range FSR (right).

What does the error signal look like that is detected by the photodiode and used for frequency stabilization? For this purpose, it is considered how the electromagnetic fields behaves after reflection from cavity. First, a reflection coefficient $F(\nu)$ is defined, which describes the ratio between the radiated E-field E_{inc} and the reflected E-field E_{ref} in front of the cavity [55] :

$$F(\nu) = \frac{E_{\text{ref}}}{E_{\text{inc}}} = \hat{R}_{\text{cav}} \tag{2.74}$$

Analogous to FM-spectroscopy (section 2.2.4), the light is modulated so that two additional frequency sidebands are generated. The emitted field can then be described by Bessel functions as described in Equation (2.53):

$$E_{\text{inc}} = E_0 e^{i\nu t} \left[J_0(\beta) + J_1(\beta) e^{if_{\text{PDH}}t} - J_1(\beta) e^{-if_{\text{PDH}}t} \right] \tag{2.75}$$

Here f_{PDH} is the PDH modulation frequency and β is the modulation index. With equation (2.74) we get the following for the cavity reflected field under consideration of the sidebands [55]:

$$\begin{aligned} E_{\text{ref}} =& E_0 \left[F(\nu) J_0(\beta) e^{i\nu t} \right. \\ &\left. + F(\nu + f_{\text{PDH}}) J_1(\beta) e^{i(\nu + f_{\text{PDH}})t} - F(\nu - f_{\text{PDH}}) J_1(\beta) e^{i(\nu - f_{\text{PDH}})t} \right] \end{aligned} \tag{2.76}$$

Since the power P_{ref} of the light field is detected, the absolute square $P_{\text{ref}} = |E_{\text{ref}}|^2$ is considered:

$$\begin{aligned} P_{\text{ref}} =& P_{\text{c}} \left|F(\nu)\right|^2 + P_{\text{s}} \left\{ |F(\nu + f_{\text{PDH}})|^2 + |F(\nu - f_{\text{PDH}})|^2 \right\} \\ &+ 2\sqrt{P_{\text{c}}P_{\text{s}}} \times \left\{ \, \text{Re}\left[F(\nu)F^*(\nu + f_{\text{PDH}}) - F^*(\nu)F(\nu - f_{\text{PDH}}) \right] \cos(f_{\text{PDH}}t) \right. \\ &\left. + \text{Im}\left[F(\nu)F^*(\nu + f_{\text{PDH}}) - F^*(\nu)F(\nu - f_{\text{PDH}}) \right] \sin(f_{\text{PDH}}t) \, \right\} \\ &+ \text{O}\left(2f_{\text{PDH}} \right) \end{aligned} \tag{2.77}$$

Here 3 different terms appear. First the direct reflection of the carrier and the sidebands. Second, mixed terms can be seen which result from the interference between the carrier and the sidebands (f_{PDH}) and further terms which result from the interference between the sidebands ($2f_{\text{PDH}}$). For the error signal the interference term between the carrier and the sidebands is of interest, which oscillates at the modulation frequency f_{PDH} and accommodates the phase information between the bands. Experimentally, this term is filtered out by mixing with the modulation frequency and a lowpass filter. If the carrier frequency ν_{c} is now in the resonance range of the cavity and the modulation frequency is so high that the sidebands are totally reflected ($F(\nu \pm f_{\text{PDH}}) \approx -1$), only the imaginary part is important (cf. equation (2.77), $\Rightarrow F^*(\nu) - F(\nu) = -2i \, \text{Im}\{F(\nu)\}$) and the following error signal ϵ is obtained:

$$\epsilon = -2\sqrt{P_{\text{c}}P_{\text{s}}} \text{Im}\left[F(\nu)F^*(\nu + f_{\text{PDH}}) - F^*(\nu)F(\nu - f_{\text{PDH}}) \right] \tag{2.78}$$

Figure 2.14 shows the simulation of such a PDH error signal ϵ. At the resonance frequency of the cavity the signal changes sign with a strong slope. With the help of this error signal, the frequency of a laser can be stabilized to the resonance of a cavity.
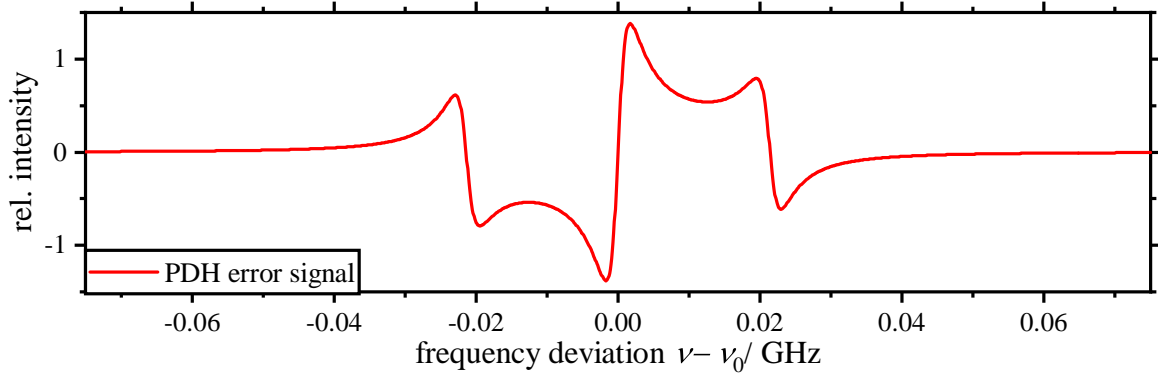
Figure 2.14: Simulated Pound-Drever-Hall error signal with the relative intensity plotted against the deviation from the resonance frequency of the cavity.

Since the interference between the bands determines the error signal, it is proportional to $J_0(\beta)J_1(\beta)$. The optimum signal is at a modulation index of $\beta = 1.08$ and corresponds to:

$$\frac{P_s}{P_c} = 0.42. \tag{2.79}$$

2.5 NICE-OHMS

Noise-immune cavity-enhanced optical heterodyne molecular spectroscopy (NICE-OHMS) is a technique to detect weak molecular transitions in the gaseous state [57]. This technique combines frequency modulation spectroscopy (FMS), power build up and increased effective absorption length by a cavity. Using FMS reduces the noise and using the cavity extends the length at which the light can interact with the molecule [58]. The trick in combining the techniques is to choose the modulation frequency according to the FSR of the cavity. Thus the triplet consisting of carrier and sidebands is transmitted through the cavity in the same way and all experience the same influences from residual frequency fluctuations between laser and cavity. This in turn reduces the amplitude noise which is called "noise immunity" [23]. Since within the cavity the beams run counter wise to each other, NICE-OHMS can be used to investigate both Doppler broadened signal (Db) and sub-Doppler signal (sD) [59]. In this chapter, we now present the basics needed to investigate the influence of the NICE-OHMS method on the contributions of frequency uncertainty using iodine as an example.
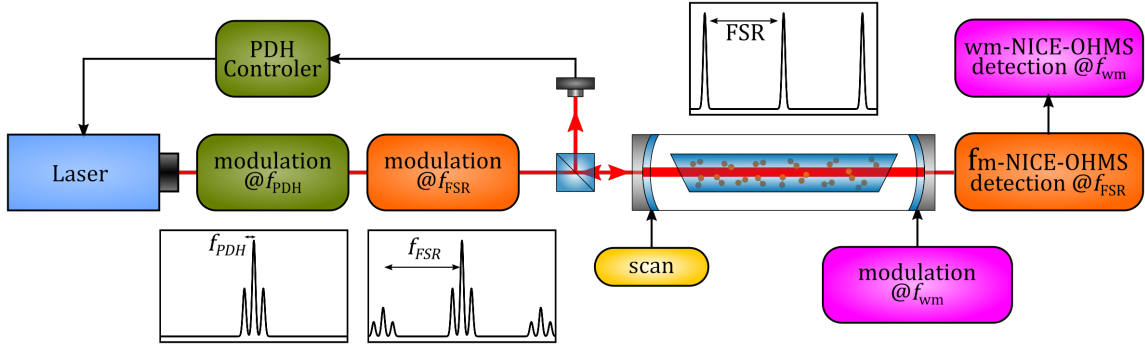
Figure 2.15: Sketch illustration of the NICE-OHMS method for stabilizing the frequency of a laser on an absorption line of a medium. The PDH stabilization (green) from figure 2.13 is extended by a further phase modulation of the light at a modulation frequency f_{FSR} of the FSR with shown spectrum and the frequency modulation (FM) detection behind the cavity (orange), the modulation of the length of the cavity with a frequency f_{wm} and the wavelength modulation (wm) detection (pink) and an absorber cell inside the cavity.

2.5.1 Principle

Figure 2.15 shows a schematic sketch of the NICE-OHMS setup used in the thesis for stabilizing the frequency of a laser to a nuclear transition [60]. As described in chapter 2.4, first the frequency of the laser is stabilized to the length of a cavity using the PDH method. For this purpose, frequency sidebands in the MHz range are generated with the modulation frequency f_{PDH} and the light reflected from the cavity is detected and evaluated with a PDH controller. Inside the cavity, the molecule to be investigated is located in gas form in a glass cell. Additionally, for the NICE-OHMS method, the light field of the laser is further modulated with another frequency f_{FSR}, so that sidebands corresponding to the FSR freqeuncy of the cavity are generated. This frequency modulation is used for FMS to study molecular transitions. Behind the cavity, the transmitted light field is observed with a detector and evaluated at the modualtion frequency of the FSR. For this purpose, the signal is mixed with the modulation frequency f_{FSR} and it is called frequency modulated NICE-OHMS detection. In order to be able to tune the frequency ν of the laser (scan), the length of the cavity is changed so that a frequency change is the result. In order to suppress the Doppler background during the recording of the NICE-OHMS signals, the length of the cavity is modulated

with the frequency f_{wm}. Using a lock-in amplifier, a Doppler-free signal is produced, which is here called wavelength modulated (wm-NICE-OHMS) signal.

The signal behind the cavity can be described with the tools presented in section 2.2.4 for FM-spectroscopy. Due to the PDH stabilization, the frequency of the carrier is in resonance with the cavity and the PDH sidebands are completely reflected by the cavity, so that they can be neglected when considering the signal behind the cavity. Since the sidebands with frequency f_{FSR} have a distance equal to the FSR of the cavity, they are completely transmitted. This results in the same initial situation behind the cavity as in FM-spectroscopy. For this reason, equation (2.59) can be used, with one change: instead of the transmission of the absorber $\hat{T}^A$, the transmission of the cavity with absorber $\hat{T}^{cav}_A$ from equation (2.70) is used. This results in the following NICE-OHMS signal behind the cavity:

$$
\begin{aligned}
S_A^{NO,\nu_m} \propto & J_0(\beta) J_1(\beta) \\
& \times \left\{ \mathrm{Re} \left[\hat{T}_1^{cav} \hat{T}_0^{cav*} - \hat{T}_0^{cav} \hat{T}_{-1}^{cav*} \right] \cos\theta_{FM} \right. \\
& \left. + \mathrm{Im} \left[\hat{T}_1^{cav} \hat{T}_0^{cav*} - \hat{T}_0^{cav} \hat{T}_{-1}^{cav*} \right] \sin\theta_{FM} \right\}
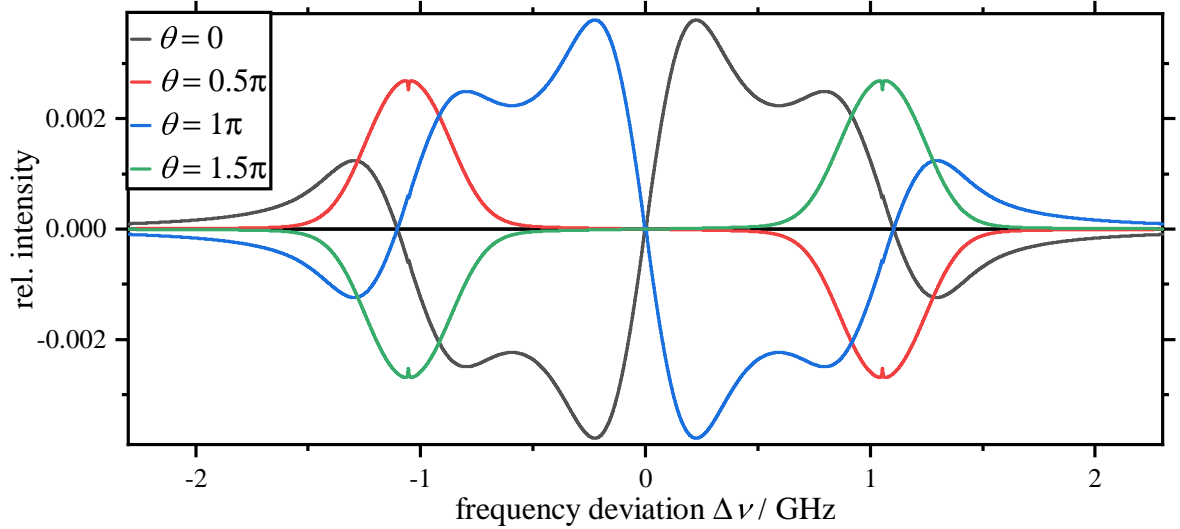\end{aligned}
\tag{2.80}
$$

Figure 2.16: Simulated NICE-OHMS signals of a single transition versus frequency deviation from resonance of absorption line with a FSR of 1.054 GHz, Doppler FWHM of around 365 MHz and for different phases θ_{FM}.

Here $\hat{T}_0^{cav} = \hat{T}_A^{cav}(\nu)$ is the transmission of the carrier and $\hat{T}_{\pm 1}^{cav} = \hat{T}_A^{cav}(\nu \pm f_{FSR})$ the transmission of the sidebands. θ_{FM} describes the phase shift between the detected signal and the reference signal with which the signal is mixed. With the setting of the phase

it can be decided whether the real part or the imaginary part from equation (2.80) should be considered. By keeping the cavity transmission coefficient $\hat{T}^{\text{cav}}$ calculated by equation (2.70), no approximation by assuming very small absorption ($\alpha \ll 1$, i.e. $\alpha(\nu) \ll \pi/2F$) needs to be made. Figure 2.16 shows the simulation of the NICE-OHMS signal for a single transition and different phases θ_{fm} between 0 and 2π.

Two different types of signals can be recognized. On the one hand for a phase position of a odd multiple of $\pi/2$ an absorption signal of the sidebands can be seen and a cancellation of the carrier in the range of the resonance frequency. On the other hand, for a phase of 0 or an integer multiple of π, there is a dispersion signal that has a zero crossing at the resonant frequency. Both signal types are dominated by a Doppler broadened part with a barely visible sub-Doppler signal. For a better view of the sub-Doppler signal only a single signal with a phase setting of 0 is simulated in Figure 2.17. At the position of the resonance frequency the sub-Doppler zero-crossing can be seen with a steep slope.
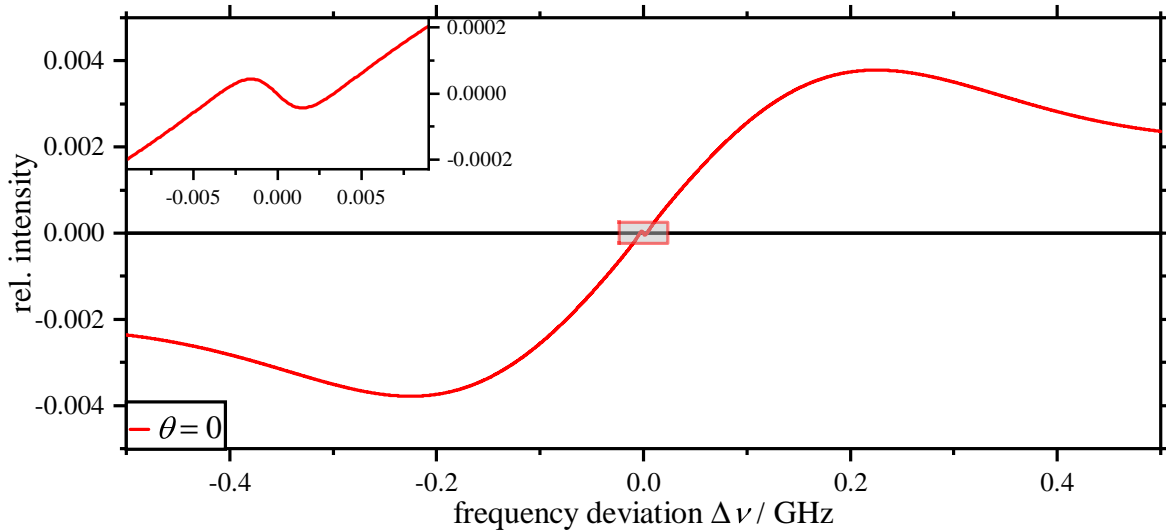

Figure 2.17: Simulated NICE-OHMS error signal with the relative intensity plotted versus the frequency deviation from the resonance of the absorption line at phase shift of $\theta_{\text{FM}} = 0$ (imaginary part of equation (2.80)) with magnification of the sub-Doppler feature at the resonance frequency.

2.5.2 NICE-OHMS with many HFS

Up to here, only single Doppler broadened with Lamb-dip transition was assumed for the simulation of the NICE-OHMS signals. As described before (see section 2.2.3),

a iodine line profile consists of several overlapping Doppler profiles of HFS (15 or 21) components with almost the same intensity. Thus, iodine differs from the other molecules (CH_4 [61], CH_3I [62], N_2O [63], C_2H_2 [64, 65]) studied so far with the NICE-OHMS method. Mostly NICE-OHMS is used there for ultra-sensitive detection or to study molecular spectra. On the one hand, in some works only spectra with one line are examined or, on the other hand, mainly weak lines which do not influence each other are detected. Here the aim is a high accuracy, which requires a detailed investigation of this influence. How do the NICE-OHMS signals change due to the many HFS lines of $^{127}I_2$? In Figure 2.18, the NICE-OHMS signal from equation (2.80) of the P(33)6-3 iodine line is simulated for different phases θ_{fm}.
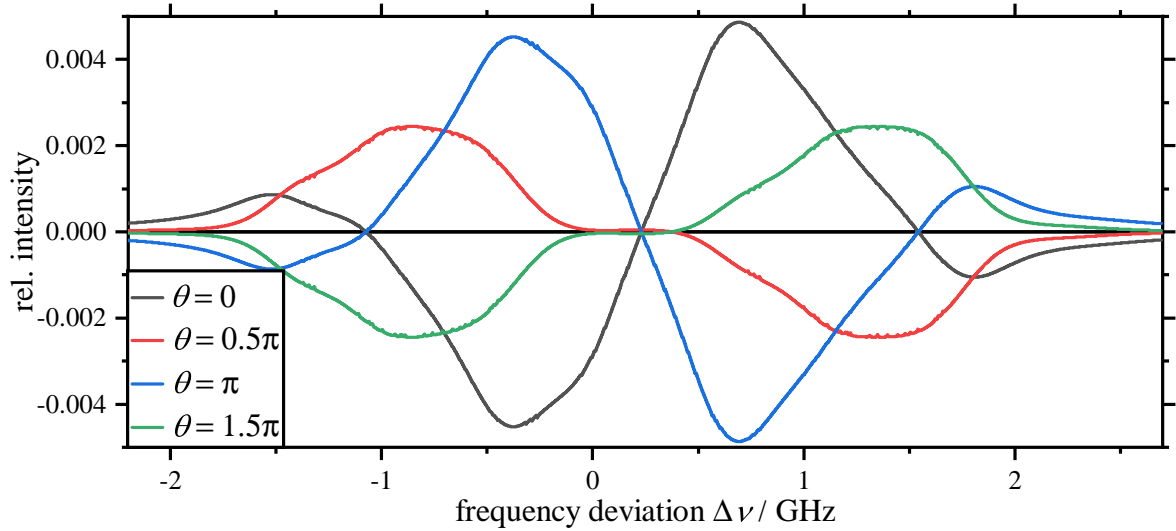

Figure 2.18: Simulated NICE-OHMS error signal with many HFS components within overlapping Doppler profiles using the iodine line P(33)6-3 as an example for different phase $\theta_{fm} = 0$.

However, the difference to a single line spectrum is that multiple resonances of the HFS components can be seen at the respective resonance frequency. The dispersion signals show a zero crossing at the frequency of the minimum of the Doppler broadened absorption profile and not at the resonance frequency of a single line. It is also noticeable that an offset from the zero line can be seen in the absorption signal at the cancellation of the carrier. Since the frequency of the laser is to be stabilized to the resonance of a single HFS component of iodine, the NICE-OHMS dispersion signal at a phase of $\theta_{fm} = 0$ is shown again in Figure 2.19.

It can be seen in this phase setting that in the transmission minimum region the
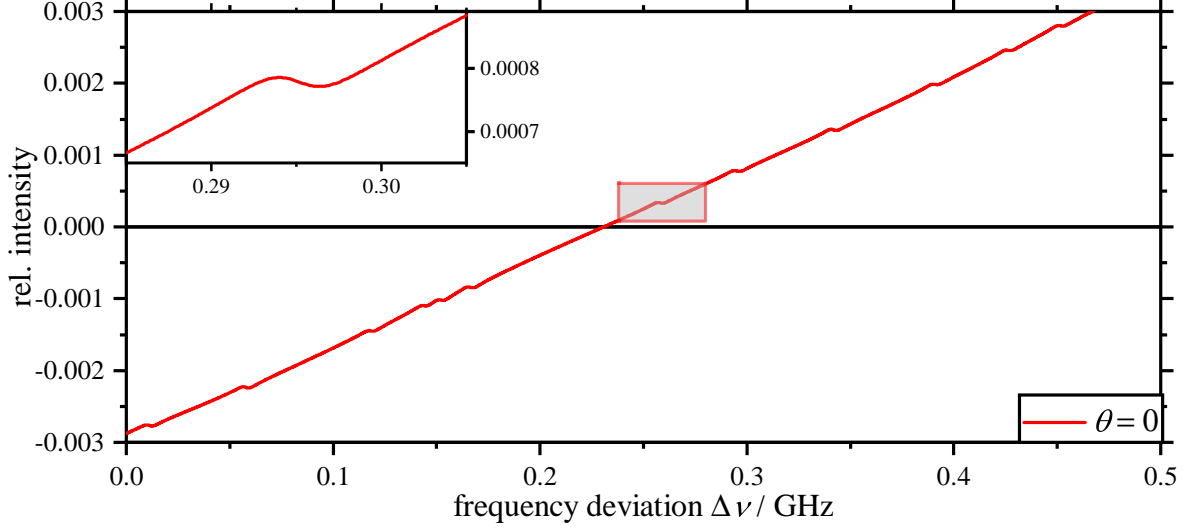
Figure 2.19: Illustration of the individual resonances of the HFS components using the example of the iodine line P(33)6-3 in the simulated NICE-OHMS error signal at a phase $\theta_{\text{fm}} = 0$.

Doppler background of the NICE-OHMS signal is approximately linear. On the Doppler broadened background the sD signals of the HFS components can be recognized. Due to the Doppler broadened background, this NICE-OHMS signal cannot be used in this form for frequency stabilization on an HFS component. The main reason is that the sub Doppler signals do not have a zero crossing and therefore no accurate reference at which the resonant frequency of the HFS component is located. Thus, this signal could only be used to stabilize the frequency of the laser to the zero crossing of the Doppler broadened signal.

To suppress the Doppler broadened background a further wavelength modulation (wm) is applied and corresponding modulation at the n-th harmonic of the NICE-OHMS signal is detected with a lock-in amplifier. Since the laser frequency follows the length of the cavity due to PDH stabilization, the wavelength modulation is performed by modulating its length at a frequency f_{wm}. The obtained wm-NICE-OHMS error signal can then be described as follows [63]:

$$\epsilon_{\text{wm}} = \int_0^{2\pi} S_A^{\text{NO},\nu_{\text{m}}} \left[\nu + \Delta\nu_{\text{wm}} \cos(x) \right] \cdot \cos(n \cdot x) \, \mathrm{d}x \qquad (2.81)$$

It is assumed that the NICE-OHMS system can follow the wm modulation instantaneously in time. Thus $x = f_{\text{wm}}t$ is substituted and integrated over a period of 2π. $\Delta\nu_{\text{wm}}$ is the amplitude of the modulation in frequency space and n is the harmonic.

The wm-NICE-OHMS signal behaves like the *n*-th derivative of the NICE-OHMS signal and the Doppler broadened background can be suppressed [66]. Because of the symmetry of the NICE-OHMS signal, the 2nd harmonic of the wm-NICE-OHMS signal is used as an error signal to stabilize the laser frequency in this experiment. Figure 2.20 shows a simulated wm-NICE-OHMS signal of the P(33)6-3 iodine line.
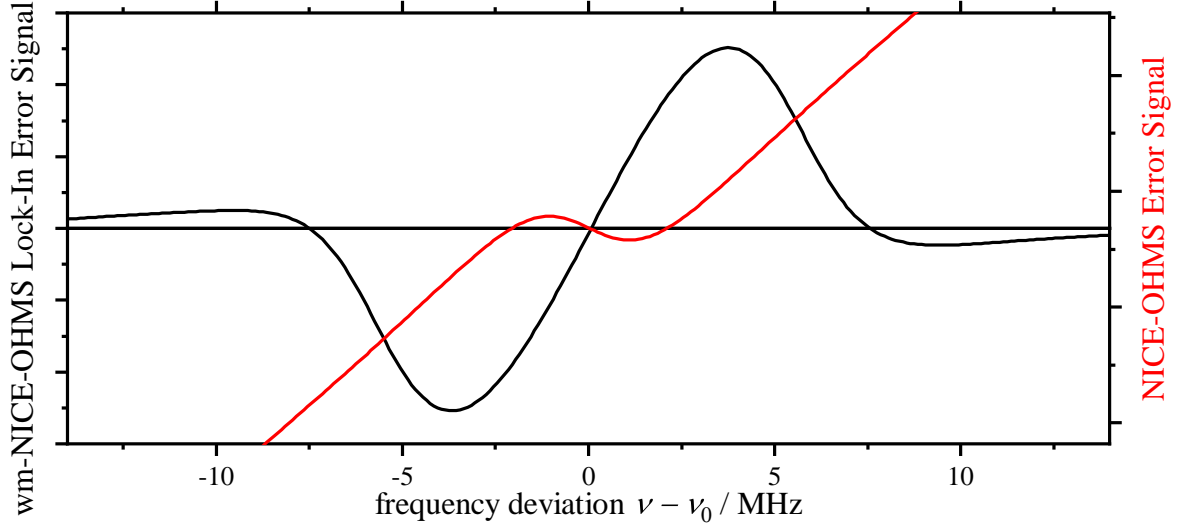
Figure 2.20: Simulated NICE-OHMS error signal (red) and wm-NICE-OHMS error signal (black) of HFS component "i" of the iodine line P(33)6-3 as a function of frequency shift.

With the wm modulation technique, the Doppler broadened background is suppressed and zero crossings with a strong slope can be seen at the resonant frequencies of the HFS components. Thus, using this wm-NICE-OHMS error signal, the frequency of the laser can be stabilized at a resonant frequency of a HFS component.

Chapter 3

Precision Frequency Measurement Techniques

This chapter presents how the frequency stability over time and the absolute frequency of a light field emitted by a laser system is determined in this thesis. The principle of a beat frequency measurement is used, where the frequency difference of two light fields can be determined [67]. In this measurement, the frequency stability of one system can be determined by comparison to a more stable reference system. Two different reference systems are used, which are presented in more detail in this chapter. The first reference system is an iodine-stabilized He-Ne laser, which can be used as a practical realization of the meter. The second system is a frequency comb that is referenced to hydrogen maser which is further referenced to a Cs atomic clock.

3.1 Helium-Neon Laser

First, a look at the current practical realization of the meter for the wavelength of 633 nm in the form of an iodine-stabilized helium neon laser will be taken [68]. The PTB helium-neon laser consists of a resonator with two mirrors (see figure 3.1). The laser medium is neutral neon that is exited in a high voltage helium-neon gas discharge. The gas is contained in a glass tube that is sealed by two Brewster windows to provide low optical loss and also ensure a linearly polarized laser emission. To stabilize the laser frequency, another gas cell containing iodine is installed inside the resonator. By using saturation spectroscopy, the frequency of the laser is stabilized on hyperfine structures of the R(127)11-5 iode line. For this purpose, the laser frequency is modulated and from the observed change in the laser power a 3f signal is generated with the use of a

lock-in amplifier. Both the frequency modulation and the tuning of the frequency itself are made possible by piezos on which the mirrors are mounted and thus the resonator length can be influenced. Due to the properties of the atomic laser medium, tuning of the frequency is limited to a few 100 MHz, so that the laser can only be stabilized on seven HFS lines of the R(127) 11-5 iodine line.
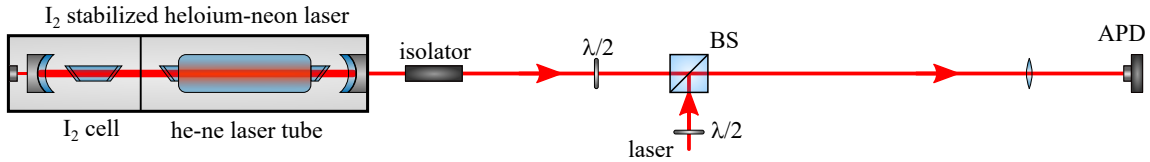
Figure 3.1: Setup of an optical beat frequency measurement for frequency comparison to an iodine stabilized He-Ne laser. On the left side the He-Ne laser is shown, consisting of two mirrors, iodine cell and He-Ne laser tube. The measurement setup consists of the beam paths of the two lasers, half-wave plates ($\lambda/2$), a beam splitter (BS), a focusing lens and an avalanche photo diode (APD).

In order to measure the frequency or stability of another laser using the iodine-stabilized He-Ne laser, the beat frequency of the emitted light fields of both lasers is investigated. Figure 3.1 shows a sketch of the corresponding setup. The light field of the He-Ne laser and the laser to be examined are superimposed with a 50:50 beam splitter with similar beam shape and polarization. To adjust the polarization of the light field, a half-wave plate is placed in front of both inputs of the beam splitter. To avoid back reflections to the He-Ne, which disturb the stability of the laser, an optical isolator is used. The beat signal of both superimposed fields is detected by an avalanche photodiode (APD). Since only frequencies of a few GHz can be measured with this kind of APD, only lasers with a frequency close to the frequency of the He-Ne can be investigated. The frequency of the beat signal is either observed directly with a frequency analyzer or measured with a fluke PM6681 counter over time. The counter is set to average the measured frequency over one second intervals. The instability of the beat is $\sigma_{beat}^2 = \sigma_1^2 + \sigma_2^2$ thus the stability of the beat frequency is dominated by the more unstable laser.

Figure 3.2 shows the instability of an iodine-stabilized He-Ne of PTB in terms of the Allan deviation (see section 3.2).

The iodine-stabilized He-Ne laser studied here shows an instability of $\sigma_y = 4.4 \cdot$
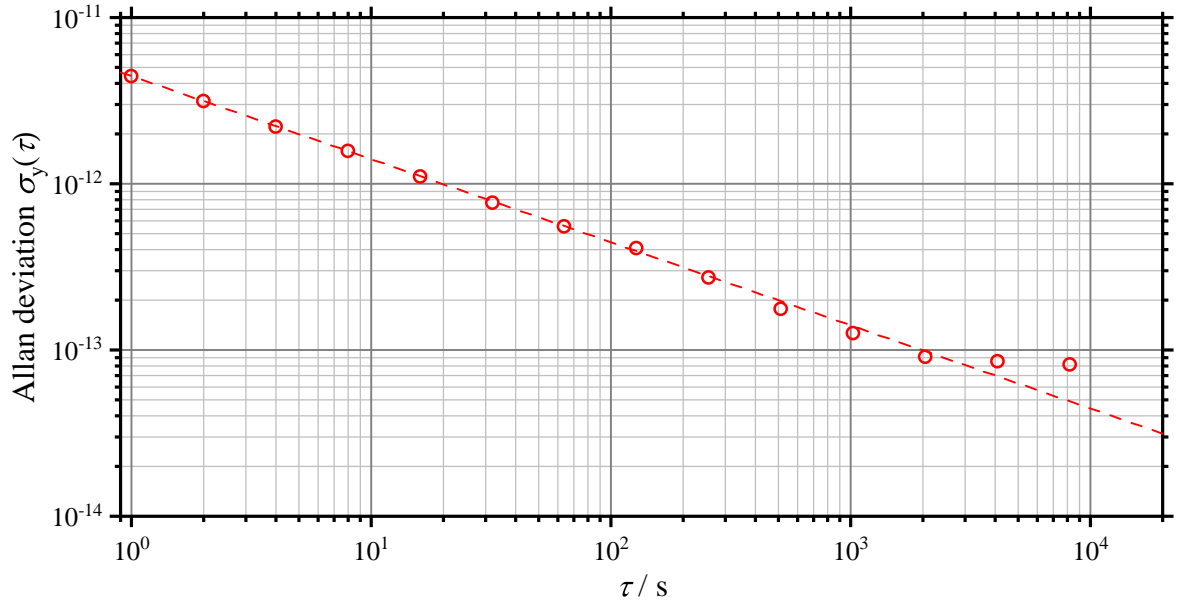
Figure 3.2: Allen deviation $\sigma_{\text{y}}(\tau)$ as a function of a time interval of an iodine stabilized He-Ne of PTB inferred from an optical frequency measurement with a comb in comparison to hydrogen maser.

$10^{-12} \cdot \tau^{-1/2}$ in the time interval up to $\tau = 3000\,\text{s}$ (dashed red line). This agrees well with the instability of down to $\sigma_{\text{y}} = 1.1 \cdot 10^{-11} \cdot \tau^{-1/2}$ determined from the comparison of different iodine-stabilized He-Ne lasers [69]. Here it must be taken into account that in [69] only He-Ne lasers were compared with each other and the results drawn above are from a beat frequency measurement with a frequency comb (see section 3.2). A comparison between two He-Ne lasers with the same frequency instability results in a value of $\sqrt{2}$ as large for the resulting frequency instability of the beat frequency.

3.2 Frequency Comb

The second method used in this work to measure absolute frequency and frequency stability is a frequency measurement via an optical frequency comb to a hydrogen maser. With the help of the frequency comb it is possible to transfer the frequency of a light field in the THz range, which is difficult to measure, into the microwave range (MHz), which is easy to measure. The the stability and absolute frequency of the frequency comb is traced back to a primary frequency standard in the form of two cesium atom clocks of the PTB with the help of a hydrogen maser. Figure 3.3 shows the schematic structure of the frequency comparison between the frequency comb and

the laser under investigation. The comb spectrum is generated with an Er:fiber-based fs-laser oscillator (MenloSystems Mcomb 1550 ULN) [70]. Here, the center wavelength of the spectrum is 1560 nm. With an Er-doped fiber amplifier (EDFA) the emitted comb spectrum is amplified. Subsequently, the frequency is doubled with a second harmonic generation (SHG), so that a spectrum around the wavelength of 780 nm is generated. Finally, the spectrum is broadened with a non-linear fiber (NLF) to a super-continuum, which has a wavelength range of 600-750 nm [71].
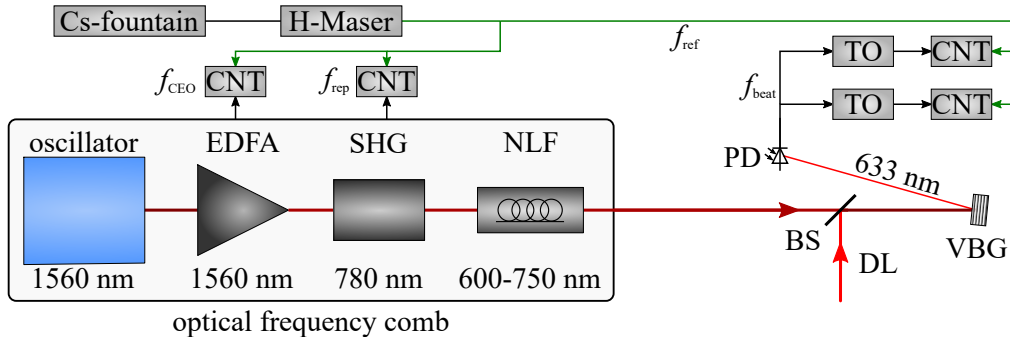

Figure 3.3: Sketch of the optical frequency measurement by means of a frequency comb. On the lower left side the frequency comb is shown with the oscillator, Er-doped fiber amplifier (EDFA), second-harmonic generation (SHG) and a nonlinear fiber (NLF). The optical setup consists of a beam splitter (BS), the diode laser (DL), volume Bragg grating (VBG) and a photo diode (PD). To measure the frequencies f_{CEO},f_{rep} and f_{beat}, frequency counters (CNT) and tracking oscillators (TO) are used, which are referenced by the combination of CS-Fontaine and H-Masser with f_{ref}.

Figure 3.4 shows an example of the comb spectrum. It shows the intensity I of the comb lines over the absolute frequency ν.

The spectrum of the comb consists of repeating lines, which have a fixed frequency spacing. This distance is called repetition rate f_{rep}. Due to the dispersion of the fs-laser oscilator the comb lines are shifted by the carrier-envelope offset frequency f_{CEO}, which is determined by a beat measurement between the actual comb spectrum and the frequency-doubled comb spectrum. The number n indicates the number of the comb line. The interference between the comb and the light of a laser gives the beat frequencies with certain individual comb lines. However, only the smallest beat frequency f_{beat}^{comb} between the frequency of the light of the laser and the nth comb line is used. From this beat frequency f_{beat}^{comb} the absolute frequency ν of the light field of
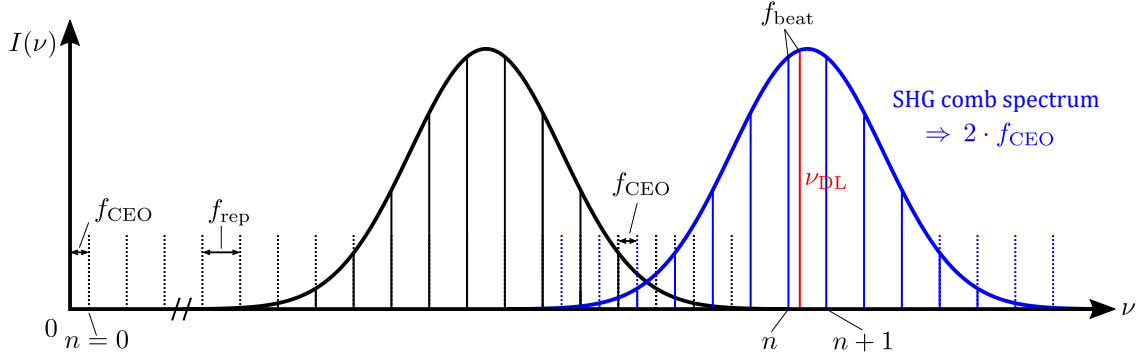
Figure 3.4: Sketch of the comb spectrum plotted versus frequency ν. Here n denotes the comb mode, f_{CEO} the carrier-envelope offset frequency, f_{rep} the repetition rate, f_{beat} the beat frequency and ν_{DL} the frequency of a laser system.

the laser to be examined can be calculated as follows:

$$\nu = 2f_{CEO} + n \cdot f_{rep} \pm f_{beat}^{comb}. \tag{3.1}$$

f_{CEO} and f_{rep} are also recorded by K+K FXE counters. Due to the frequency doubling, the shift by f_{CEO} must be considered twice (see figure 3.4). To determine the sign of the beat frequency f_{beat}^{comb} and the mode number n, the frequency of the laser to be examined must be already known with an accuracy of few 10 MHz.

All counters on the frequency comb are referenced to a frequency f_{ref}^{H}. This signal comes from an H-maser, which is further referenced to the PTB's primary Cs atomic clocks. Thus the frequency is traceable to the definition of SI unit of time and frequency. The effective instability of the Cs fountains in everyday operation is $\sigma_{CS} = 2.5 \cdot 10^{-13} \, (\tau/s)^{-1/2}$ with an accuracy of $2.7 \cdot 10^{-16}$ [72]. The hydrogen maser has a slightly lower instability over all averaging times [73, 74]. The frequency comb itself reaches instabilities of $\sigma_{comb} < 10^{-15}$ by comparing different frequency combs with each other [70].

To obtain the beat frequency f_{beat}^{comb} between the super continuum and the light of the laser DL to be measured, both fields are superimposed on a beam splitter BS. In order to improve the signal-to-noise ratio, only comb lines in the wavelength range of 633 nm are considered. For this purpose, a volume Bragg grating (VBG) is used to filter out only a few GHz wide range around 633 nm from the continuum spectrum. The beat with the filtered light field is detected by a photodiode. The beat frequency f_{beat}^{comb} is band-pass filtered with a tracking oscillator (TO), that phase-locks a voltage controlled oscillator to the beat signal. Then the frequency is recorded with a counter

(CNT) in Π-averaging or Λ-averaging mode (K+K FXE) [75]. To identify possible problems of cycle slips due to the frequency modulation of the studied laser in this work, two TOs and CNTs are used here. The TOs are operated with slightly different settings. If both counters agree, it is ensured that the frequency of the beat with the modulated laser is tracked correctly. Using the deviation of both counters, the error introduced by the beat measurements can be estimated. A deviation of a few hundred mHz results in a measurement accuracy of the frequency over 1 s of $\Delta\nu/\nu \approx 10^{-15}$.

To study the instability of the frequency of the laser light over time, the Allan variance $\sigma_y^2(\tau)$ is determined based on the measured frequency deviation [76, 77]. Generally, the Allan variance can be considered as half of the variance between neighboring 2-sample averages $\overline{y}$ of duration τ.

$$\sigma_y^2(\tau) = \left\langle \frac{\left(\overline{y}_{k+1} - \overline{y}_k\right)^2}{2} \right\rangle \tag{3.2}$$

Here gives k the index of the kth averages value in the time interval τ. The square root of the Allan variance results in the Allan deviation:

$$\sigma_y(\tau) = \sqrt{\sigma_y^2(\tau)} \tag{3.3}$$

Now we still have to consider how the values are averaged [75]. In the so called Π mode, all values are averaged equally. For this type of averaging, the normal Allan deviation is used for the analysis. Whereas in Λ mode a weighted averaging with a triangle weighting function is used. For this kind of averaging the modified Allan deviation $\text{mod}\,\sigma_y(\tau)$ is obtained [78]. Depending on the spectrum of the frequency fluctuations, the modified and the standard Allan deviation differ by a certain factor [79]. For example for white noise the modified Allan deviation $\text{mod}\,\sigma_y(\tau)$ is converted into the general Allan deviation $\sigma_y(\tau)$ by multiplying the factor $\sqrt{2}$ (see section 4.2.2).

Chapter 4

Toptica Beta Demonstrator

In this chapter, a shoe box sized diode laser system from Toptica is presented that is stabilized to iodine lines by Doppler broadened spectroscopy. Thereby, the laser system can be stabilized on a large number of different iodine lines in a broad frequency spectrum of several hundred GHz frequency in a range of 633 nm. With such a system the possibilities as a substitute of simple helium-neon lasers in the field of interferometric length measurement and metrology applications shall be investigated. The design of the laser system will be explained in detail, the frequency instability over time and the absolute frequency will be analyzed. Also the influences of the molecular structure of iodine on the frequency instability are investigated. This chapter expands and supplements the results published in [80]. In contrast to that publication, instead of an approximated transmission ($T^{\mathrm{A}} \approx 1 - [L_{\mathrm{cell}}\alpha]$) for small absorption α, the exponential function is used ($T^{\mathrm{A}} = e^{-L_{\mathrm{cell}}\alpha}$) for the estimation of the stability. In addition the correct modified Allan deviation for the two-mode and Zeeman stabilized He-Ne is shown in figure 4.6. However, these changes in the values do not affect the conclusions drawn in the publication.

4.1 Setup of the Laser System

This section shows the optical setup of the Toptica Beta Demonstrator and its basic properties. Also the stabilization of the frequency on the Doppler broadened absorption spectrum of iodine is shortly presented.

4.1.1 Optical Setup

The Toptica Beta demonstrator combines a distributed-feedback (DFB) laser diode and an iodine cell and employs Doppler broadened spectroscopy to stabilize the frequency of the laser light. A schematic of the setup is shown in Figure 4.1.
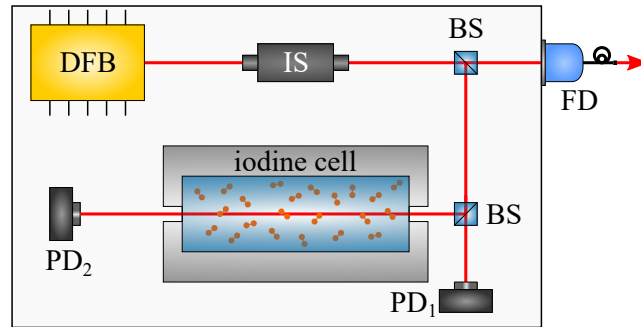

Figure 4.1: Sketched optical setup of the Toptica Beta demonstrator, with the distributed feedback diode laser (DFB), the isolator (IS), beam splitters (BS), Toptica fiberdock (FD), the iodine cell with encased heater and the photodiodes PD_1 and PD_2.

An optical isolator IS is used to prevent reflections back into the diode, that would disturb the frequency stability of the laser diode. Behind the isolator, the light (power around 10 mW) is divided with a 90:10 beam splitter. The main part of the power is coupled into a polarization maintaining fiber by a Toptica fiberdock FD to serve as output of the laser system. Depending on the optical frequency, an output power of around 4.5 to 6.5 mW is achieved. The reflected part of the light (around 1 mW) is used for iodine spectroscopy and frequency stabilization of the laser light. With photodiode PD_1, the power of the light transmitted by the second 90:10 beam splitter is measured to serve as a reference signal for the spectra. With the photodiode PD_2 the transmission of an iodine absorption cell with $^{127}I_2$ is measured. A power of around 0.1 mW is used for the spectroscopy itself. To control the vapor pressure and the thermal occupancy of the nuclear levels inside the iodine cell, it is located in a temperature controlled housing. In order to achieve a good balance between the required heating power and strong absorption lines (50 %) of iodine, the cell is heated up to 60 °C. The iodine cell itself has a length of 3.3 cm and the estimated saturation iodine vapor pressure is 616 Pa inside the cell according to equation (2.4) and the pressure data of Honig in table 2.2.

Figure 4.2 (a) shows the 27 cm × 15 cm housing with the fiberdock in which the laser system is set up and Figure 4.2 (b) displays the interior with the individual components and electronics.

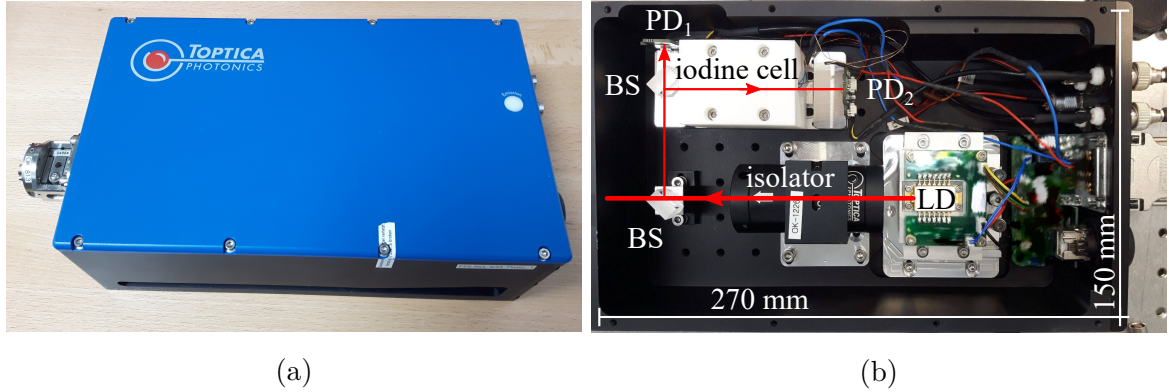<div align="center">(a)   (b)</div>

Figure 4.2: Photos of the shoebox-sized housing of the Beta demonstrator with connected fiberdock (a) and the internal setup (b) with the beam path drawn in (red), laser diode (LD), beam splitter (BS), and the photodiodes (PD).

By varying the diode temperature in a range between 12 °C and 20 °C, the frequency of the laser diode can be tuned over an interval of more than $\Delta \nu = 245\,\mathrm{GHz}$. In comparison a change of the laser diode current has only a very small influence on the frequency (1 GHz per 1 mA, [19]). Thus to avoid power fluctuations the temperature is used to scan the laser frequency.

4.1.2 Doppler Broadened Frequency Stabilization

In order to stabilize optical frequency of the laser diode to the center of a Doppler broadened iodine line, first the transmission spectrum of iodine was determined, by tuning the temperature of the diode between 12 °C and 20 °C. The transmission of light through the iodine cell is measured with photo diode PD_2. Since the output power of the laser changes with the temperature of the diode, the power in front of the iodine cell is recorded with PD_1 to calculate the normalized transmission T^{TBD}. Figure 4.3 shows the transmission spectrum T^{TBD} of the iodine cell determined in the above way.

After scanning the iodine spectrum, an iodine line can be selected from the transmission spectrum T^{TBD} and the laser is stabilized automatically to this line by the controller software. For the frequency stabilization the laser frequency is modulated via the current. In this work a modulation frequency of 21 kHz with a peak-to-peak
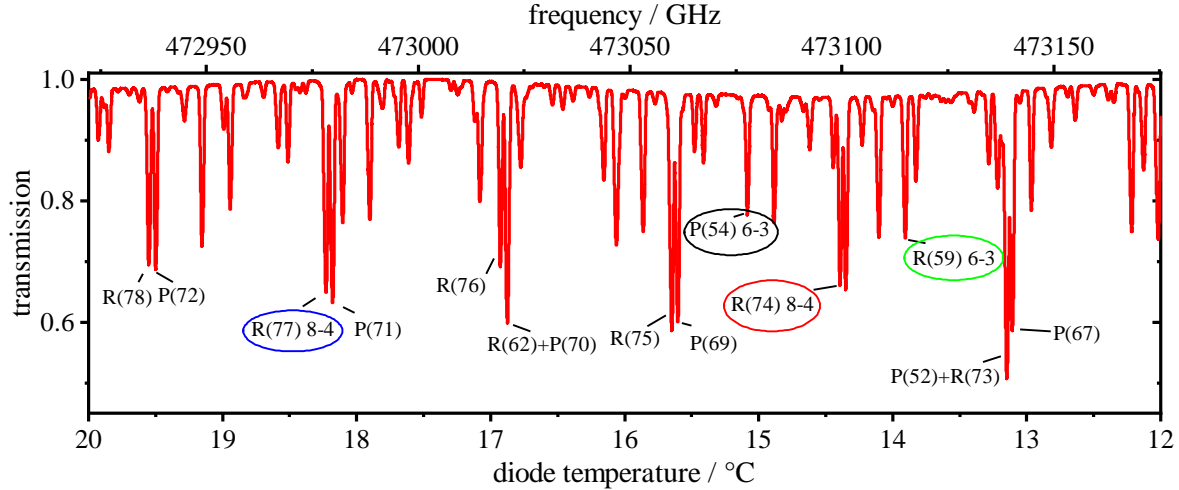
Figure 4.3: Normalized transmission spectrum of iodine measured with the Beta Demonstrator plotted versus diode temperature and optical frequency. The stronger Doppler broadened iodine lines are labeled and the lines studied in this work are color-coded.

frequency deviation of 5 MHz is used. Using a 1-f lock-in technique, an error signal is generated. The generated error signal is fed to a PID servo amplifier [81] to stabilize the laser frequency to a selected iodine line by feedback to the current and temperature.

4.2 Simulation and Experimental Results

In the following part, the measurement results of the investigations of the Toptica Beta Demonstrator are shown. The absolute frequency as well as the instability of the laser system stabilized on different iodine lines will be discussed. These results will be compared with simulations based on the data of the "Iodine Spectrum" program. Finally, the obtained results are explained by means of the structure of the iodine molecules.

4.2.1 Simulation of Doppler Broadened Iodine Spectra

To verify the experimental results, transmission spectra are simulated using the data in the form of frequency and absorption coefficient from the "Iodine Spectrum" program. As described in chapter 2.2.1, each line of the transmission spectrum of iodine consists of a superposition of many molecular hyperfine transition. As the iodine cell is heated

to a temperature of 60 °C, in addition to Doppler broadening ($\gamma_{DB} = 388\,\text{MHz}$) the pressure inside the vapor cell causes a collisional line broadening of $\gamma_{co} = 76.6\,\text{MHz}$. Thus, this can no longer be neglected and a Voigt profile must be used here in this chapter to simulate the spectra. In the simulation it is calculated as the real part of the Faddeeva function [48] (see section 2.2.3). The absorption coefficient is adjusted to match the transmission spectrum shown in Figure 4.3. Using the simulated Doppler broadened transmission spectra, the frequency ν_{sim} of the maximum absorption of each iodine line is determined and the curvature κ_{sim} is approximated at this point. Also, due to the high pressure of 616 Pa at the temperature of 60 °C, there is a shift in the resonant frequency. This results in a shift of approx. -5.9 MHz. The shift was determined from a scaling of the results of a He-Ne laser stabilized on the line R(127) 11-5 [82]. The pressure shift for the He-Ne is -9.5 kHz/Pa at a temperature of 15 °C (18 Pa) in the cold finger.

4.2.2 Frequency Measurement

In order to investigate the frequency stability and the absolute frequency of the light of the laser stabilized on different iodine lines, a frequency comb (see section 3.2) is used. The laser is stabilized to four different representative lines from the iodine spectrum covering the frequency of the laser (see Figure 4.3) to which . Two of the iodine lines consist of 15 HFS components and two consist of 21 HFS components to investigate if and how the structure of the HFS components affects the instability of the laser. Also the influence of the line intensity is investigated. For each type of line, one with stronger ($T_0^{TBD} = 0.66$) absorption and one with weaker absorption ($T_0^{TBD} = 0.76$) is selected. Lines P(54) 6-3 (weak intensity) and line R(74) 8-4 (strong intensity) are picked for the case of 15 HFS components and line R(59) 6-3 (weak) and line R(77) 8-4 (strong) for the case of 21 HFS components.

For all given lines the beat frequency ν_{beat}^{TBD} to a suitable comb mode of the frequency comb is measured over time. In this measurement the counters are in Λ-averaging mode with synchronous 1 s counting intervals. Using equation (3.1), the absolute frequency ν^{TBD} of the laser light from the TBD is calculated from the measured beat frequency for all four lines. The deviation from the respective average frequency ($\nu^{TBD} - \nu_0^{TBD}$) over a period of two hours for all four lines is shown in fig. 4.4.

To better visualize the course of the measured frequencies, a moving average over 10 s is also shown in fig. 4.4. It can be observed that the frequency noise for both the
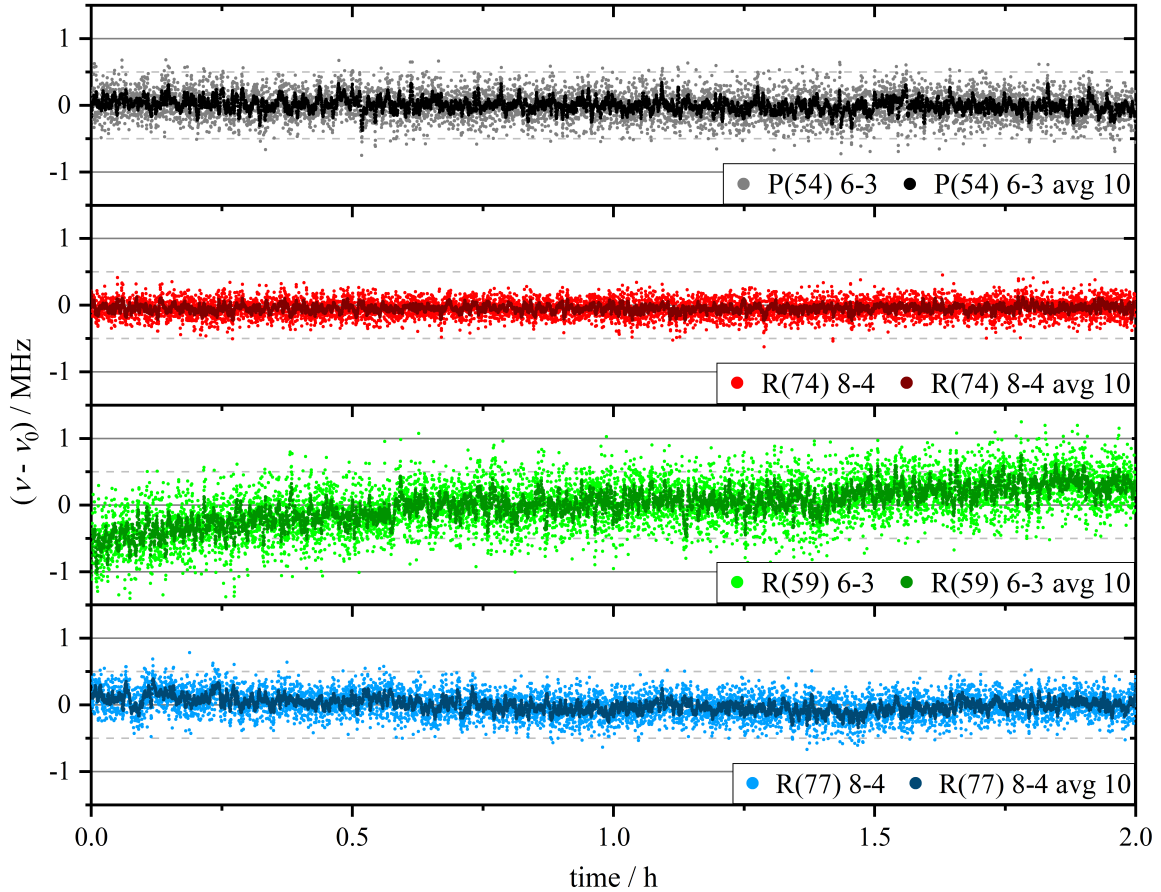
Figure 4.4: Measured frequency of the beta demonstrator stabilized on 4 different Doppler broadened iodine lines: P(54) 6-3 (black), R(74) 8-4 (red), R(59) 6-3 (green) and R(77) 8-4 (blue). The deviation of the optical frequency ν of the laser light from the measured average frequency ν_0 over time is shown. Both the 1 s values and the 10 s moving average is shown to visualize the temporal behavior.

lines with 15 HFS and the lines with 21 HFS components is smaller for the line with higher intensity (R(74) 8-4 (red) and R(77) 8-4 (blue)) in the transmission spectrum than for the line with weaker intensity(P(54) 6-3 (black) and R(59) 6-3 (green)). It can also be seen that for similar intensity of the iodine line, the frequency instability over longer times varies less for lines with 15 HFS (R(74) 8-4 (red) and P(54) 6-3 (black)) than for lines with 21 HFS components (R(77) 8-4 (blue) and R(59) 6-3 (green)). To investigate the instability of the frequency over a much longer period of several days, the measurement described above is repeated for line R(74)8-4. Line R(74)8-4 is selected because it showed the best frequency stability in the measurement over 2 hours. The

evaluated frequency deviations from the average frequency are shown in Figure 4.5.
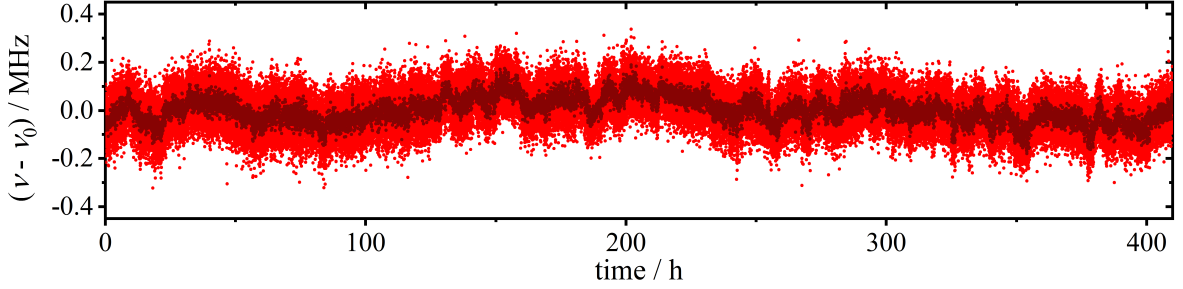

Figure 4.5: Long-term frequency measurement of the beta demonstrator stabilized on the Doppler broadened iodine line R(74) 8-4 over several days. The deviation of the measured average frequency ($\nu_0 = 473\,099\,403.6(1)\,\mathrm{MHz}$) is shown over time for 1 s counting intervals (red) and the moving average over 10 s (dark red).

From the long-term measurement, it can be seen that the laser remains stabilized on an iodine line for several days without falling out of lock. It can be seen that the 10 s averaged frequency fluctuates in a range of $\pm 0.15\,\mathrm{MHz}$ around the average frequency. Table 4.1 shows the results of the four iodine lines tested. The deviation $\Delta\nu$ of the measured average frequency ν_0 from the simulated frequency ν_{sim} is less than $\pm 10\,\mathrm{MHz}$. Thus we expect that, using the data from the "Iodine Spectrum" program and the model presented in this work the optical frequency of the laser can be predicted with similar accuracy for any iodine line.

Linie	N_{HFS}	ν_0 / MHz	ν_{sim} / MHz	$\Delta\nu$ / MHz	T_{min} / %
P(54) 6-3	15	473 077 641.3(2)	473 077 638.4	2.9	78
R(74) 8-4	15	473 099 403.6(1)	473 099 406.6	-3.0	66
R(59) 6-3	21	473 114 765.8(4)	473 114 756.9	8.9	74
R(77) 8-4	21	472 978 055.3(2)	472 978 054.5	0.8	65

Table 4.1: Comparison of the results of the four investigated iodine lines, showing the number of hyperfine transitions (HFS), the measured average frequency of the laser ν_0, the frequency position of the simulated minimum ν_{sim}, the difference $\Delta\nu = \nu_{\mathrm{c}} - \nu_{\mathrm{sim}}$ and the measured minimum transmission T_{min}.

4.2.3 Frequency Stability

For a more detailed analysis of the frequency stability, the modified Allan deviation $\mathrm{mod}\,\sigma_y(\tau)$ is calculated from the beat frequency data according to [78] for all four investigated iodine lines (see figure 4.6 and compare section 3.2).
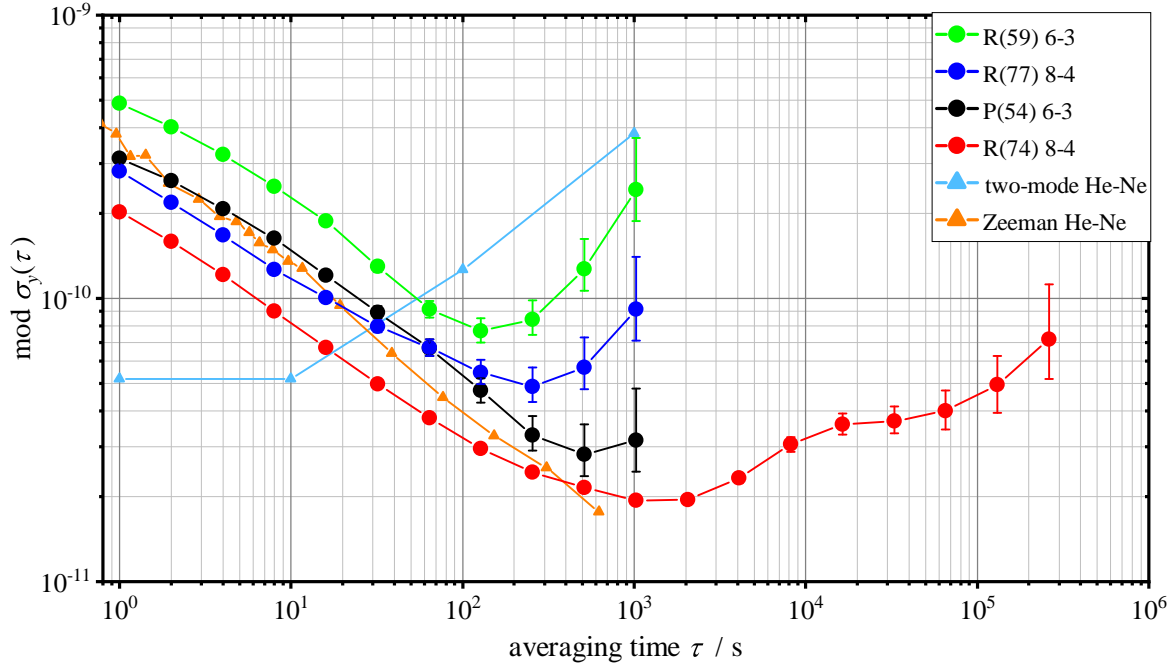
Figure 4.6: Modified Allan deviation of the beta demonstrator stabilized on various Doppler broadened iodine lines as function of the averaging time. For comparison the data of a two-mode [83] and a Zeeman He-Ne [84] are shown.

For short averaging times, the instability decreases proportional to $1/\sqrt{\tau}$, which corresponds to white frequency noise. In contrast, the instability increases again for longer averaging times of $\tau > 100...1000\,\mathrm{s}$. Also shown are the Allan deviations of a Zeeman He-Ne [84] and a two-mode He-Ne laser [83] as a comparison to current technology. In order to compare the Allan deviation of the Zeeman He-Ne laser with the modified Allan deviation of this work, its Allan deviation is corrected by a factor of $\mathrm{mod}\,\sigma_y(\tau)/\sigma_y(\tau) = 1/\sqrt{2}$, since the stability is limited by white frequency noise [79]. For the two-mode He-Ne, the Allan deviation is corrected up to an averaging time $\tau < 10\,\mathrm{s}$ with factor $\mathrm{mod}\,\sigma_y(\tau)/\sigma_y(\tau) = \sqrt{0.67}$ due to flicker noise and for larger averaging times with factor $\mathrm{mod}\,\sigma_y(\tau)/\sigma_y(\tau) = \sqrt{0.82}$ due to a random walk behavior [79].

In the following, the SNR of the error signal is calculated to derive the expected short-time stability. The transmission T near the line center ν_0 can be described by a Taylor expansion with curvature $T''(\nu_0) = \kappa_{\text{sim}}$ for the TBD:

$$T(\nu) \approx T(\nu_0) + \frac{\kappa_{\text{sim}}}{2} \left(\nu - \nu_0\right)^2 \tag{4.1}$$

The photo detector PD_2 converts the optical power P to a photocurrent I_S with a sensitivity $S_{\text{PD}} = \frac{e \cdot \eta}{h \cdot \nu_0}$ with the quantum efficiency η of the detector, the electron charge e and the Planck constant h. Here, the constant frequency ν_0 is used, since small optical frequency changes of a few GHz have little effect on the sensitivity S_{PD}. Since the optical power P depends on the transmission $T(\nu)$ of the iodine cell, the following relationship for the photocurrent I_S to the optical frequency ν is obtained:

$$I_S(\nu) = S_{\text{PD}} \cdot P_0 \cdot T(\nu). \tag{4.2}$$

To generate the 1f-rms error signal, the optical frequency of the laser is modulated around the resonance peak and with a root-mean-square modulation amplitude $\Delta\nu_{\text{mod}}^{\text{rms}}$ (here $\frac{5}{2\sqrt{2}}$ MHz). The Fourier-component at 1f of the photocurrent I_S^{1f} at the modulation frequency corresponds the error signal, which is:

$$I_S^{\text{1f}}(\nu) = S_{\text{PD}} \cdot P_0 \cdot T'(\nu) \cdot \Delta\nu_{\text{mod}}^{\text{rms}} = S_{\text{PD}} \cdot P_0 \cdot \kappa_{\text{sim}} \left(\nu - \nu_0\right) \Delta\nu_{\text{mod}}^{\text{rms}}. \tag{4.3}$$

The slope $D = \mathrm{d}I_S^{\text{1f}}/\mathrm{d}\nu$ is given by:

$$D(\nu_0) = S_{\text{PD}} \cdot P_0 \cdot \kappa_{\text{sim}} \cdot \Delta\nu_{\text{mod}}^{\text{rms}} = \frac{\eta e P_0}{h \nu_0} \cdot \kappa_{\text{sim}} \cdot \Delta\nu_{\text{mod}}^{\text{rms}}. \tag{4.4}$$

The short-term instability $\sigma_y(\tau)$ for a laser frequency ν_{L} is estimated using the slope D of the error signal and the noise spectral power density S_I of the photocurrent near the modulation frequency [85]:

$$\sigma_y(\tau) = \frac{\sqrt{S_I}}{\sqrt{2} D \nu_{\text{L}}} \tau^{-\frac{1}{2}} \qquad \text{or} \qquad \mathrm{mod}\,\sigma_y(\tau) = \frac{\sigma_y(\tau)}{\sqrt{2}} = \frac{\sqrt{S_I}}{2 D \nu_{\text{L}}} \tau^{-\frac{1}{2}}. \tag{4.5}$$

The stability is thus inversely proportional to the transmission curvature of the absorption peak.

Using the equations from section 2.2.1, the Doppler broadened spectra of the four iodine lines are simulated and the curvatures κ_{sim} at the extrema are determined. These are then used to calculate the respective expected short term stability $\mathrm{mod}\,\sigma_y^{\text{sim}}(\tau)$ by means of equation (4.5). Here, the detector PD_2 has a sensitivity of $S_{\text{PD}} = 0.41 \frac{\text{A}}{\text{W}}$

at the wavelength of 633 nm and a power $P_0 = 88\,\mu\mathrm{W}$ in front of the iodine cell is assumed. If the electronic noise of the detector is sufficiently small, the detection noise is given by the photon shot-noise. This results in S_I for the noise spectral power density of the photocurrent I_S [86] :

$$S_I = 2eI_S = 2eP_0 S_{\mathrm{PD}} T(\nu_0)\,. \tag{4.6}$$

As the shot noise is white i.e. independent of frequency, filtering by means of a lock-in of the error signal has no influence on this kind of noise S_I [87].

Table 4.2 compares the results of the four iodine lines studied in terms of the simulated curvature κ_{sim}, measured transmission $T(\nu_0)$, expected short time stability $\mathrm{mod}\,\sigma_y^{\mathrm{sim}}(\tau)$, and instability calculated from the measured values using the $\mathrm{mod}\,\sigma_y(\tau)$ at averaging times of 1 s and 128 s.

Linie	N_{HFS}	κ_{sim} / GHz^{-2}	$\mathrm{mod}\,\sigma_y^{\mathrm{sim}}(1\,\mathrm{s})$	$\mathrm{mod}\,\sigma_y(1\,\mathrm{s})$	$\mathrm{mod}\,\sigma_y(128\,\mathrm{s})$
P(54) 6-3	15	1.72	$2.9 \cdot 10^{-11}$	$3.1 \cdot 10^{-10}$	$4.7 \cdot 10^{-11}$
R(74) 8-4	15	2.31	$2.0 \cdot 10^{-11}$	$2.0 \cdot 10^{-10}$	$3.0 \cdot 10^{-11}$
R(59) 6-3	21	1.01	$4.8 \cdot 10^{-11}$	$4.9 \cdot 10^{-10}$	$7.7 \cdot 10^{-11}$
R(77) 8-4	21	1.40	$3.2 \cdot 10^{-11}$	$2.8 \cdot 10^{-10}$	$5.5 \cdot 10^{-11}$

Table 4.2: Comparison of the number of hyperfine transitions (HFS), the modified Allan deviation $\sigma_y(\tau)$ at $\tau = 128\,\mathrm{s}$ and the calculated curvature κ_{sim} for the four investigated iodine lines.

In the comparison based on the expected shot noise limit $\mathrm{mod}\,\sigma_y^{\mathrm{sim}}(1\,\mathrm{s})$ of the system and that of the measured $\mathrm{mod}\,\sigma_y(1\,\mathrm{s})$, it becomes apparent that these differ by an order of a magnitude. In search for excess noise, the noise of the detector and the technical noise of the laser was investigated. The total noise is given as:

$$S_P = S^{\mathrm{SN}} + S^{\mathrm{T}} + S^{\mathrm{PD}}\,, \tag{4.7}$$

with contributions from the photon shot-noise $S^{\mathrm{SN}} \propto 2h\nu P$, technical noise of the laser diode $S^{\mathrm{T}} \propto P^2$ and electronic noise of the detector photo detector $S^{\mathrm{PD}} \propto \mathrm{const.}$ Expressed as the relative intensity noise (RIN), it is obtained for an ideal detector ($\eta = 1$):

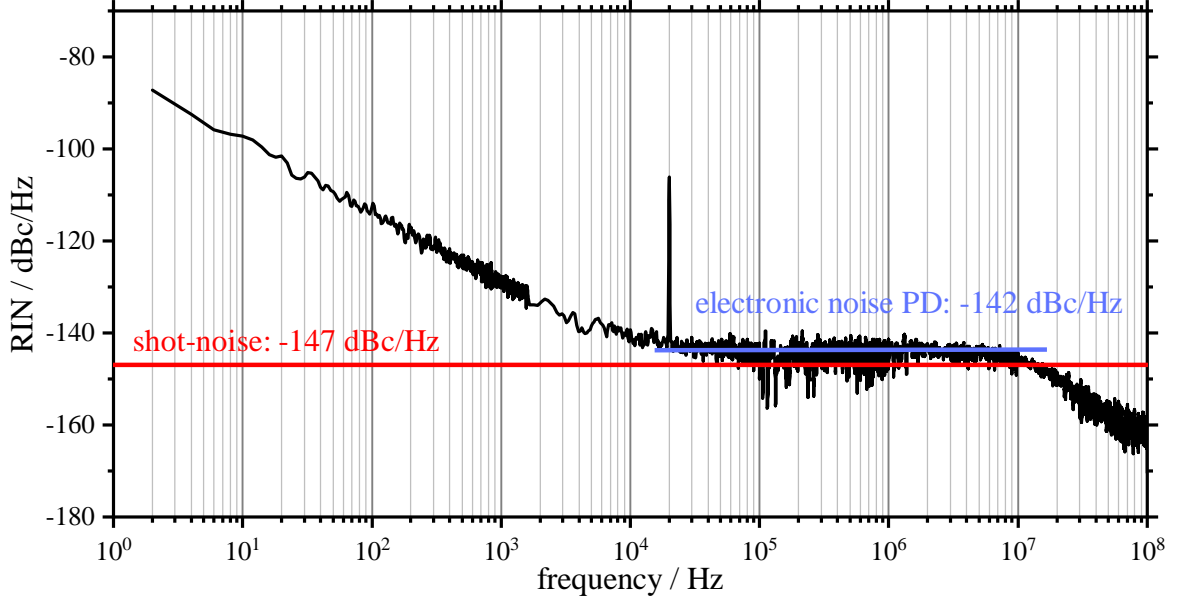$$S_{\mathrm{RIN}} = \frac{S_P}{P^2} = \frac{S_I}{I_S^2} \tag{4.8}$$

Figure 4.7: RIN spectrum of the photodetector used in the TBD. The shot-noise limit is marked in red and the electronic noise of the photodetector in blue.

Figure 4.7 shows the measured relative intensity noise RIN of the same type of modulated laser diode recorded with identical photodetector. It shows technical noise increasing towards low frequencies and white noise at higher frequencies up to the band width of the detector. The modulation frequency is already in a region, where the technical noise is sufficiently small. Also, it can be observed from Figure 4.7 that a suitable modulation frequency of 21 kHz was chosen for the used photodetector, since for lower frequency the noise is much larger than the shot-noise limit. The shot-noise in a photodetector with $\eta < 1$ leads to a RIN of:

$$S_{\mathrm{RIN}}^{\mathrm{SN}} = \frac{S_I^{\mathrm{SN}}}{I_S{}^2} = \frac{2eI_S}{I_S{}^2} = \frac{2e}{I_S} = \frac{2e}{S_{\mathrm{PD}}P} = \frac{2h\nu}{\eta P} \tag{4.9}$$

Approximately 390 μW of optical power is applied to the photodiode, which corresponds to a shot noise limit of $S_{\mathrm{RIN}}^{\mathrm{SN}} = -147\,\mathrm{dBc/Hz}$. However, at higher frequencies the measured noise is 5 dB above the shot-noise (see 4.7). Most likely it is due to electronic noise from the PD. It corresponds to a electronic current noise of $S_I^{\mathrm{PD}} = 1.62 \cdot 10^{-22}\,\frac{\mathrm{A}^2}{\mathrm{Hz}}$ according to equation (4.8).

When the laser is stabilized on line R(74)8-4, the power on PD$_1$ is smaller and has an value of $P_{\mathrm{R(74)}} = 58\,\mu$W, which corresponds to a shot-noise level of $S_I^{\mathrm{SN}} = 7.63 \cdot 10^{-24}\,\frac{\mathrm{A}^2}{\mathrm{Hz}}$ using equation (4.6). The electronic noise in this case is the same as before, since it remains constant despite higher optical power, and thus it is more than an order of

magnitude larger than the SN limit ($S_I = S_I^{\mathrm{PD}}$). On the base of the electronic noise value, equation (4.5) gives an expected instability of $\mathrm{mod}\,\sigma_y^{\mathrm{sim}}(1\,\mathrm{s}) = 9.1 \cdot 10^{-11}$ for the R(74) 8-4 iodine line, which is only a factor of $1/2$ off the measured value. The discrepancy is most likely due to variations between the photodetectors.

4.2.4 Absolute Frequency

For the iodine lines in the frequency spectrum of the laser ($472\,936.3\mathrm{GHz} < \nu < 473\,168.5\,\mathrm{GHz}$), the absolute frequency is determined using the frequency comb. For this purpose, an iodine line is selected and the frequency of the light is stabilized. A spectrum analyzer is used to evaluate the beat frequency $f_{\mathrm{beat}}^{\mathrm{comb}}$ between the comb and the laser light, and the absolute center frequency of the laser light is calculated using equation (3.1). These measurement results are compared with the obtained results from the simulation ν_{sim} of the Doppler broadened profiles.

Table 4.3 shows the results of the comparison. If the deviations $\Delta\nu$ of the absolute frequency ν_{c} from the simulated frequency ν_{sim} of the different iodine lines are considered, two influencing factors become apparent. For lines with 15 HFS components, the frequency deviation seems to be lower on average ($\Delta\nu_{15} = 5\,\mathrm{MHz}$) than for lines with 21 HFS components ($\Delta\nu_{21} = 9\,\mathrm{MHz}$). It is noticeable that weaker lines with a higher transmission seem to deviate more strongly.

Both influences also become clear when looking at the simulated curvature κ_{sim}. If the curvature is larger, the frequency deviation is generally smaller. From this it can be concluded that with smaller curvatures, as shown by the four iodine lines above, the instability becomes larger due to the poorer error signal. As the curvature becomes smaller, variations in the rms amplitude of the modulation also have a greater effect on the error signal. This can also lead to larger deviations of the absolute frequency. Due to a lower slope in the error signal, influences by electronic offsets also have a greater influence on the stability.

Linie	N_{HFS}	ν_{c} / MHz	ν_{sim} / MHz	$\Delta\nu$ / MHz	T_{min} / %	κ_{sim} / GHz^{-2}
R(58)6-3	15	473 144 856	473 144 854	2	79	1.77
R(60)6-3	15	473 083 929	473 083 931	-2	76	1.74
P(122)7-3	15	473 067 331	473 067 318	13	86	1.08
R(128)7-3	15	473 065 178	473 065 159	19	88	0.79
R(76)8-4	15	473 018 996	473 018 999	-3	69	2.42
P(56)6-3	15	473 014 374	473 014 371	3	80	1.68
R(64)6-3	15	472 955 547	472 955 546	1	79	1.95
P(58)6-3	15	472 948 959	472 948 958	1	73	2.15
R(78)8-4	15	472 936 369	472 936 374	-5	70	2.15
P(51)6-3	21	473 168 582	473 168 574	8	75	1.07
P(67)8-4	21	473 140 129	473 140 132	-3	59	1.67
P(53)6-3	21	473 108 562	473 108 554	8	74	1.01
P(69)8-4	21	473 061 021	473 061 010	11	60	1.43
R(75)8-4	21	473 059 529	473 059 537	-8	59	1.73
R(61)6-3	21	473 052 753	473 052 741	12	75	1.02
P(55)6-3	21	473 046 477	473 046 455	22	73	0.85
R(63)6-3	21	472 988 570	472 988 560	10	77	1.00
P(57)6-3	21	472 982 025	472 982 015	10	77	1.00
P(71)8-4	21	472 979 596	472 979 594	2	63	1.42

Table 4.3: Overview of the frequency measurement on different Doppler broadened iodine lines and the comparison to the expectations. Shown are the line, the number of HFS components, the measured center frequency ν_{c}, the simulated center frequency ν_{sim}, the difference of both $\Delta\nu = \nu_{\text{c}} - \nu_{\text{sim}}$, the transmission in the minimum T_{min} and the simulated curvature κ_{sim} for the 3 cm iodine cell with a temperature of 60 °C.

4.2.5 **Analysis**

When evaluating the results, it turns out that iodine lines in the considered frequency range of over 200 GHz with 15 HFS have a larger curvature than lines with 21 HFS components, if the absorption of the lines is comparable. This results in a better short-term as well as long-term stability of the iodine lines with 15 HFS components than comparable lines with 21 HFS components.

The different curvatures can be explained by the line structure of the HFS components. Figure 4.8 shows an example of the simulated transmission spectrum of the lines R(77) 8-4 (21 HFS) and R(74) 8-4 (15 HFS). In addition, the frequencies of the individual HFS components are shown.
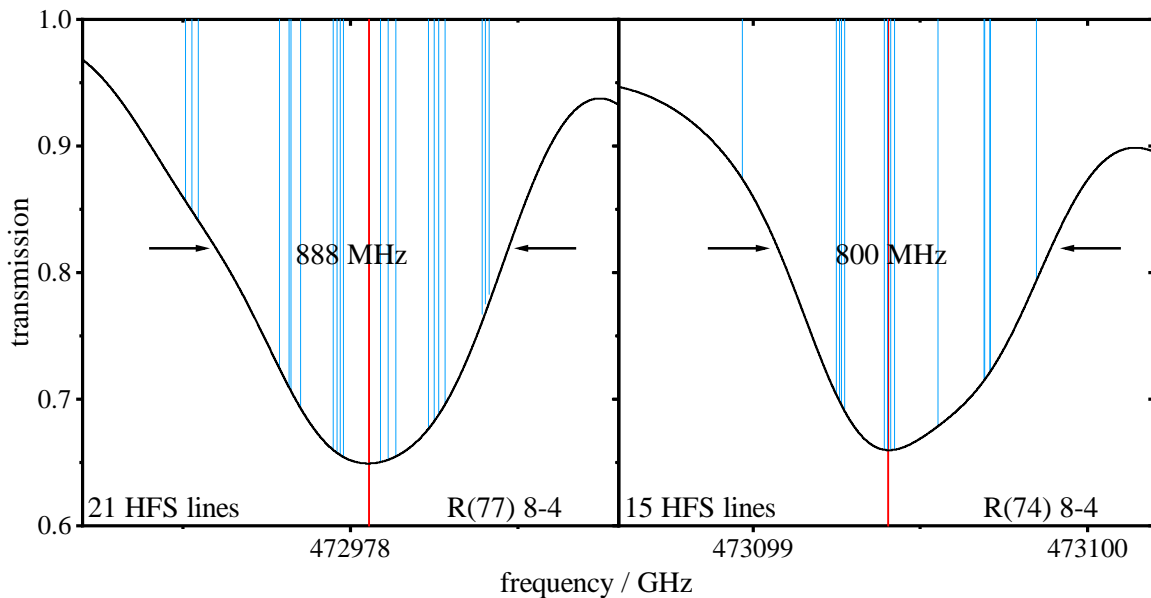

Figure 4.8: Comparison of two simulated transmission spectra of the iodine line R(77) 8-4 (left) with 21 HFS components and line R(74) 8-4 (right) with 15 HFS components. The blue lines show the frequencies of the individual HFS components, whereas the measured center frequency is drawn in red. The respective FWHM is also shown.

It is visible that the transmission spectrum consisting of 15 HFS components is narrower and sharper around the minimum than the spectrum with 21 HFS components. A grouping of the HFS components and a spacing pattern can also be seen.

The question now arises whether the pattern seen here in this example applies to all other lines in the frequency spectrum under investigation, or whether the other lines

deviate from this pattern. As described in section 2.1.3, the selection rules, the nuclear spins and the angular momentum allow only transitions with 15 HFS components for even angular momentum number J" in the ground state and 21 HFS components with an odd angular momentum number J". Thereby the shapes are depending on whether J" is even or odd. The two different HFS components arrangements are also described in [31]. This results in a sequence of (1,4,4,1,4,1) lines for 15 HFS components and a sequence of (3,4,4,3,4,3) lines for 21 HFS components. If this sequence is now compared with figure 4.8, it can be observed that for 15 HFS components in the region of the minimum just 4 and 1 components added up to the transmission spectrum, whereas for 21 HFS components 4 and 3 components are found. These 2 further components in the area of the minimum with 21 HFS components provide a broadening in this area and thus also to a smaller curvature in comparison to transitions with 15 HFS components.

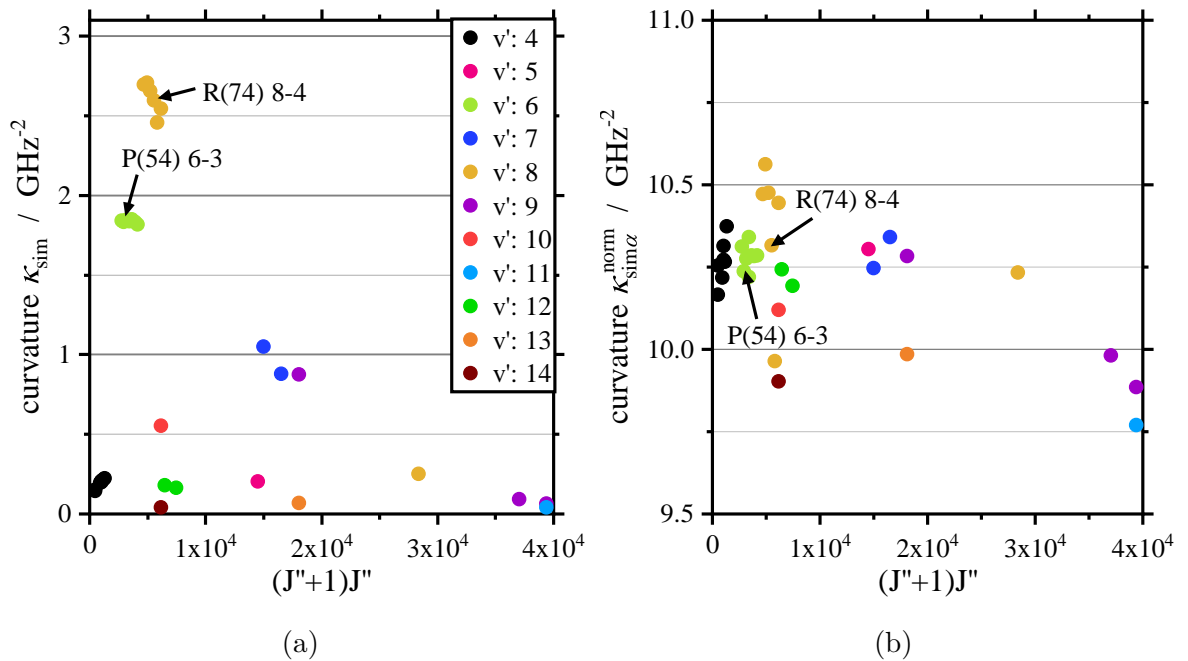(a)   (b)

Figure 4.9: (a): Simulated curvature at the peak absorption of Doppler broadened iodine lines with 15 HFS components as a function of angular momentum J" and color sorted by vibration level v'. In (b), the curvatures are normalized by the maximum of absorption of the iodine lines.

Figure 4.9a shows the curvatures κ_{sim} simulated using data from the "Iodine Spectrum" program for a larger selection in the studied frequency spectrum of iodine lines with 15 HFS components as a function of ground state angular momentum J" and sorted by the vibrational level. It can be observed that lines with the same vibrational

transition are grouped and have a similar curvature κ_{sim}. Lines with an excited vibrational level of v'=8 and a vibrational level of v"=4 in the ground state show the largest curvature κ_{sim} and lines with v'=6 and v"=3 the second largest curvature.

All lines with the same vibrational transition have a similar absorption coefficient, but the coefficients differ for different vibrational transitions. Since the intensity of the absorption lines depend on the Hönl-London factor, which is relatively constant for large J, the thermal population of the states, and the Frank-Condon factor, which is described by v and J [30].

To separate the influence of the shape of the line from the line strength, the normalized curvature off the absorption coefficient $\kappa_{sim,\alpha}^{norm} = \left|\frac{d^2\alpha}{d\nu^2}\right|/\alpha$ (see figure 4.9b) is calculated. It is visible that the normalized curvature is similar for all lines with 15 HFS components. Thus, the shape of the lines is also similar for all lines studied and this does not strongly depend on J" and v'.

For the lines with 21 HFS, an analogous procedure is followed and similar results are obtained (see Figure 4.10a and 4.10b).
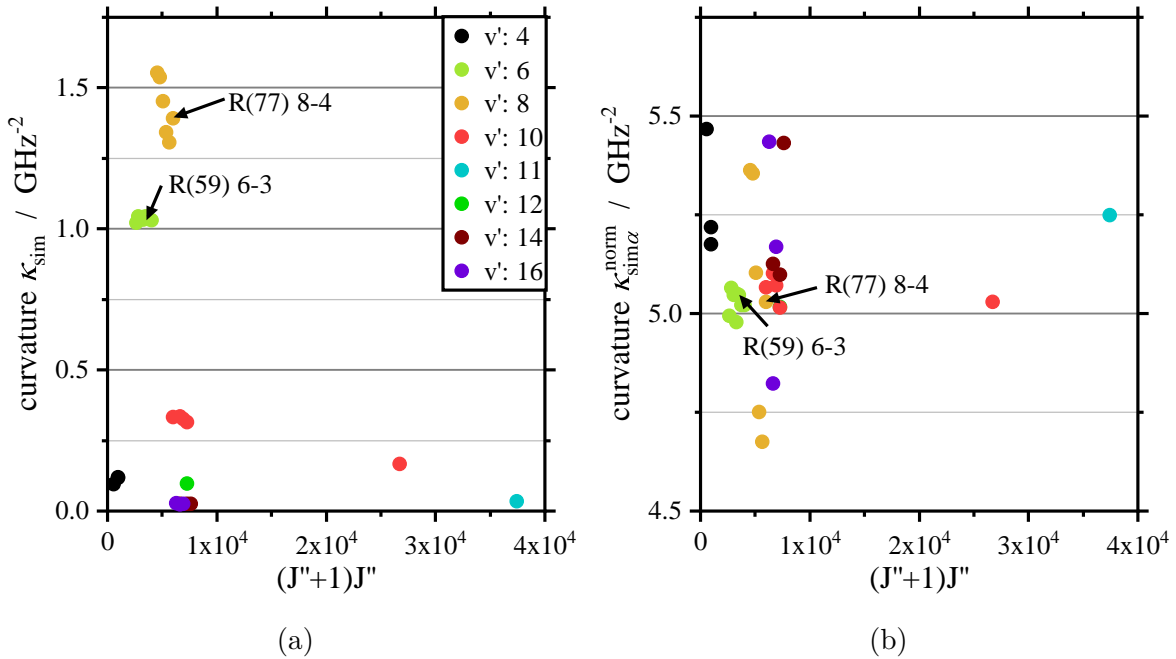

Figure 4.10: (a): Simulated curvature at the peak of transmission of Doppler broadened iodine lines with 21 HFS components as a function of angular momentum J" and color sorted by vibration level v'. In (b), the curvatures are normalized by the maximum of absorption of the iodine lines.

However, compared to the lines with 15 HFS components, the normalized curvature

$\kappa_{\text{sim}}^{\text{norm}}$ of the lines with 21 HFS components is only half as large. This indicates, that all lines with 21 HFS have a similar shape, that is different from the lines with 15 HFS components.

In summary, a compact iodine stabilized DL system is shown, which is competitive with Zeeman- and two-mode-He-Ne lasers at a wavelength of 633 nm. In contrast to He-Ne lasers, it is possible to operate the DL system over a wide frequency range above of 100 Ghz and to select the preferred Doppler broadened iodine lines for stabilization. In addition, a significant dependence of the frequency stability on the structure of the HFS components of the Doppler broadened line profiles has been found. At the same line strength, the stability of the laser stabilized on iodine lines with even angular momentum J" (15 HFS) resulted in less instability than lines with odd angular momentum J" (21 HFS).

Chapter 5

NICE-OHMS Experimental Technique

In this section of the thesis, the frequency stabilization of a diode laser to a hyperfine component of iodine is described using the NICE-OHMS method and the experimental results are evaluated and presented. First, the experimental setup in the laboratory is explained in detail. The design of the cavity used and the selection of the various components are discussed. In the second part, the frequency instabilities and accuracies achieved by the laser system are determined and the results are presented. In the last section of this chapter systematic effects are investigated, which could be the reason for the frequency deviations of the laser system.

5.1 Experimental Setup

Figure 5.1 shows schematically the main part of the experimental setup of the NICE-OHMS method. The three central components are the diode laser, electro-optic phase modulator (EOM, see section 5.1.2) and the resonator with iodine cell. A Toptica DL Pro 633 nm extended cavity diode laser (ECDL) is used as the laser system. For the resonator, a self-made device with an internal iodine cell is used (see section 5.1.1).

First, the optical components and the path of the light of the experimental setup are considered. The light with an optical output power of up to 35 mW (wavelength dependent) emitted by the DL Pro is divided into two parts by a combination of a half-wave plate ($\lambda/2$) and a polarizing beamsplitter (PBS). This combination of half-wave plate and PBS is used at various points of the setup to flexibly adjust the optical power for specific parts of the experiment. The reflected part is used for monitoring the laser spectrum and for measuring its frequency, whereas the transmitted part is used for the NICE-OHMS frequency stabilization. In both parts optical isolators are implemented,

because it turned out, that the frequency stabilization is extremely sensitive to back reflections to the laser diode. For monitoring the laser spectrum a scanning Fabry-Perot interferometer (FPI) and a photo diode (PD_1) (Thorlabs PDA10A) are used. To observe the frequency of the light with a beat measurement, a part of the light is passed to a He-Ne laser or to the frequency comb. For these purposes, only a few mW of power are needed.
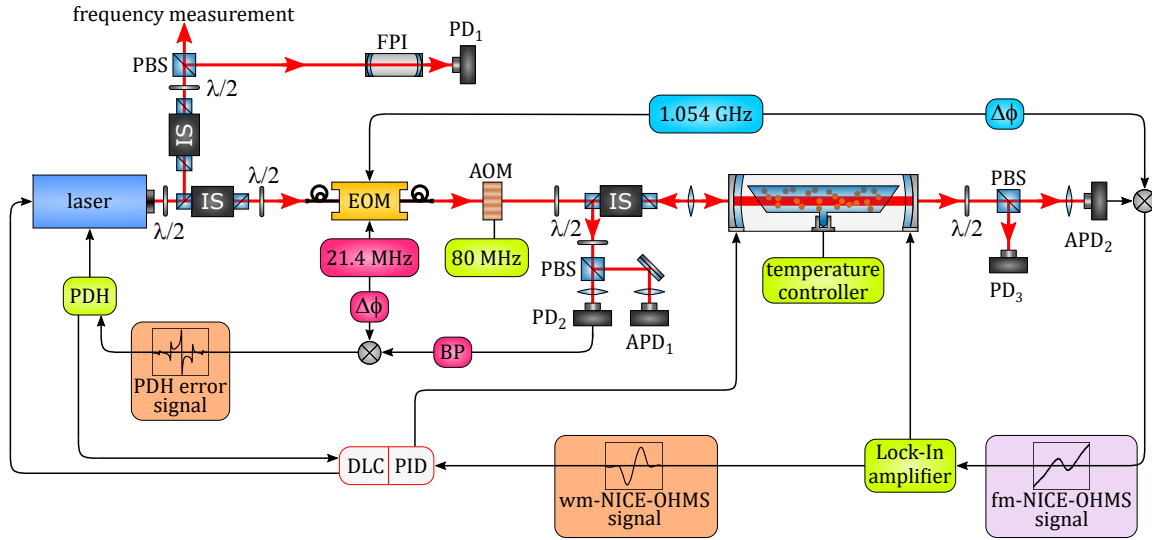

Figure 5.1: Sketch of the experimental setup for stabilizing a diode laser on sub-Doppler lines of iodine using the NICE-OHMS method. The optical path is shown in red, and the signal flow between the electronic components with black arrows. It contains isolators (IS), half-wave plates ($\lambda/2$), polarizing beam splitters (PBS), electro-optical modulator (EOM), acousto-optical modulator (AOM), electrical phase shifter ($\Delta\phi$), photodiodes (PD), avalanche photodiodes (APD), the Fabre-Perot interferometer (FPI), bandpass filters (BP), the Pound-Drever-Hall controller (PDH) and the laser controller (DLC) with integrated PID controller (PID).

The main part of the light with a power of about 20 mW is used for the NICE-OHMS frequency stabilization. With a Toptica Fiberdock this light is coupled into a polarization maintaining fiber of a wave-guide EOM to generate a phase modulation with the FSR (1.054 GHz) and the PDH (21.4 MHz) frequency. Since the beam shape of the DL Pro does not correspond to an optimal Gaussian beam, only about 75% of the light is coupled into the fiber. A half-wave plate is used to match the polarization to the preferred axis of the fiber. Via the EOM, the sidebands required for the PDH

and NICE-OHMS methods, are generated. Behind the EOM exit fiber the light is re-collimated to a Gaussian beam with a fiber coupler (S&K FC-4M5-10). The optical power losses in the fiber coupled EOM are about 6 dB, so that the combination of fiber coupling and EOM results in a total optical power loss of about 85%. With a previous power of 20 mW, this means that approx. 3 mW of optical power is available for frequency stabilization.

To further reduce the effects of back reflections from the cavity in to the laser, an acoustic optical modulator (AOM) is used in the free beam, and the first order diffracted beam is used. By the AOM the optical frequency is shifted by 80 MHz on the way to the cavity and again by 80 MHz when the reflected light passes the AOM a second time. This means that the light reflected from the cavity that returns to the laser has a frequency shift of 160 MHz and thus no significant perturbation of the laser frequency can occur. Behind the AOM the light passes a further combination of half-wave plate and isolator IS. Subsequently, the light is coupled into the resonator with a mode-matching lens combination. On the way from the EOM to the cavity, another 25% of optical power is lost, leaving about 2 mW of power available for coupling into the cavity.

The light reflected from the cavity is detected by a photo diode PD_2 (Hamamatsu Si:S5971) and an avalanche photo diode APD_1 (Hamamatsu S10341-02). With PD_2, the PDH error signal (see section 2.4) is detected at a frequency of 21.4 MHz and with APD_1 the an error signal is detected at a frequency of 1.032 GHz for the active tracking of the FSR (see section 5.3.4).

Behind the cavity, the transmitted light has an optical power of only a few $100\,\mu$W. With another APD_2 (Hamamatsu S10341-02) the NICE-OHMS error signal is detected at a frequency of 1.054 GHz, and the transmission of the cavity is measured with PD_3 (Thorlabs PDA10A). As an alternative to PD_3, a power meter (Thorlabs PM100D with S120C) is also used at this point for several measurements.

5.1.1 Cavity Design

The NICE-OHMS method requires a resonator containing a glass cell filled with iodine. For the design of the resonator, an iodine-stabilized helium-neon laser from PTB is used as a model. Figure 5.2 shows a CAD sketch and cross section alongside of the cavity used in this work.

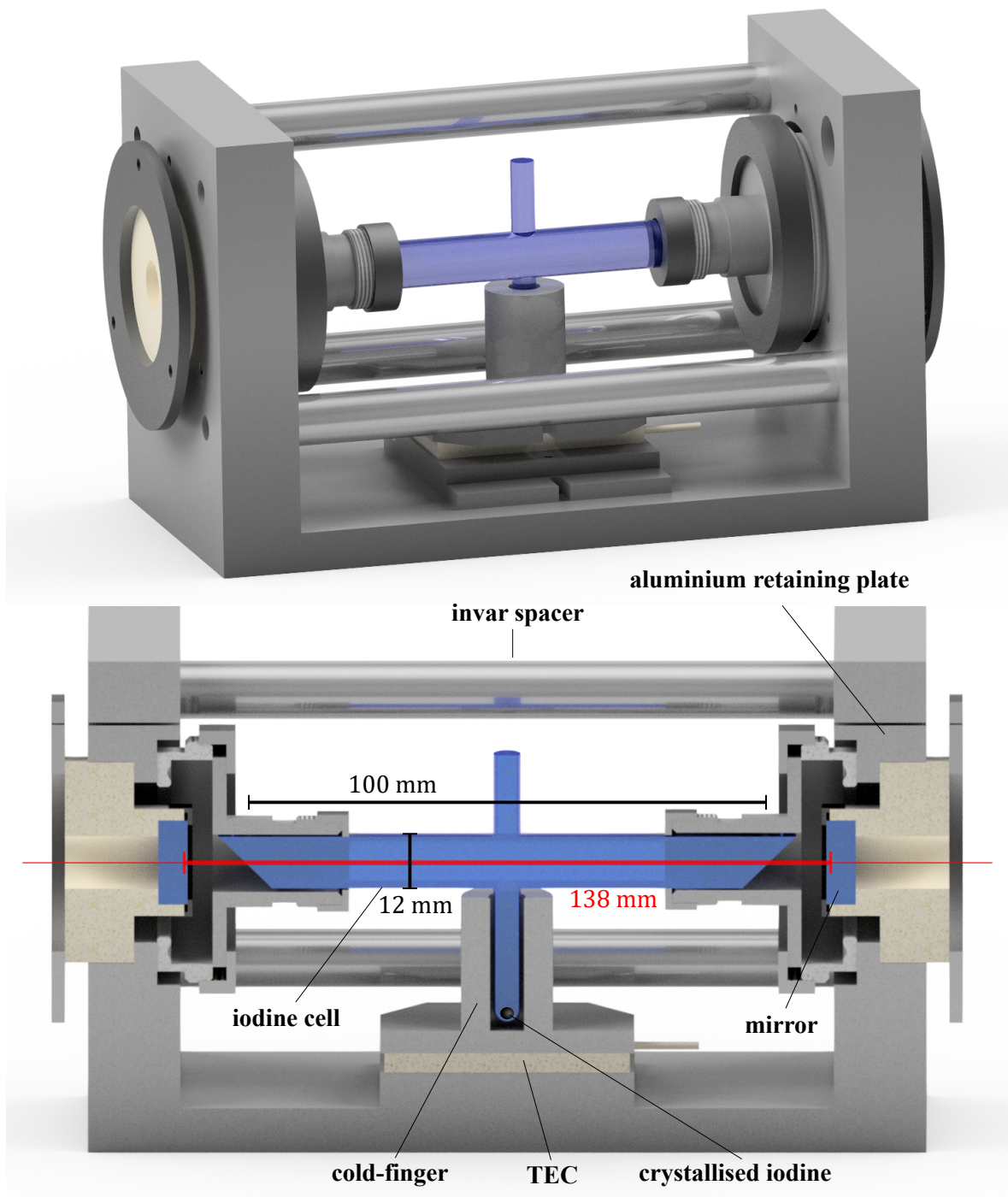The resonator consists of two mirrors mounted on piezo electric transducers to change

Figure 5.2: Rendered technical CAD images of the cavity with integrated iodine cell designed for NICE-OHMS spectroscopy. Top image shows the entire cavity, lower image shows a cross-section along the ray axis with labeling of the individual components. The length and diameter of the iodine cell (black) and the mirror spacing (red) are indicated.

the length by about $1\,\mu$m with a voltage of 1 kV. As shown in figure 5.2 and 5.3, the mirror Zerodur holders are mounted on the outside of the aluminum retaining plates by a clamping ring. This mirror mount design results in a robust and long-term stable cavity. Mirrors with a radius of curvature of $r_M = 1\,$m are used, which results in a stable eigenmode with a beam waist $w_0 = 227\,\mu$m at the center of the cavity and beam radii of $w = 260\,\mu$m at the mirrors. To avoid fluctuations in resonator length due to temperature effects, three Invar spacers are used between the two aluminum holders. The end of the Invar rods and the front surface of the Zerodur mirror holders are in the same plane of the aluminum endplate, thus thermal expansion of aluminum does not change the cavity length. The nickel-iron alloy Invar is used because of its low expansion coefficient of 0.98 ppm/K compared to other metals like aluminum (23.1 ppm/K) or steel (11.8 ppm/K) [24]. Thus, if the ambient temperature changes by 1 K, there is a change in the length of the resonator of about 140 nm due to the expansion of the Invar rods. This variation corresponds to a change in FSR of about 1 kHz. Since these changes are slow and the FSR changes only slightly compared to the set FSR in the GHz range, these effects can easily be corrected with a control and will be suppressed when the cavity is locked to iodine. Thereby the expansion should not have any influence on the frequency instability.

The reflectivities of the mirrors are chosen so that there is a good balance between the finesse of the cavity, the absorption of the medium, the build-up power to saturate the transitions and the optical power transmitted through the resonator, which is used for detecting the signals. Mirror M_1 as input coupling mirror has a measured transmission of $T_1 = (1.386 \pm 0.025)\,\%$ and the output coupling mirror M_2 a transmission of $T_2 = (0.352 \pm 0.006)\,\%$. This results in a finesse of $F = 355$ for the cavity without iodine cell (see equation (2.64)). A FSR of 1.087 GHz is measured by scanning over a full FSR of the cavity, which corresponds to a resonator length according to equation (2.61) of $L_C = 138\,$mm (without iodine cell) using the refractive index of air $n_{\mathrm{air}}(630\,\mathrm{nm}) = 1.00028$ [24].

Between the mirrors a gas cell with iodine $^{127}I_2$ is placed. The complete iodine cell holders are installed on the inside of the aluminum end plates with a mount (see figure 5.2).

Figure 5.3 shows this cell holder in detail. Using a screw cap, the iodine cell is clamped by O-rings into the cell holder. The holder itself is fixed to the mounting with another screw cap. Thereby it is possible to move the cell holder on the mounting cell holder for the adjustment. A Teflon disc glued onto the contact surface has proven
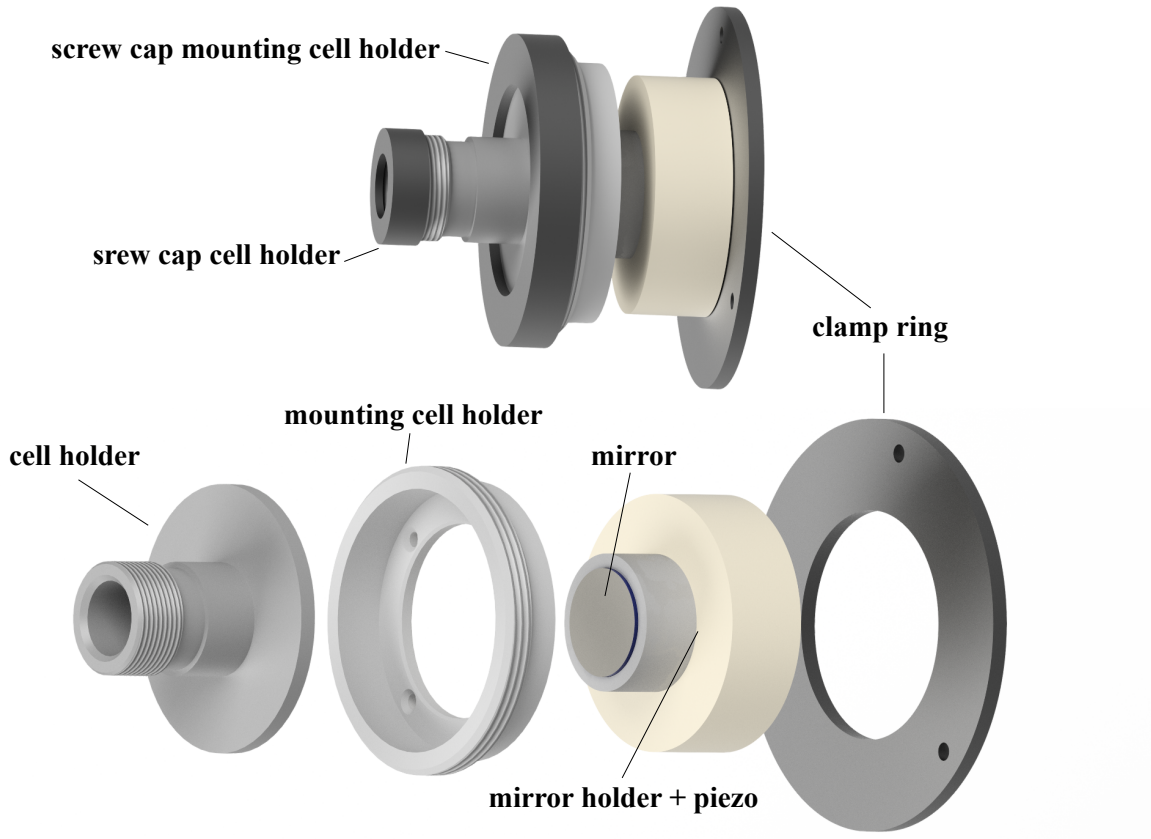
Figure 5.3: Rendered technical CAD drawings of the cell and mirror holder, without showing the aluminum retaining plate. Above, these are shown assembled with the locking caps. Whereas below the individual parts are shown for illustration. The individual parts are labeled in each case.

usefull for smooth and optimal adjustment of the cell position. This combination of the cell holder and the mount creates a gap in which the respective mirror is located. As a result, the beam path inside the resonator with the installed cell is in a closed system and therefore no dust can get onto the mirrors.

The iodine cell has a length of 100 mm on the beam axis and an outer diameter of 12 mm. At the ends of the cell there are two fused silica Brewster windows ([88], n=1.457 refractive index at 20 °C) at 55.53 ° for low optical losses. To set the vapor pressure of the iodine cell, the temperature of a cold-finger is controlled with a thermo-electric cooler (TEC). Thermal paste is used for a optimal temperature exchange. Solid iodine crystallizes at the coolest point of the cell inside the cold-finger. A temperature of 15 °C is set, which corresponds to a good compromise between signal strength of the Lamb-dips and optical intra cavity power. Also the results can be compared with

the standard frequency values of the BIPM [13] that assume the same cold finger temperature. With the cell installed, the longer optical path through the iodine cell results in a FSR of 1.054 GHz.

Figure 5.4 shows a photo of the cavity with integrated iodine cell set up in the experiment. The light path can be seen in the center of the cell due to the luminescence of the iodine resonating with the light. The top of the TEC cooler is surrounded by insulation material to keep the temperature stable.
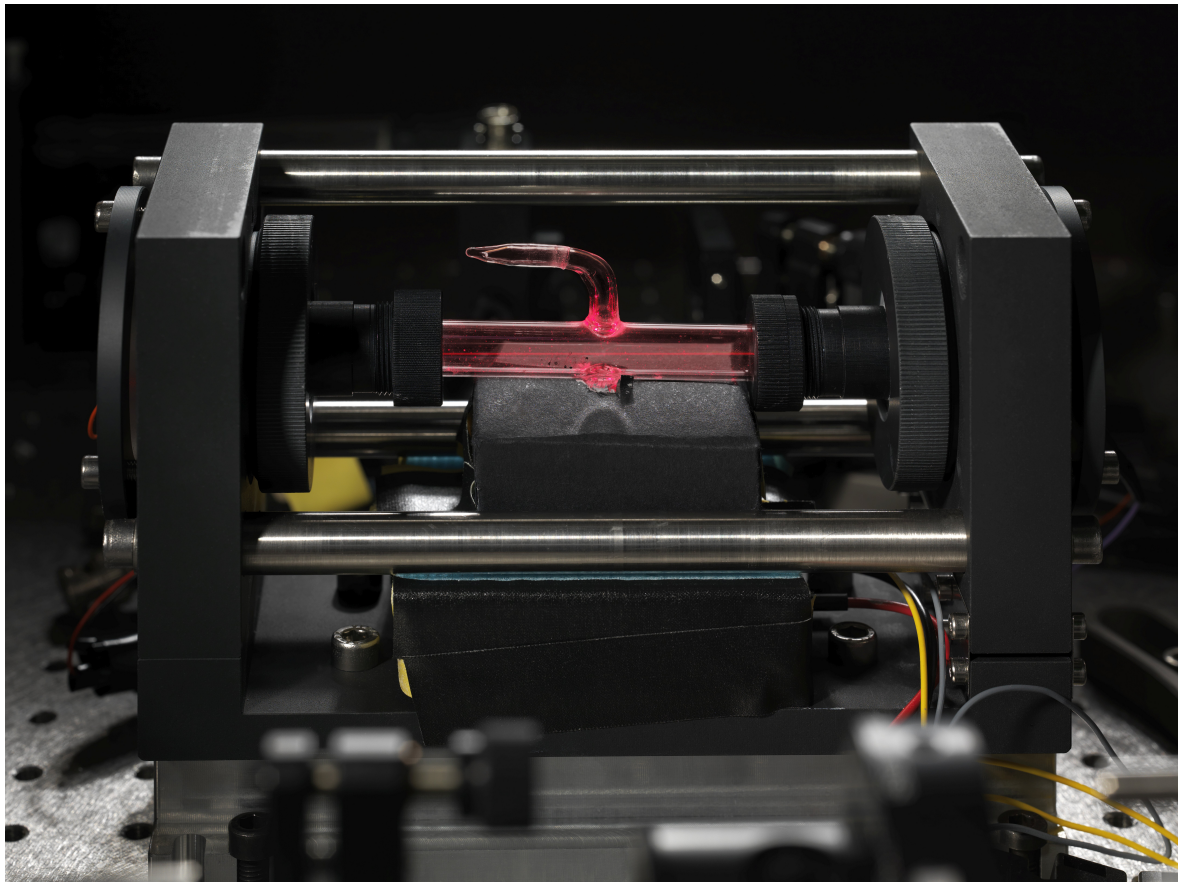
Figure 5.4: Photo of the cavity used in the experiment with the iodine cell installed. The laser is stabilized with the NICE-OHMS method, so that the iodine gas can be seen inside the cell in the beam path through the luminescence.

5.1.2 Electro-Optic Phase Modulator (EOM)

To generate the phase modulation of the light required for the PDH and NICE-OHMS method, an electro-optic phase modulator is used. The functionality of EOMs is based

on the linear elctro-optical effect called the Pockels effect. By applying a voltage to a non centrosymmetric crystal, the refractive index is changed proportional to the applied electric field [89]. In this work, two different fiber coupled waveguide EOMs are used. The first one from the company AdvR is based on the birefringent material potassium titanyl phosphate (KTP) [90]. The second one from the company Jenoptik is based on a proton exchanged lithium niobate (LiNbO$_3$) waveguide. In general, the choice of waveguide EOMs for the wavelength of 633 nm was very limited. The KTP based EOM was the first choice, since it would have been possible to regulate away a possible occurring RAM by means of an applied DC voltage due to the two transmissive polarization directions [91, 92]. However, over time it became apparent that the KTP based EOM had a defect (see section 5.3.1). For this reason, the LiNbO$_3$ based EOM from Jenoptik was used as a replacement. Since this EOM uses a proton exchange waveguide, only one polarization direction is transmitted by the waveguide and a control of RAM by means of a DC voltage is not possible.

To generate the sidebands for both the PDH and the NICE-OHMS method, the rf-frequency signals generated with two synthesizers are combined using a rf power splitter, amplified and applied to the EOM input.

Two different methods are used to examine and adjust the sidebands generated by the EOM. For the PDH sidebands, the transmission of the cavity is used, which in this case acts as a Fabry-Perot spectrometer. The NICE-OHMS sidebands are determined with a beat frequency measurement.

To determine the PDH sidebands, the resonator length is kept stable and the frequency of the laser is tuned into a range of several 100 MHz by changing the laser PZT voltage. The transmission of the cavity is measured with the photodiode PD$_3$ and shown normalized between 0 and 1 in figure 5.5. We adjust the amplitude of the PDH modulation signal applied to the EOM so that the ratio between carrier and sideband corresponds to approximately 0.42 (here: 0.413). As described in section 2.4, this ratio corresponds to an optimal PDH error signal.

Since the FSR of the resonator is equal to the modulation frequency of the NICE-OHMS sidebands, these sidebands cannot be measured as before. Therefore, a beat frequency measurement as presented in section 3.1 is performed here. For this purpose, the light beam behind the EOM is guided out of the setup with a folding mirror. This beam is superimposed with light of the He-Ne as shown in figure 3.1 and the beat frequency of both light fields is investigated. Because the frequency modulation of the He-Ne is interfering with this investigation, it is turned off so that the frequency
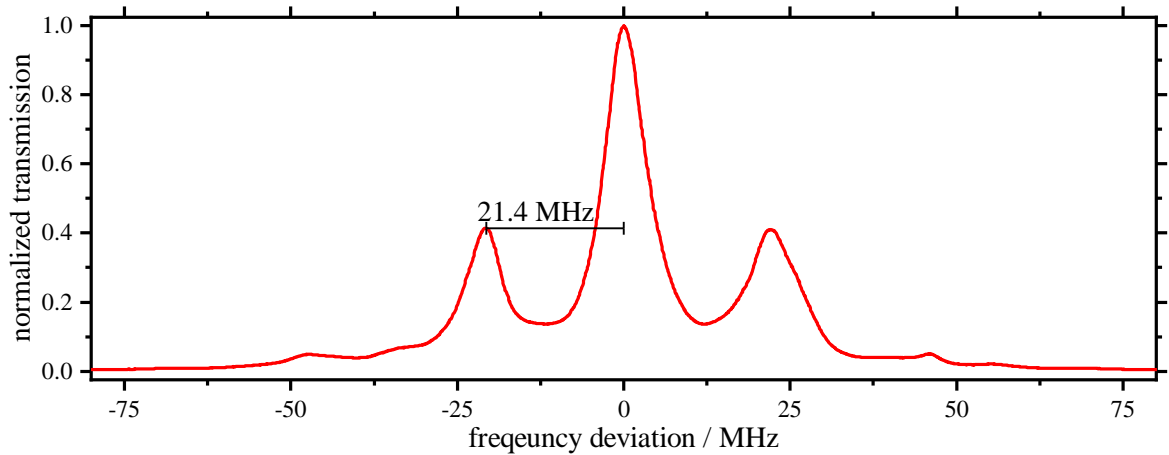
Figure 5.5: Frequency spectrum of the laser light behind the EOM measured with the cavity. The generated sidebands have a distance of 21.4 MHz to the carrier.

of the laser is not stabilized to an iodine line. However, this has no great influence, since this measurement is only used to adjust the sideband ratios. With an APD, the beat is detected and viewed with a spectrum analyzer. Figure 5.6 shows the measured frequency spectrum.
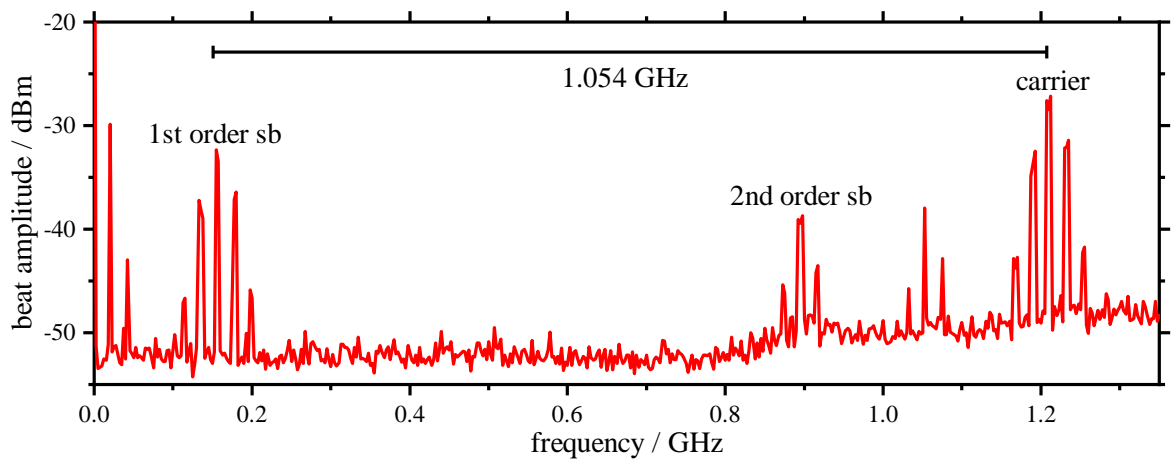
Figure 5.6: Example of beat frequency spectrum between the phase modulated light field of the laser behind the EOM and a He-Ne laser. The carrier and the first and second sideband of the 1.054 GHz modulation are marked.

The frequency of the light from the DL Pro is set to a value, that both the carrier and the first sideband of the NICE-OHMS modulation are on the same side offset from the frequency of the light from the He-Ne laser. As a result, the carrier in Figure 5.6 is at a frequency greater than 1.2 GHz and the first sideband is at a frequency less

than 0.2 GHz. The spacing of these two components is at the applied rf frequency f_{NO} of 1.054 GHz. A measurement of the power of the sidebands compared to the carrier gives a modulation index of $\beta = 0.8$. To exclude the frequency response of the photodiode, for this measurement the laser was tuned, such that the carrier and the sidebands appear at similar beat frequencies. At a frequency of about 0.9 GHz the second order sideband can be seen, which is on the other side of the frequency of the light of the He-Ne laser. Both the carrier and the first and second order sidebands show the sidebands of the PDH modulation, each with a spacing of $f_{PDH} = 21.4\,\text{MHz}$. In this case, the modulation index is $\beta = 1.09$. In the spectrum, however, further peaks can be seen at a frequency around 0 GHz and around 1.054 GHz. The peaks around 0 GHz have a frequency of 21.4 MHz or a multiple of it and appear in the spectrum due to residual amplitude modulation in the EOM at the PDH frequency. Similarly, the peaks at 1.054 GHz are generated by RAM from the NICE-OHMS frequency and the mixed product of NICE-OHMS and PDH frequency.

5.1.3 PDH-Lock

How is the PDH error signal generated to stabilize the laser frequency to the length of the cavity? With a QDDS (AD9959) the PDH frequency of $f_{PDH} = 21.4\,\text{MHz}$ is generated. A QDDS consist of four direct digital frequency synthesizer on a chip with common clock, which produce four outputs with well defined phase relations. The QDDS itself is referenced to a stable 100 MHz PTB reference. For the excitation of the PDH sidebands, the PDH frequency signal is applied to the EOM. The signal is filtered with a 50 MHz high pass and a 21.4 MHz band pass to remove interfering higher harmonic signals. The signal from photo diode PD_2, which is generated by the reflection of the cavity, is amplified and bandpass filtered (21.4 MHz). Then it is mixed with a reference frequency signal ($f_{PDH}^{ref} = 21.4\,\text{MHz}$) of the QDDS and the PDH error signal is obtained. Using the QDDS, the phase relationship $\Delta\phi_{PDH}$ between the signal applied to the EOM and the reference signal is also adjusted. To determine the correct phase shift $\Delta\phi_{PDH}$ between the two signals, the laser frequency ν_{DL} is modulated in a range of 100 MHz around the resonance of the cavity. The phase is changed until the main resonance peak in the PDH error signal disappears. Then the phase $\Delta\phi_{PDH}$ is adjusted by $\pm 90\,^\circ$ so that the slope in the zero crossing at resonance becomes maximum (see figure 5.7).
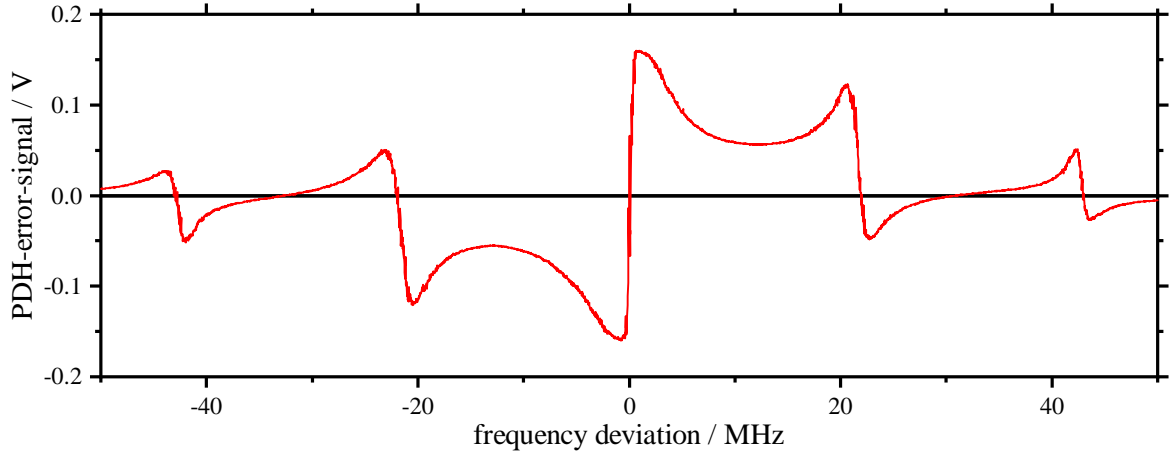
Figure 5.7: Measured optimized Pound-Drever-Hall error signal in terms of mixer output voltage versus frequency deviation from cavity resonance.

Figure 5.7 shows an example of a PDH error signal measured with PD_2 after the mixer. Compared to the simulated signal in Fig. 2.14, the signal from the experiment shows a zero crossing even at a frequency of 41.8 MHz, which corresponds to a higher sidebands order (>1) that were not included in the simulation.

To stabilize the laser frequency to the resonance frequency of the cavity with the help of the PDH error signal, a PTB self-made PDH servo amplifier is used. This proportional, integral, differential (PID) servo amplifier ensures that the error signal remains at zero. The PDH servo has two outputs to control the laser. The fast one is directly connected to the input of the current at the laser diode itself and is used to correct fast frequency changes, such as vibrations, in a short time. The second slow output takes the fast output into a second unlimited proportional-integral (PI) amplifier to control the voltage at the laser tuning piezo via the DLC to correct for influences over longer periods of time, such as temperature changes and thus to keep the fast output on average at zero.

5.1.4 Intra Cavity Absorption Spectroscopy

In this section the behavior of the cavity with a built-in iodine absorption cell will be investigated. Based on these investigations, the absorption coefficient α will be estimated from optical power measurements. The cavity is assumed to be in resonance ($\Delta\nu = 0$) with the incoupled mode matched single frequency light field. Accordingly,

the ratio of the incident optical power P_{in} to the reflected power P_{ref} or to the power transmitted P_{out} by the cavity is given by [52]:

$$\frac{P_{\text{ref}}}{P_{\text{in}}} = \left(\frac{T_1 + 2A_{\text{all}} - T_2}{T_1 + 2A_{\text{all}} + T_2}\right)^2 \qquad \text{and} \qquad \frac{P_{\text{out}}}{P_{\text{in}}} = \frac{4T_1T_2(1 - 2A_{\text{all}})}{(T_1 + 2A_{\text{all}} + T_2)^2}. \tag{5.1}$$

In comparison to chapter 2.3.2 it has to be considered that the power is measured and therefore the coefficients of the mirrors refer to the measured power ($R = |r|^2$, $T = |t|^2$, see section 2.3). A_{all} describes the power absorption coefficient within a half roundtrip through the cavity and includes the absorption and scatter of the mirrors A_{m}, the cell windows and the iodine:

$$1 - A_{\text{all}} = \sqrt{(1 - A_{\text{m,1}})(1 - A_{\text{m,2}})(1 - A_{\text{cell}})} \cdot e^{-\alpha L_{\text{cell}}} \tag{5.2}$$

Since in the experiment the laser is stabilized to the resonance of the cavity by the PDH method, the distribution of the power between the triplet of carrier and sidebands must be taken into account when measuring the input power. Ideally, only the carrier should be coupled into the cavity, but measurements of the frequency spectrum behind the cavity have shown that because of the finite cavity linewidth a small faction η of the sideband power is also coupled into the cavity. With a mode matching coefficient ϵ the following power ratio between the input power P_{in} and the transmitted power P_{out} results:

$$\frac{P_{\text{out}}}{P_{\text{in}}} = \epsilon \left(J_0^2 + 2\eta J_1^2\right) \frac{4T_1T_2(1 - 2A_{\text{all}})}{(T_1 + 2A_{\text{all}} + T_2)^2}. \tag{5.3}$$

Here $\epsilon \left(J_0^2 + 2\eta J_1^2\right)$ describes the fraction of the total input power that is coupled into the cavity. For the reflected part, the following applies:

$$\frac{P_{\text{ref}}}{P_{\text{in}}} = 1 - \epsilon \left(J_0^2 + 2\eta J_1^2\right) \left[1 - \left(\frac{T_1 + 2A_{\text{all}} - T_2}{T_1 + 2A_{\text{all}} + T_2}\right)^2\right]. \tag{5.4}$$

Here, with the small modulation index used in the experiment it was assumed that $J_0^2 + 2J_1^2 \approx 1$. If equation (5.3) is now substituted into equation (5.4) with elimination of $\epsilon \left(J_0^2 + 2\eta J_1^2\right)$, the total single path absorption A_{all} of the cavity with built-in iodine cell can be determined from the power in front of and behind the cavity and the transmission T_2 of the output coupling mirror:

$$A_{\text{all}} = \frac{-T_2}{2} \frac{P_{\text{in}} - P_{\text{ref}} - P_{\text{out}}}{T_2 \left(P_{\text{in}} + P_{\text{ref}}\right) - P_{\text{out}}} \tag{5.5}$$

Now, how can the iodine absorption coefficient α be determined from the total experimentally received absorption A_{all}? For this purpose, three cases are considered and power measurements are performed in each case:

1. without an iodine cell: $(1 - A_{\text{all}})^2 = (1 - A_{\text{m,1}})(1 - A_{\text{m,2}})$,

2. with an empty cell: $1 - A_{\text{all}} = \sqrt{(1 - A_{\text{m,1}})(1 - A_{\text{m,2}})}(1 - A_{\text{cell}})$,

3. with an iodine cell: $1 - A_{\text{all}} = \sqrt{(1 - A_{\text{m,1}})(1 - A_{\text{m,2}})}(1 - A_{\text{cell}})e^{-\alpha l_{\text{cell}}}$.

Case one can be easily implemented experimentally by removing the cell. Based on equation (5.5), a total absorption of $A_{\text{m}} = A_{\text{m,1}} + A_{\text{m,2}} = 0.00023$ is determined for both mirrors. The absorption of the mirrors is very low and can be neglected. Using this absorption and the measured transmission, equation (2.60) gives a reflectivity of $R_1 = 0.9860$ for the input mirror and a reflectivity of $R_2 = 0.9964$ for the output mirror. These values are slightly higher than the values given by the manufacturer ($R_1 = 0.985$ and $R_1 = 0.995$), but still within the specified tolerances. The coupling constant $\epsilon = 0.92$ is derived from equation (5.3) by assuming that the sidebands are completely reflected due to the high finesse of the empty cavity of $F = 360$ (compare equation (2.64)) and thus $\eta \approx 0$.

Since no empty gas cell was available, case 2 is implemented as follows. It is assumed that at a frequency far from an absorption line and with low vapor pressure, the absorption is zero and thus corresponds to an empty gas cell. For this reason, in order to determine the losses of the cell windows, the frequency of the laser is set so that it has an offset of +600 MHz from the HF line R(127)11-5 "f". This corresponds to an offset to the transmission minimum of the line P(33)6-3 of about 1.5 GHz and thus almost twice as far as the FWHM of the Doppler broadened line.

Based on case three, the absorption maximum of the line P(33)6-3 was determined, by adjusting the laser frequency to the transmission minimum.

In a series of measurements, different cold finger temperatures T between 5 °C and 20 °C are set to investigate the dependence of the absorption A_{all} on the vapor pressure $p(T)$ inside the cell. In a first set of measurements the optical intensity irradiated onto the resonator is kept constant at approx. $P_{\text{in}} = 6.9\,\text{mW}$. The transmitted power P_{out} and the reflected power P_{ref} are measured in parallel. The reflected power is determined with the photodiode PD_2. Its voltage proportional to the light power is measured in two conditions. Outside the resonance of the cavity the maximum voltage is measured U_{max} and in resonance the minimum voltage U_{min}. By multiplying the ratio $U_{\text{min}}/U_{\text{max}}$ by the power emitted on the cavity P_{in}, the power reflected by the cavity P_{ref} is obtained.

Figure 5.8 shows the single path absoprtion A_{all} determined from equation (5.5) as function of the vapor pressure in the cell.
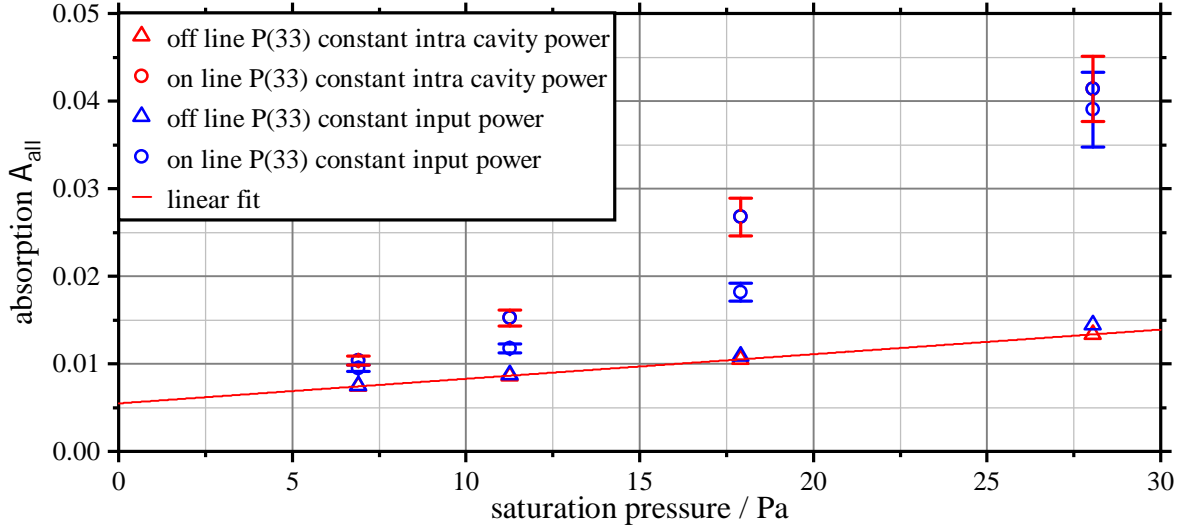
Figure 5.8: Single path absorption A_{all} with iodine cell determined from cavity transmission and reflection at the center of the Doppler broadened iodine line P(33)6-3 (circles) and with 1.5 GHz detuned (triangles). The power inside the cavity was kept constant (red) or the power before the cavity (blue) was fixed.

The calculated absorption A_{all} at the center of the P(33)6-3 line does not increase linearly with the vapor pressure $p(T)$ as naively expected. Although always the same power is irradiated, the optical power within the cavity P_{cav} varies strongly due to the variation of the absorption by the vapor pressure. At 5 °C the power on the line center is at $P_{\text{cav}} = 170\,\text{mW}$, whereas at 20 °C the power is at $P_{\text{cav}} = 39\,\text{mW}$. With an average beam waist of $\omega_0 = 0.237\,\text{mm}$, intensities vary from $I_{\text{cav}} = 22\,\text{W/cm}^2$ to $I_{\text{cav}} = 96\,\text{W/cm}^2$ inside of the cavity. If the intensities are compared with the saturation intensity $I_{\text{sat}} = 10.3\,\frac{\text{W}}{\text{cm}^2}$ from section 2.2.2, it is clear that for smaller vapor pressures the intensity is greater than the saturation intensity. Thus, the observed non-linearity can be explained by the saturation of the transition depending on the vapor pressures (see equation (2.28)).

Thus another series of measurements is performed for cases on and off resonance of line P(33)6-3. This time the power $P_{\text{out}} = 70\,\mu\text{W}$ transmitted through the cavity is held constant. This guarantees that within the cavity the power ($P_{\text{cav}} = 20\,\text{mW}$) and therefore the intensity $I_{\text{cav}} = 11\,\text{W/cm}^2$ is nearly constant. The absorption A_{all} determined from this series of measurements is plotted in red in Figure 5.8.

In the case of constant intracavity power due to the reduced intensity, the absorp-

tion is bigger than in the case of constant irradiated power. There is also a rather linear relationship between absorption and vapor pressure. The measured absorption away from the iodine line P(33)6-3 (case two) also increases continuously with the vapor pressure ($\alpha_{\mathrm{back}} = 0.0085\,\mathrm{m^{-1}Pa^{-1}}$). This indicates a weak residual absorption background of the gas in addition to the absorption and scattering of the cell windows which is independent of the vapor pressure. There is only a minimal difference in the absorption for different intensities in the cavity, so the background iodine absorption shows no sign of saturation. The contribution of background absorption was explained by transitions from ground level X to the first dissociating electronic A states with $\alpha_{\mathrm{back,Bri}} = 0.0038\,\mathrm{m^{-1}Pa^{-1}}$ [43] (see figure 2.1). By a linear fit through the measured values next to the P(33)6-3 line, the absorption of the empty cell A_{cell} is determined at the y-axis intercept by subtracting the absorption of the mirrors A_{m} from this absorption value. The absorption and scatter loss of the empty cell is therefore $A_{\mathrm{cell}} = 0.0053$.

With an empty cell, the finesse drops to $F = 218$ and on line P(33)6-3 further to $F = 86$ at a cooling finger temperature of 15 °C and a constant internal power of 20 mW. For all measured absorptions from figure 5.8, the background absorption and the absorption of the cell determined from the linear fit are subtracted, resulting in the respective absorption of the iodine line P(33)6-3. Using these absorptions, the coefficients at negligible saturation $\alpha^0_{\mathrm{P(33)6-3}}$ are determined and an averaged absorption coefficient of $\bar{\alpha}^0_{\mathrm{P(33)6-3}} = (0.0116 \pm 0.0027)\,\frac{1}{\mathrm{m \cdot Pa}}$ is obtained.

With a further experiment, it was examined how well the simulated results from the parameters determined up to here agree with the observation in a NICE-OHMS setup. There, in addition to the carrier, two side-bands are generated, which have a frequency spacing in the order of the FSR of the cavity. The frequency of the laser is stabilized to the resonance of the cavity by the PDH method. Because of the PDH stabilization the whole frequency range of some GHz of the line P(33)6-3 cannot be sampled, but only a range of several 100 MHz around the absorption peak. Thus the transmission is normalized as follows: First the transmission outside the resonance with the medium is determined, to obtain the maximum transmitted power. Then the transmitted power is determined at the frequency at which the iodine absorbs maximally, so that an order of magnitude for the absorption of the Doppler broadened spectrum can be given. At last the transmission spectrum of iodine near the maximum absorption is detected. Beside the Doppler broadened line, a total transmitted power of $P_0 = 0.264\,\mathrm{mW}$ is determined at a laser frequency of $\nu = \nu_0^{\mathrm{P(33),j}} + 1490\,\mathrm{MHz}$. On the line at $\nu = \nu_0^{\mathrm{P(33),j}}$ the total transmitted power is $P_{\mathrm{P(33),j}} = 0.187\,\mathrm{mW}$. Now the splitting of the power

into carrier and sidebands is considered. With a modulation index of $\beta = 1.08$, this results in a power of 56% in the carrier and 21% in the respective sidebands. Since the modulation frequency is $f_{\text{FSR}} = 1053\,\text{MHz}$, the sidebands should not contribute to the absorption, so that they provide a constant offset in the transmitted power. As a result, the absorption of the medium reduces the transmitted power from 0.148 mW (100%) to 76 mW (51%). Figure 5.9 shows the recorded normalized transmission spectrum of line P(33)6-3 in the range of lines 'h' to 'k'. The normalized amplitude of the Lamb-dips of line "j" is 0.003 (black bar).
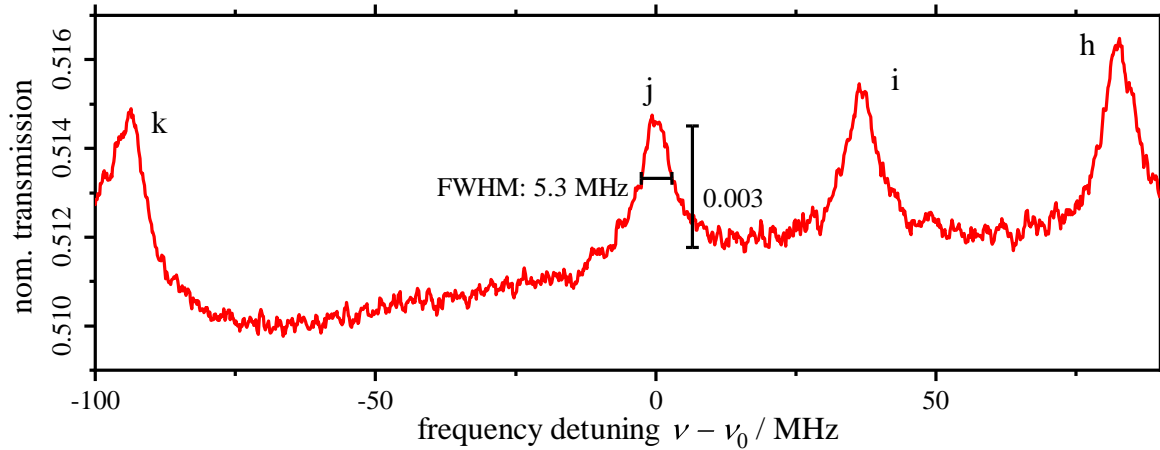

Figure 5.9: Measured normalized saturation transmission spectrum of the cavity from the iodine line P(33)6-3. The irradiated spectrum of the light is frequency modulated with sidebands at the distance of the FSR of the cavity.

Next, the transmission of the cavity is simulated when the laser frequency is phase modulated with the frequency close to the FSR. Since the carrier frequency in the experiment is stabilized to the resonance of the cavity by means of the PDH method, this is also assumed for the simulation. In addition, it is taken into account that the actual FSR of the cavity changes depending on the dispersion of the medium, so that the sidebands are not always in resonance with the neighboring modes of the cavity resonance. Figure 5.10 shows the simulated individual transmission of the cavity for the three frequency components. Here black indicates the carrier, blue the upper sideband ($\nu + f_{\text{mod}}$) and red the lower sideband ($\nu - f_{\text{mod}}$). Up to this point it is assumed that modulation frequency $f_{\text{mod}} = 1054.4\,\text{MHz}$ corresponds to the FSR at the iodine line center.

As the carrier is always in resonance with the cavity, its transmission (black) at the line P(33)6-3 has the same shape as in the experiment with the long iodine cell (see
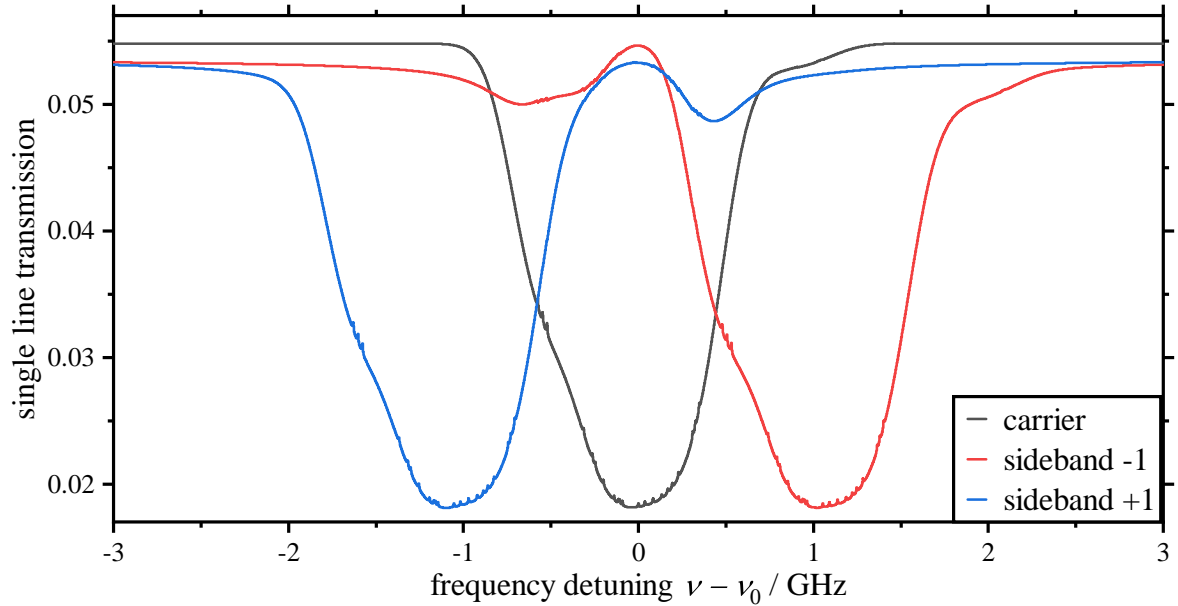
Figure 5.10: Simulated individual transmission coefficients of the cavity with built-in iodine cell in the frequency range of the iodine line P(33)6-3 of the carrier (black) and the two sidebands (red, blue) of the radiated frequency modulated spectrum

figure 2.5). The transmission of the sidebands (red, blue), however, shows a distortion of the spectrum. This effect on the sidebands can be explained by the influence of dispersion on the FSR (see eq. (2.62)). Depending on the irradiated laser frequency, the FSR varies due to the dispersion of the medium and thus the frequency spacing $|\nu_{k\pm1} - \nu_k|$ of the modes of the cavity by a view MHz. Since the sidebands of the irradiated light are always at the same frequency spacing, they are sometimes more and sometimes less resonant with the ±1 cavity mode. As a result, the transmission of the sidebands through the cavity changes which explains the strong distortion behavior of the sideband transmission in the range of the medium, although the sidebands themselves do not interact with the medium.

At the edge of the spectrum, where no absorption takes place, the transmission of the sidebands is lower than that of the carrier. If the modulation frequency of the sidebands is set to the FSR at the frequency of maximum absorption like in the simulation, the consequence is that outside the range of the medium the FSR is different and the sidebands are not optimally resonant with the ±1 cavity mode. This leads to the lower transmission of the sidebands at the edge of the figure.

In addition, in the frequency range of the highest absorption, it can be seen that the

transmission of the sidebands is at a maximum and reaches the value of the carrier, because the cavity FSR fits to the spacing of the sidebands. In this range, there is also a dispersive behavior, which deviates from the shape of the transmission spectrum of the carrier.

Figure 5.11 shows the resulting total simulated normalized transmission spectrum of the sum of all three sidebands (modulation index $\beta = 1.08$) with their correct power ratio. Compared to the simple saturation spectroscopy on the long cell, it can be seen that the spectrum is strongly broadened and strongly deformed in the region of the absorption of the medium. To compare the experimental data with the simulation, the modulation frequency is set to $f_{\mathrm{mod}} = 1053\,\mathrm{MHz}$ and is also shown in red in figure 5.11. In addition, another simulated transmission with a modulation frequency of $f_{\mathrm{mod}} = 1051\,\mathrm{MHz}$ is shown in black.
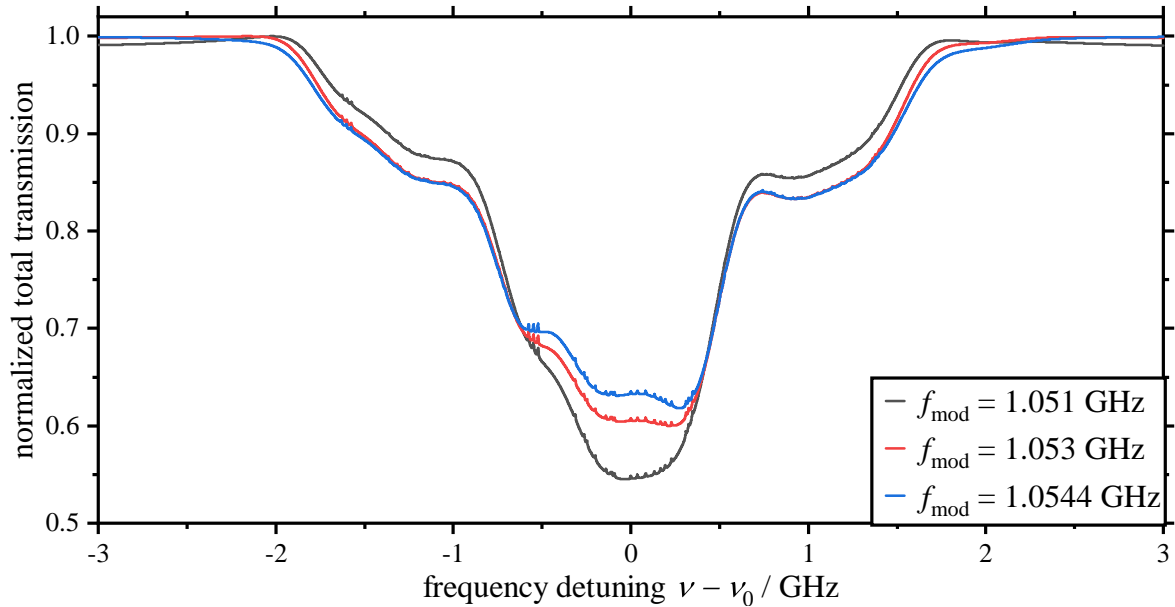

Figure 5.11: Simulated total normalized transmission of the iodine line P(33)6-3 through the cavity over the frequency deviation $\nu - \nu_0$ for the modulated input field for three different modulation frequencies f_{mod}.

It can be seen that the shape of the transmission changes with the selected modulation frequency, and the further it is from the FSR with maximum absorption, the spectrum in the medium region approaches the shape of the simple saturation spectroscopy. At the modulation frequency of $f_{\mathrm{mod}} = 1053\,\mathrm{MHz}$, the simulated data show a loss of transmission due to absorption of about 40 % and the dip depth of the Lamb-dips is 0.24 %. Compared to the experimental data, these are in good agreement. A

fit to the data is very complex and not possible, because too many variables have to be taken into account, which are difficult to determine experimentally and fluctuate. The change of the transmission due to the change of the modulation frequency could also be observed in the experiment in the way described by the simulations.

Based on the data obtained up to this point from the various experiments, the following parameters are used to simulate the NICE-OHMS signals for the further investigations of this thesis

- $S = 1.18$ saturation parameter

- $\alpha_{\text{sca}}^0 = 797$ scaling factor of the absorption given by the "Iodine Spectrum" program to get α in $1/m$

- $\alpha_{\text{IS}} = 0.18 \cdot 10^{-4}$ - $0.25 \cdot 10^{-4}$ from "Iodine Spectrum" calculated line intensity of the HFS components of line P(33)6-3

- $T = 293\,\text{K}$ cell wall temperature

- $p = 17.9\,\text{Pa}$ pressure in the cell ($T_{\text{cf}} = 288.15\,\text{K}$ cold-finger temperature)

- $\gamma_{\text{n}} = 513.4\,\text{kHz}$ natural line width [42]

- $\gamma_{\text{col}} = 3.5\,\text{MHz}$ collision broadening and $\Delta_{\text{pow}} = 1.48$ power broadening factor based on $S = 1.18$ and equation (2.33)

- $K(T) = 1.2 \cdot \sqrt{\frac{293\text{K}}{T}}\,\frac{\text{MHz}}{\text{Pa}}$ K-factor based on equation (2.33) and $p = 17.9\,\text{Pa}$

- $I_{\text{sat}} = 10.3\,\frac{\text{W}}{\text{cm}^2}$ saturation intensity

- $d = 1.5 \cdot 10^{-31}\,\text{Cm}$ dipole moment based on I_{sat}, $K(T)$ and equation (2.34)

- $\gamma_{\text{dip}} = 5.9\,\text{MHz}$ resulting Lamp-Dip line width (5.3 MHz width is observed in the experimental cavity transmission)

- $f_{\text{mod}} = 1054.4\,\text{MHz}$

- $\beta = 1.08$ modulation index

- $L_{\text{cell}} = 10\,\text{cm}$ length of the iodine cell

- $R_1 = 0.986025$ and $R_2 = 0.996365$ power reflectivity of the mirrors

- $T_1 = 0.01386$ and $T_2 = 0.00352$ power transmission coefficient of the mirrors

- $L_{\text{rest}} = 0.0105$ single pass loss of empty cell and background absorption of iodine at cold-finger temperatur of 15 °C

5.1.5 Frequency Modulated NICE-OHMS

In order to stabilize the frequency of the laser on the molecular transition of iodine, the NICE-OHMS method is now used to generate a low-noise frequency sensitive error signal. In a first step, a NICE-OHMS signal is generated based on frequency modulating the laser with a frequency f_{NO} equal to the FSR. In the experimental setup (figure 5.1), the laser light is phase modulated and the transmitted light from the cavity is detected with the avalanche photo detector APD$_2$. To evaluate the photo diode signal at the frequency of f_{NO}, it is mixed with a reference signal at the same frequency. The phase shift $\Delta\phi_{\text{NO}}$ between the reference signal and the voltage applied to the EOM is adjusted to maximize the slope of the Doppler broadened signal and thus also maximize the slope between local minimum and maximum around the Doppler free Lamb-dips of hyperfine components of the iodine line. Figure 5.12 shows a measured NICE-OHMS error signal (red) of the line P(33)6-3 and the corresponding cavity transmission (black). Here, the cavity length was tuned over a frequency range of several 100 MHz with the piezo at one mirror of the cavity.
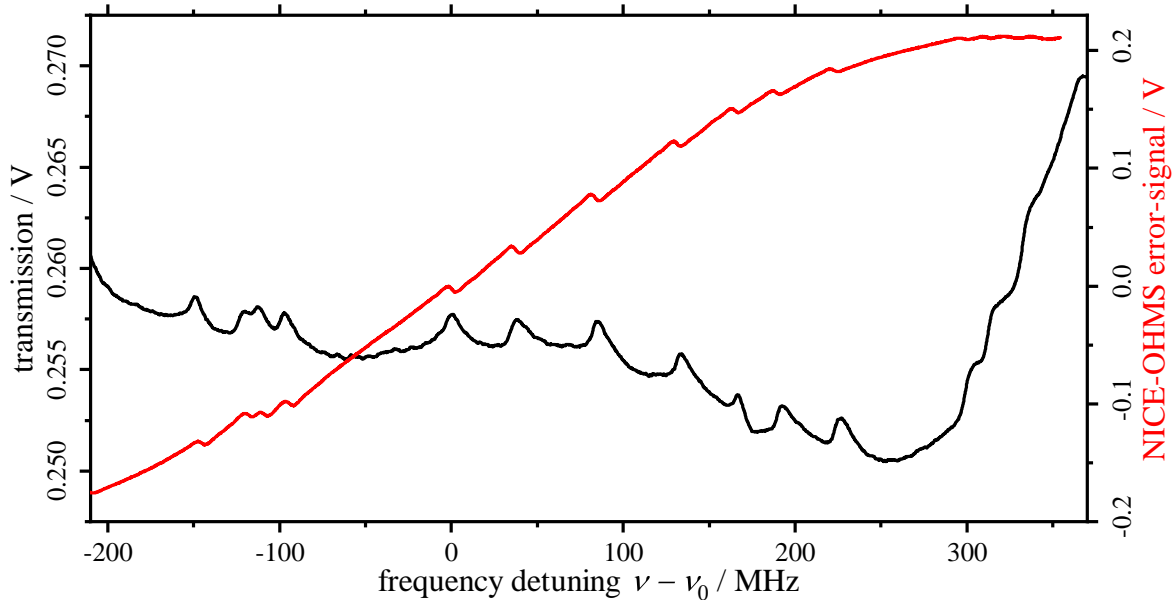

Figure 5.12: Measured NICE-OHMS error signal (red) of the iodine line P(33) 6-3 and the transmission of the cavity (black) versus the frequency deviation. Zero detuning indicate the position of the HFS component "j".

The transmission shows the Lamb-dips of the HFS transitions "d-n" and the distortion of the Doppler broadened signal is also noticeable, which indicates that that the modulation frequency f_{NO} is close to the FSR at the center of the Doppler broadened line (see figure 5.11). In the error signal, the HFS transitions appear as the local minima and maxima on top of the slope from the Doppler broadened background. Compared to the simulation (see fig. 2.18), in the NICE-OHMS error signal the slope of the Doppler broadened background flattens out much earlier with the detuning. This can be explained by saturation effects in the electronics used to generate the error signal. Since in this work mainly the line "j" is considered, which is located near the zero point of the Doppler broadened NICE-OHMS error signal, this effect is not relevant.
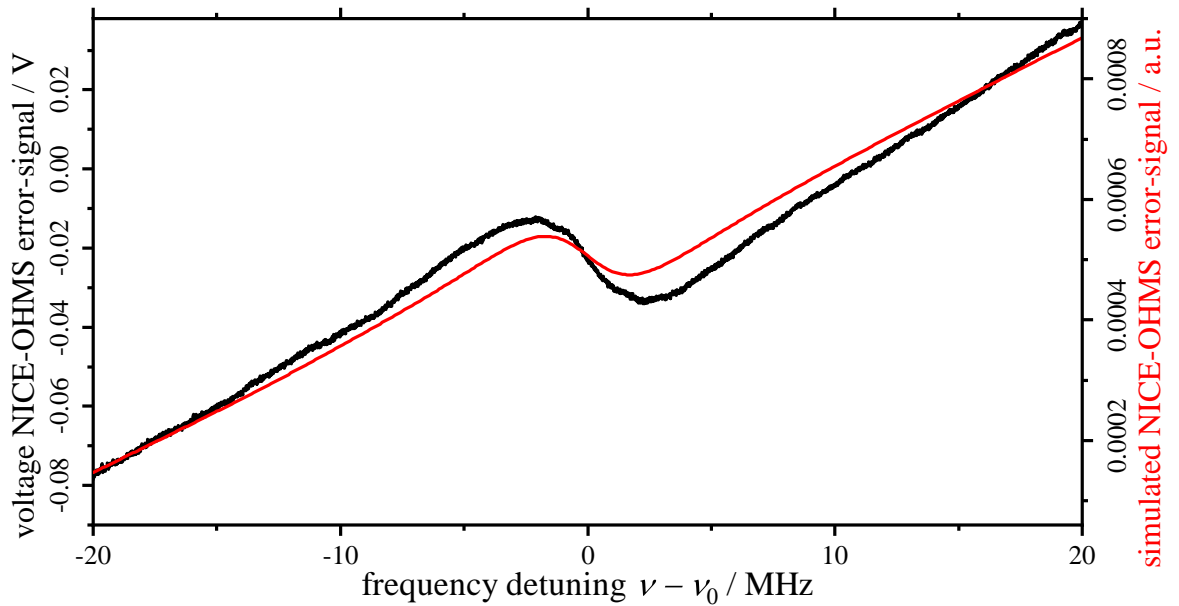

Figure 5.13: Comparison of the measured voltage signal of the NICE-OHMS error signal with the simulated error signal plotted versus the frequency deviation $\nu - \nu_0$ from the resonant frequency of the HFS component "j" of the P(33)6-3 iodine line.

Figure 5.13 shows a comparison between the detected NICE-OHMS signal of line "j" (black) and the simulated signal. As the simulated data are relative values and the experimentally obtained data are voltage values of the mixer output, the simulated data in the figure have been scaled to fit the slope from the Doppler broadened background. When comparing the two signals, it is noticeable that the dispersion signal is slightly smaller. As many factors play a role in the simulation, as stated earlier in this thesis, agreement between the simulation and experimental results is considered quite good.

Since there is no zero crossing at the center of the Doppler free HFS iodine transition due to the Doppler background, this NICE-OHMS signal cannot directly be used to stabilize the frequency of the emitted laser light. With the NICE-OHMS error signal it would be only possible to stabilize the frequency to the Doppler broadened spectrum from all HFS components of the iodine transition. To create a suitable error signal for Doppler free HFS components, the NICE-OHMS signal must be further processed.

5.1.6 Wavelength Modulated NICE-OHMS

To generate an error signal from the NICE-OHMS signal that is zero at the HFS-line center a lock-in technique is used. By modulating the cavity length and thus the laser wavelength at low frequency, and detecting the resulting second harmonic component of the NICE-OHMS signal, approximately the second derivative of the NICE-OHMS signal can be obtained [23]. The linear component due to the Doppler broadened background is removed and a zero-crossing error signal is generated at each HFS iodine line. The function generator of the lock-in amplifier (Standford Research Systems SR830 DSP Lock-in Amplifier) generates an AC modulation signal with frequency $f_{\mathrm{wm}} = 2.5\,\mathrm{kHz}$ and amplitude U_{wm}. This signal is given to one mirror piezo of the cavity, so that the length of the cavity and thus eigenfrequency changes periodically by ± 3 MHz. Since the DL Pro laser is stabilized to the length of the cavity using the PDH method, the optical frequency of the laser follows the change in length of the cavity. The amplitude U_{wm} is chosen so that the resulting peak-to-peak wavelength modulation $\Delta\nu_{\mathrm{wm}} = 6$ MHz matches the width of a Lamb-dip of the absorption spectrum [26]. With the lock-in amplifier the modulated NICE-OHMS error signal is bandpass filtered and its component at the 2nd harmonic of the modulation frequency is detected. The phase ϕ_{wm} between detection and modulation frequency f_{wm} is adjusted in such a way that the slope in the zero crossing becomes maximum. Figure 5.14 shows the wm-NICE-OHMS error signal generated by this method.

It can be seen that in the wm-error signal generated from the NICE-OHMS error signal the Doppler background is removed and thus the zero crossing now corresponds to the position of the HFS component of iodine.

The wm-error signal is send to the PID controller included in the DLC Pro laser controller. This PID controller controls the length of the build up resonator via a piezo transducer on the second mirror in a way that the wm-error signal remains zero. This
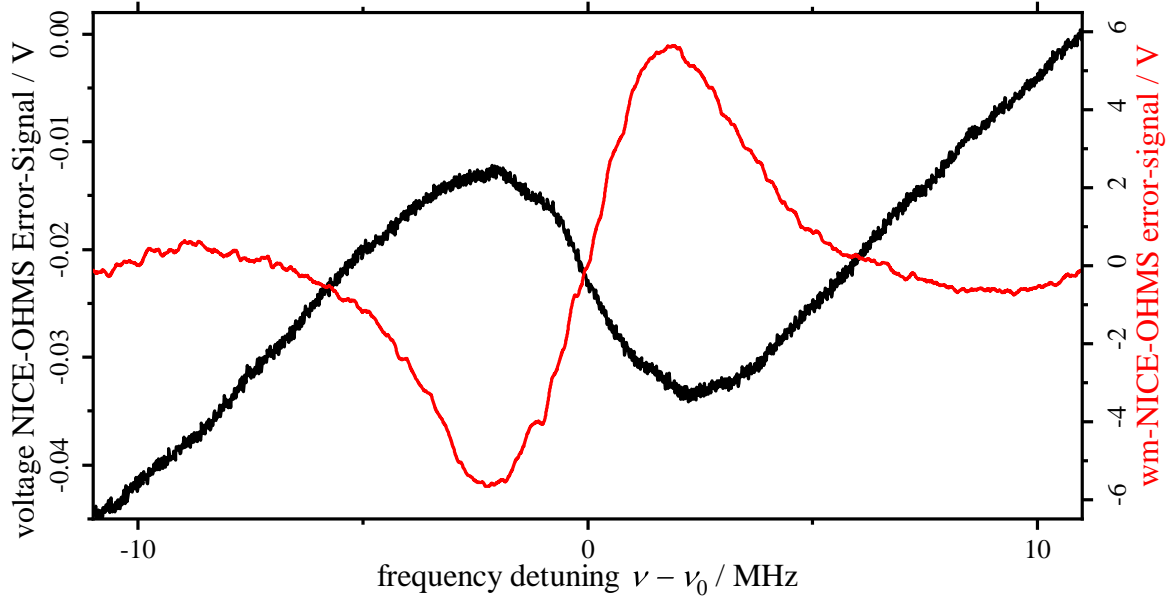
Figure 5.14: Comparison between the measured NICE-OHMS error signal (black) and the 2nd order wm-NICE-OHMS error signal (red) of the HFS component "j" of the iodine line P(33) 6-3 measured with the lock-in amplifier as a function of the frequency deviation from HFS component "j".

means that the eigenfrequency of the resonator is stabilized to the center of the selected HFS component of iodine. As the frequency of the laser light ν_{DL} from the DL Pro is stabilized to the eigenfrequency of the resonator using the PDH method, the frequency of the light is also stabilized to the iodine line.

The wm-NICE-OHMS signal is simulated and compared to the observed wm-signal (see figure 5.15). Both signals match quite well, with slight deviations in width and slope between the two signals. The width of the signal is affected by the modulation amplitude $\Delta\nu_{\mathrm{wm}}$ and this may have varied between simulation and experiment. From the comparisons of the observed NICE-OHMS signals with the simulation, it is clear that the observed and chosen parameters (see section 5.1.4) for the simulation fit well with the experimental observations.
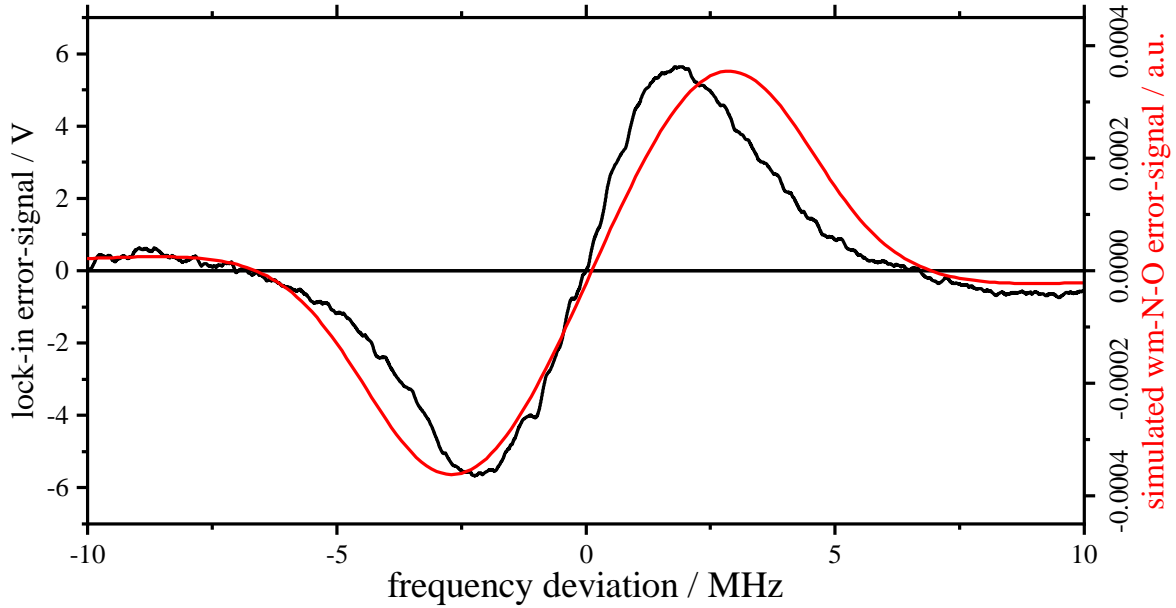
Figure 5.15: Measured wm-NICE-OHMS error signal (black) generated by the lock-in amplifier and simulated error signal (red) versus the frequency deviation from HFS component "j" of the P(33)6-3 iodine line.

5.2 Frequency Measurements

In this section, the results of absolute frequency and frequency stability are presented. In these measurements, the DL Pro laser is stabilized to the HFS line "j" of the P(33)6-3 transition using the wm-NICE-OHMS method.

5.2.1 Frequency Instability

A frequency measurement is performed against the PTB frequency comb to measure the instability and absolute frequency (see Section 3.2). To determine the exact absolute frequency with the frequency comb, the beat frequency between the DL Pro and an iodine stabilized He-Ne laser is determined in a first step (see section 3.1). This ensures that the frequency of the DL Pro is stabilized to the selected iodine HFS line. Based on this measurement, the order of the comb spike that creates the beat with the cw laser can be uniquely determined (see equation (3.1)). The frequency is measured over several hours and the calculated frequency deviation from $\nu_{\mathrm{P}(33),\mathrm{j}}^{\mathrm{BIPM}}$ [13] of a measurement is shown in Figure 5.16.

The measured values recorded over a measurement interval of 1 s are shown in light
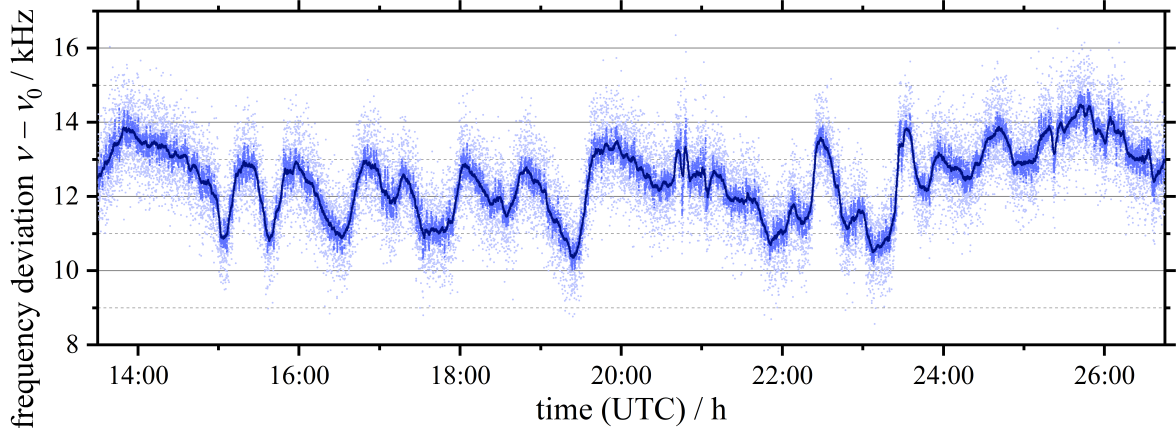
Figure 5.16: Frequency measurement of the diode laser stabilized with NICE-OHMS to the iodine line P(33) 6-3 "j" over time. The light blue dots show data with an averaging time of 1 s, whereas points in the darker blue shades indicate averaged values over 10 s and 100 s.

blue. The mean is then determined from these data by means of a moving average over a time interval of 10 s (blue) and 100 s (dark blue). Using the averaged values slow variations can be seen more easily. With a averaging time of 1 s, the frequency fluctuates within an interval of 4 kHz. For longer averaging times, the mean of the frequency fluctuated over an interval of up to 2-3 kHz.

Figure 5.17 shows the Allan deviation $\sigma_y(\tau)$ over the averaging time τ determined from the beat frequency measurements. In blue one of the first measurements with the EOM of AdvR (KTP) is shown and in black a later measurement with the EOM of Jenoptik (LiNbO$_3$) (see section 5.3.1). For comparison, the Allan deviation of an iodine-stabilized He-Ne is shown in red.

For averaging times smaller than 100 s it can be seen that the stability of the NICE-OHMS stabilized DL Pro's is better than that of an iodine stabilized He-Ne. With the EOM of Jeoptik, an instability of $\sigma_y = 1.4 \cdot 10^{-12}$ is obtained for an averaging time of 1 s. Up to an averaging time of just under 30 s, σ_y decreases with $1/\sqrt{\tau}$. For longer averaging times, however, σ_y increases again above the instability of the He-Ne laser. But the instability does not exceed a value of $\sigma_y = 2 \cdot 10^{-12}$ and decreases again for averaging times longer than 1000 s.

In order to compare the observed short-term stability of the laser stabilized with the NICE-OHMS method with the fundamental limits, it is assumed that the signal-to-noise ratio detected by the APD (sensitivity $S_{PD} = 0.5\,\frac{A}{W}$) is limited by the photon shot-
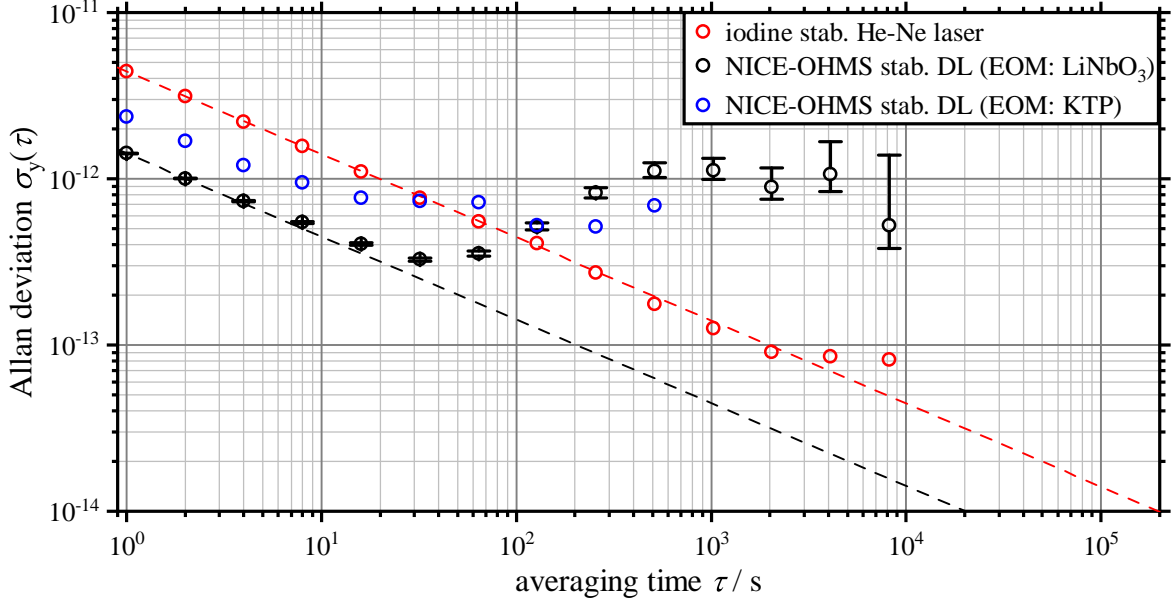
Figure 5.17: Measured Allan deviation σ_y of the diode laser stabilized by the NICE-OHMS method initially with AdvR (KTP) EOM (blue) and later with Jenoptik (LiNbO$_3$) EOM (black) and of an iodine-stabilized He-Ne laser versus the averaging time τ.

noise. With the parameters saturation $S = 1.19$ and saturation intensity $I_{\text{sat}} = 10.3 \frac{\text{W}}{\text{cm}^2}$ used for simulation, a power $P_{\text{in}} = 1.6 \, \text{mW}$ before the cavity and a power $P_{\text{out}} = 54 \, \mu\text{W}$ in transmission are obtained. The photocurrent from P_{out} in the APD has a noise spectral density of $S_I = 8.6 \cdot 10^{-24} \frac{\text{A}^2}{\text{Hz}}$ using equation (4.6). Here the internal gain of the APD is set to M=1. Figure 5.29 in section 5.3.5 shows the signal, normalized to the input power. With an input Power $P_{\text{in}} = 1.6 \, \text{mW}$ and a sensitivity of $S_{\text{PD}} = 0.5 \frac{\text{A}}{\text{W}}$, a slope of $D = 4.5 \cdot 10^{-14} \frac{\text{A}}{\text{Hz}}$ is determined for the wm-NICE-OHMS signal. Using equation (4.5), an expected instability of $\sigma_y(\tau) = 1 \cdot 10^{-13} \, \tau^{-1/2}$ from the simulation is obtained. As with the Toptica beta demonstrator (see section 4.2.3), the simulated instability for the NICE-OHMS stabilized laser is about a magnitude smaller than the measured instability. Again, technical noise could be the reason why the stabilized laser does not reach the simulated short term instability.

Since the stability degrades at longer averaging times of several 10 s, environmental influences such as room temperature are assumed to be the cause of this effect. Now the question arises, in which way the environment influences the stabilized laser system. For this purpose, further parameters are measured over time in parallel to the frequency measurement with the frequency comb. In a first approach, the room temperature near

the cavity, the power of the light changes in front and behind of the cavity and the residual amplitude modulation (RAM) at the PDH modulation frequency generated by the EOM are measured (see section 5.3.1). Additionally, the feedback voltage signal of the PDH stabilization is investigated, which changes the voltage of the DL Pro laser and should correct slow influences (see section 5.1.3). Figure 5.18 shows an overview of the comparison between the various parameters and the frequency deviation based on an example measurement.

In the long term behavior no correlation can be seen, which rules out a significant direct influence of the parameters on the laser frequency. In shorter times fast oscillation with a changing frequency can be seen. If the power of the light in front of the cavity P_{front} is compared with the fast frequency fluctuations, a correlation can be seen. Also the power behind the cavity P_{trans} is also correlated with the fast frequency fluctuations, only with opposite sign compared to the power fluctuations in front of the cavity. The influence of the temperature on the frequency of the free running diode laser is corrected with the voltage U_{cor} of the PDH controller, which is visible in figure 5.18. It is noticeable that with slow change in temperature, the frequency of oscillations changes within the frequency deviation. This indicates etalon effects in the beam path, where the path length depends on the temperature. Finally, correlations between RAM and frequency can be seen on short time scales. However, the phase relationship of the correlation seems to vary with time.

Overall the problem arises, by which parameter and at which point of the experiment the frequency of the stabilized laser is influenced. In the next section (section 5.3), the various frequency influences will be discussed in detail. Additionally it will be examined how the settings of the Lock-In or the EOM can shift the frequency.
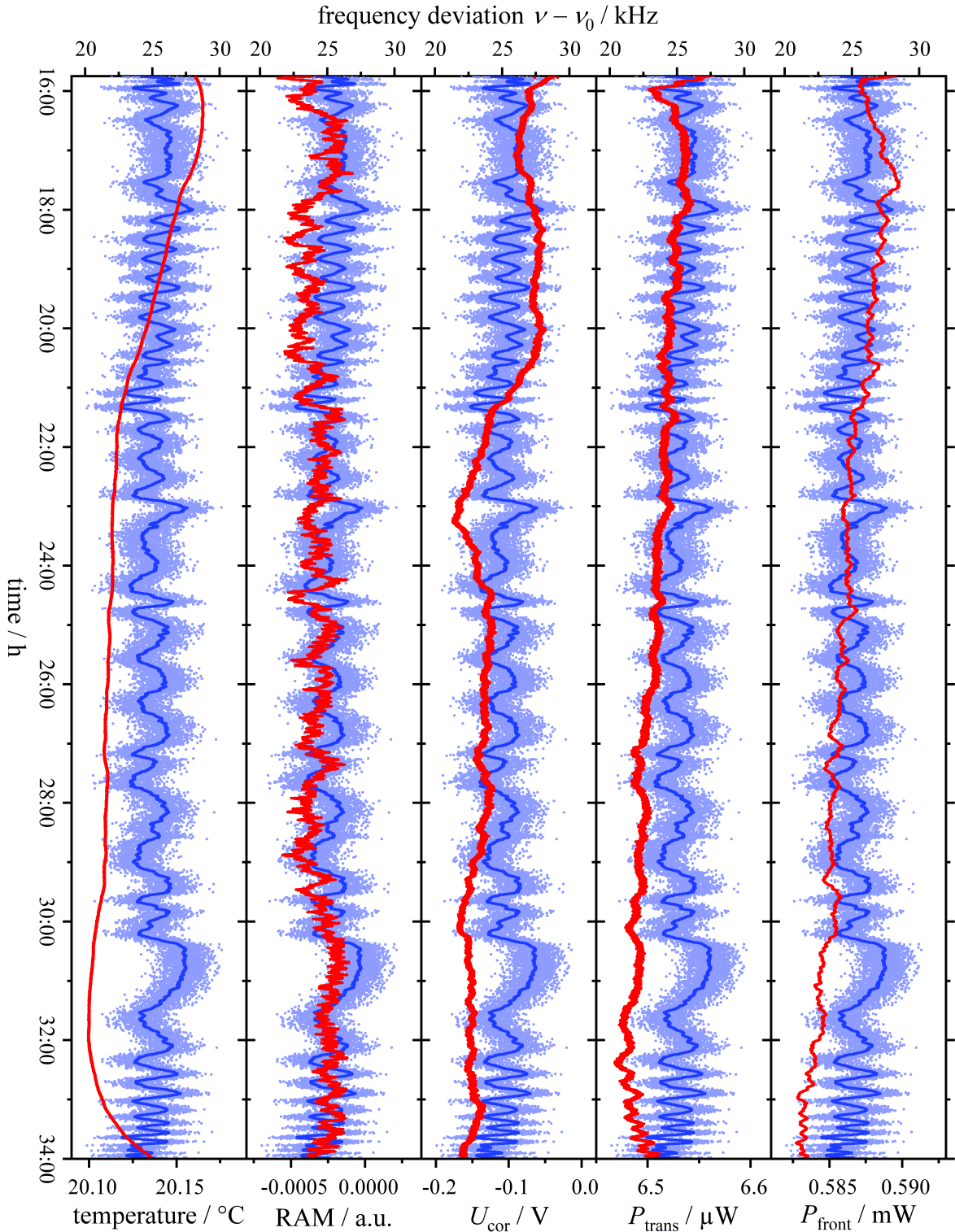
Figure 5.18: Frequency over a period of several hours of the diode laser stabilized by the NICE-OHMS method (blue) compared with the simultaneously measured power variation P_{front} in front of and P_{trans} behind the cavity, the voltage of the PDH correction U_{cor}, the RAM of the EOM and the temperature in the environment of the cavity.

5.2.2 Frequency Uncertainty

In this section, the frequency uncertainty after repeated stabilization to the HFS transition "j" of iodine will be investigated using the NICE-OHMS method and compared with the accuracy of an iodine-stabilized He-Ne.

In course of this work the absolute frequency was determined by means of a beat frequency measurement in comparison to three different systems: A Toptica frequency comb, the MenloSystem frequency comb mentioned in section 3.2 (both are referenced to PTB's Cs-fountain clock) and the PTB Iodine stabilized He-Ne 03/86 (see chapter 5.2.1). To estimate the statistical uncertainty of that measurement, a histogram of the 1 s average frequency values is created. The total uncertainty u is the root sum squared of the statistical standard deviation σ of the corresponding Gaussian distribution and the systematic uncertainty of the reference u_{ref} (He-Ne: 10^{-11}, Cs: $< 10^{-15}$, see chapter 3):

$$u = \sqrt{\sigma^2 + u_{\mathrm{ref}}^2} \tag{5.6}$$

Figure 5.19 shows an example of the histogram of an absolute frequency measurement and Table 5.1 shows the results of these measurements. This is for a total of 17 measurements from which the unweighted average value $\bar{\nu}_{\mathrm{abs}}$ is determined with statistical standard deviation.
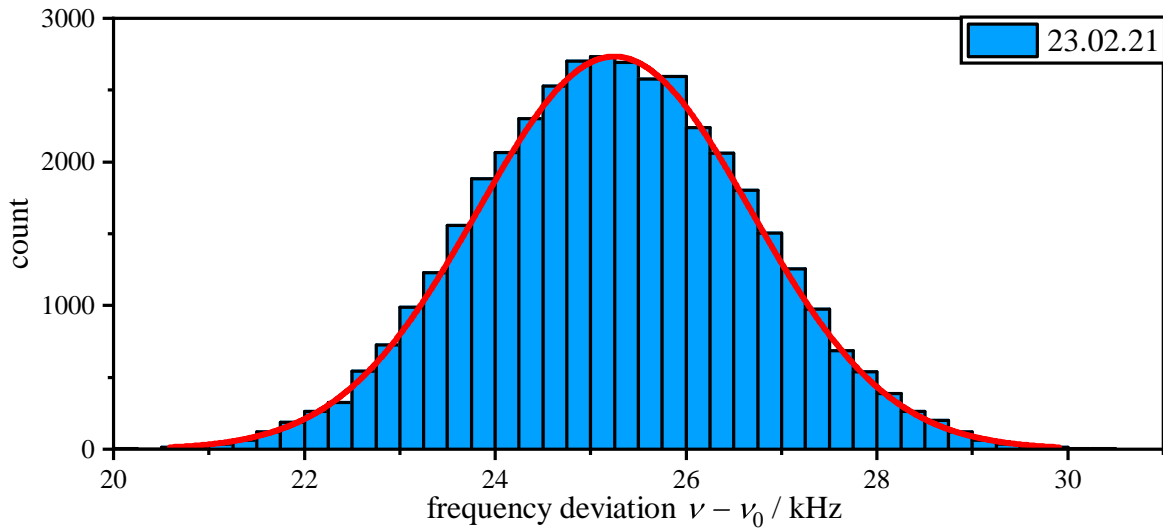

Figure 5.19: Histogram of the frequency deviation (averaging time 1 s) of the diode laser stabilized with the NICE-OHMS method on the HFS component "j" of the iodine line P(33)6-3 determined with the frequency comb.

Date	ν_{abs} / kHz	u / kHz	System
04.03.2019	473 611 473 811.0	1.9	TopticaComb
04.03.2019	473 611 473 812.4	1.3	TopticaComb
05.03.2019	473 611 473 798.1	2.8	TopticaComb
05.03.2019	473 611 473 800.9	10.6	PTB He-Ne 03/86
06.03.2019	473 611 473 781.8	2.6	TopticaComb
06.03.2019	473 611 473 784.1	10.5	PTB He-Ne 03/86
07.05.2019	473 611 473 782.3	10.5	PTB He-Ne 03/86
08.05.2019	473 611 473 786.5	10.0	PTB He-Ne 03/86
10.05.2019	473 611 473 793.3	10.1	PTB He-Ne 03/86
14.05.2019	473 611 473 806.4	10.1	PTB He-Ne 03/86
20.09.2020	473 611 473 846.6	1.2	MenloSystem
16.12.2020	473 611 473 848.2	1.6	MenloSystem
07.01.2021	473 611 473 842.4	1.1	MenloSystem
22.01.2021	473 611 473 834.1	1.0	MenloSystem
18.02.2021	473 611 473 853.0	1.9	MenloSystem
24.02.2021	473 611 473 855.2	1.4	MenloSystem
26.02.2021	473 611 473 862.8	2.1	MenloSystem
	473 611 473 817.2	29	

Table 5.1: Listing of the determined absolute frequencies of the diode laser stabilized by the NICE-OHMS method (Line P(33)6-3, "j") and their uncertainties u. Their unweighted average value $\bar{\nu}_{\mathrm{abs}}$ is given in the last line with its uncertainty, determined as standard deviation of these frequency values.

All absolute frequency measurements result in a mean frequency of $\bar{\nu}_{\mathrm{abs}} = 473\,611\,473\,817(28)\,\mathrm{kHz}$. Compared to the values given by the CIPM [13] of $473\,611\,473\,830(20)$ kHz (cell wall temperature 23 °C, coldfinger temperature 15 °C, 2 MHz peak-to-peak modulation amplitude, 20 mW power [93]) for the HFS transition "j" of the line P(33)6-3, the frequency measured here deviates by around -12 kHz, well within the combined uncertainties. Because the operating conditions are very similar to the ones of the CIMP values, no systematic corrections are applied to the measured values. In figure 5.20 the measured deviation of the absolute frequency ν_{abs} from the CIPM frequency ν_{CIPM} of the line P(33)6-3 "j" of the individual measurements from table 5.1 are shown graphically. In addition, the average deviation $\bar{\nu}_{\mathrm{abs}} - \nu_{\mathrm{CIPM}}$ with

the respective uncertainty (green dashed line) is plotted in green.

From the graph it can be seen that the average value over all measured values agrees with the frequency value of the line P(33)6-3 "j" given by CIPM.
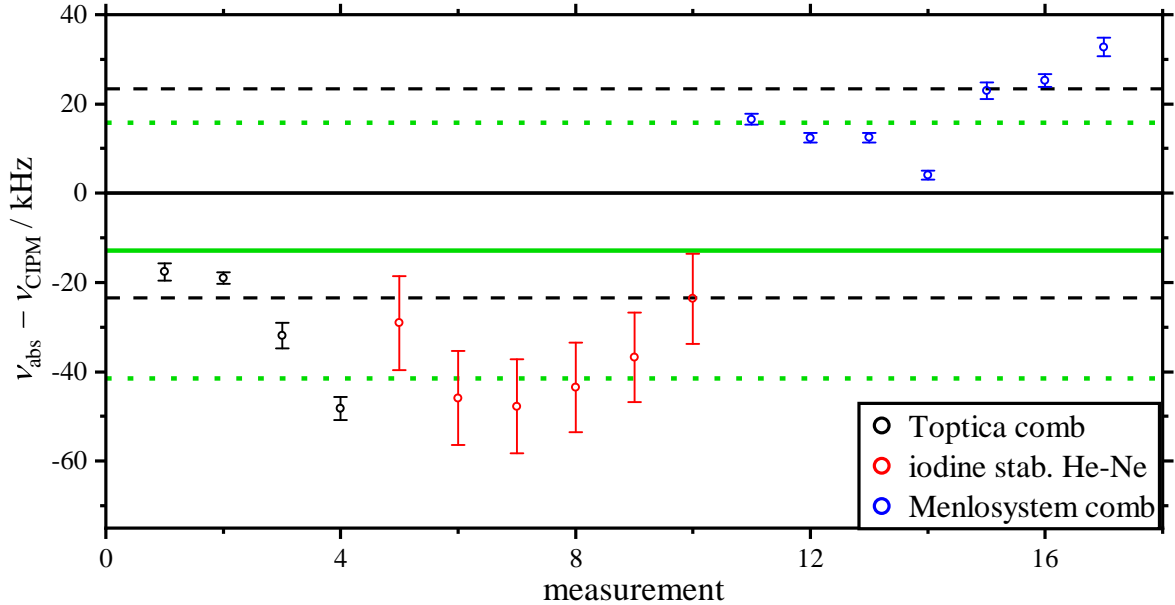

Figure 5.20: Obtained absolute frequencies of the DL Pro laser stabilized with the NICE-OHMS method onto the HFS component "j" of the line P(33)6-3 from different measurements compared to three different systems. The green solid line indicates the mean frequency with uncertainty (dashed line) determined over all measurements, whereas the black line is the absolute frequency indication of the CIPM value [13].

When looking at the individual measurements, it becomes visible that the measurements with the MenloSystem comb deviate from the values in comparison with the He-Ne and the Toptica comb by about 50 kHz on average. This can be explained by changes in the operating parameters of the NICE-OHMS method (see chapter 5.3). The greatest influence is exerted by the power within the cavity. In the measurements compared to the He-Ne and the Toptica comb, the power inside the cavity was about 8 mW. Whereas in the measurements in comparison to the MenloSystem comb, the power was approximately 15 mW. With the sensitivity of $\sim 6\,\frac{\text{kHz}}{\text{mW}}$ determined in section 5.3.7, this would imply a frequency shift of about 40 kHz.

Also the operating parameters, such as the parameters of the lock-in amplifier, have been slightly changed during the various measurements. With the frequency sensitivity from chapter 5.3, a corresponding shift of a few kHz can arise.

5.3 NICE-OHMS Systematic Effects

In this section, possible influences on the frequency of the stabilized laser are investigated. Different experimentally obtained sensitivities will be compared with simulated data. These investigations compromise the influence of the RAM of the EOM, the phase and frequency settings of the lock-in amplifier, the deviation of the NICE-OHMS modulation frequency from the FSR of the cavity and its phase setting and the power of the light are investigated. It will turn out that the multicomponent structure of the iodine spectrum has an important and often determined impact on the frequency accuracy and stability.

5.3.1 Residual Amplitude Modulation RAM (EOM)

Imperfection in the EOM cause amplitude modulation (RAM) in addition to the intended phase modulation [94]. Although the RAM is a relatively small signal, it may severely degrade the stability achievable with the PDH method. In the PDH error signal, the RAM acts as an offset, which influences the NICE-OHMS signal, too [95]. Thus the intersection with the zero line is shifted. Since the PDH method stabilizes to this zero point, there is a corresponding shift in the locked frequency. To investigate the RAM of an EOM, the experimental setup from figure 5.1 is extended as shown in figure 5.21.
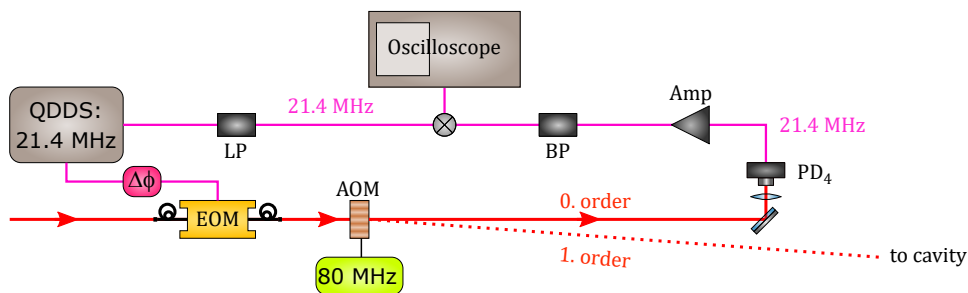

Figure 5.21: Setup sketch for the detection of RAM generated by the electro-optic phase modulator (EOM) in the form of an extension of the experimental setup from Figure 5.1. A low-pass filter (LP), a band-pass filter (BP), an amplifier (Amp), an acousto-optic modulator (AOM) and a photodiode (PD) are used.

As shown in the setup of figure 5.1, an AOM behind the EOM is used to suppress optical feedback from the cavity by using the 1st order diffracted light. A small part of the power of the light remains in the 0th order, which is detected by the photodiode PD_4. The detected AC signal from RAM is amplified, bandpass filtered and mixed with the phase shifted modulation frequency f_{ref}, which is generated with another channel of the QDDS that also provides the modulation signal similar to the reference for the PDH detection. The mixer output produces a DC signal proportional to the RAM.

To investigate the RAM of the two EOM used in the thesis, the frequency of the diode laser is stabilized to the HFS component "j" of the iodine line P(33)6-3 using the NICE-OHMS method and the frequency is measured in comparison to an iodine-stabilized He-Ne. For the EOM from AdvR (KTP), the temperature of the heat pad at the EOM is changed, resulting in a change of the RAM. Thus, the coefficient $\xi_{RAM} = (0.65 \pm 0.04)\,\frac{kHz}{mV}$ of the frequency deviation $\Delta\nu$ is determined on the basis of frequency measurements at different temperature settings of the heat pad. Despite a stable temperature, the RAM drifts leading to a calculated frequency deviation up to 10 kHz over time, as can be seen in figure 5.22 based on a long-term measurement of the RAM.
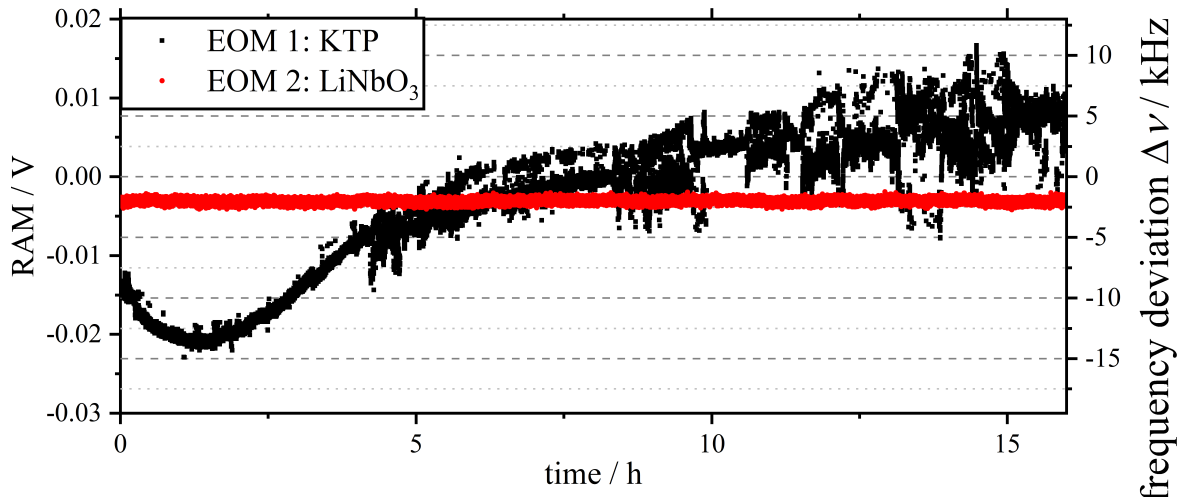
Figure 5.22: Measured RAM and the calculated frequency deviation $\Delta\nu$ of the (KTP) EOM (black) and the $LiNbO_3$ (red) used in this work over a time period of several hours.

Although strong RAM fluctuations occur over time, with the EOM of AdvR a suppression of the RAM as described in [96] would be possible with an applied DC voltage, to exclude the influence of the RAM on the frequency completely. But a very strong noise of the RAM of the AdvR EOM can be seen at certain time periods. That noise

causes a disturbance of the frequency stability of several kHz. This behavior has occurred repeatedly in the course of the investigations and indicates a defect of the AdvR EOM.

In comparison, the results of the RAM measurement with the Jenoptik EOM is shown in figure 5.22, too. Since the EOM from Jenoptik ($LiNbO_3$) does not have a temperature control, only the RAM itself is measured over time for this EOM. Using the coefficient $\xi_{RAM} = (0.65 \pm 0.04)\,\frac{kHz}{mV}$ from the measurements with the AdvR EOM, the measured RAM of the Jenoptik EOM is converted into a frequency deviation. The RAM noise of the Jenoptik is smaller compared to the KTP EOM and the RAM is stable over a long period of time. Thus, only an offset of the frequency of the light of the laser of a few kHz has to be taken into account. Because the defect of the AdvR EOM and the temporally stable behavior of the Jenoptik EOM, the EOM from Jenoptik is used in the further process of the thesis.
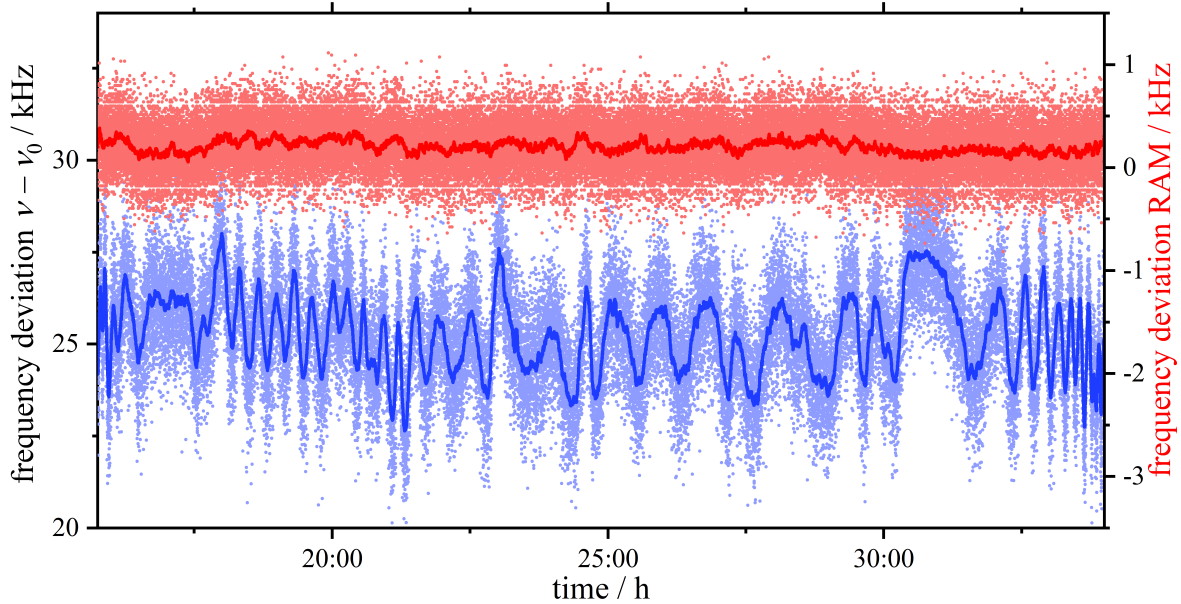
Figure 5.23: Comparison between the measured frequency deviation $\nu - \nu_0$ of the diode laser stabilized by the NICE-OHMS method (blue) and the parallel examined calculated frequency deviation $\Delta\nu_{RAM}$ due to RAM of the EOM (red).

Next, the frequency deviation $\Delta\nu_{RAM}$ due to the RAM of the Jenoptik EOM is to be compared with the frequency deviation $(\nu_{DL} - \nu_0)$ of the laser over time. For this purpose, the result of the measurements from figure 5.18 is shown again in detail in figure 5.23. The possible frequency deviation $\Delta\nu_{RAM}$ is shown from the measured RAM

signal (red). Both for the frequency deviation $(\nu_{\mathrm{DL}} - \nu_0)$ investigated with the comb and for the RAM data, the averaged values over 1 s and the moving average over 100 s calculated from these are shown.

In this case, the averaged expected frequency deviation $\Delta\nu_{\mathrm{RAM}}$ due to the RAM varies only by a few 100 Hz. In comparison, the frequency ν_{DL} of the light of the laser itself varies by a few kHz. Thus the RAM of the EOM can not be the reason for the observed frequency deviations. Nevertheless it can be seen that the fluctuations of both measurements are partly correlated. But the sign of the correlation changes with time. This could indicate that a common cause for the fluctuations, such as environmental influences, are responsible.

5.3.2 Sensitivities to the Parameters to Wavelength Modulation

In this section, the influences on the absolute frequency from the parameters of the wavelength modulation used in the wm-NICE-OHMS method will be investigated. The first important parameter in the generation of the wm-NICE-OHMS error signal is the amplitude of the applied wavelength modulation $\Delta\nu_{\mathrm{wm}}^{\mathrm{Lock}}$. Increasing the amplitude of the modulation results in a larger range of the Doppler background being scanned. Thus, when generating the error signal by means of the 2nd harmonic, more of the non-linearities of this background is taken into account. This leads to an offset of the error signal and a shift of the frequency of the laser similar to an iodine stabilized He-Ne laser [66].

To check the amplitude of the frequency modulation of the stabilized NICE-OHMS system, the beat with an iodine-stabilized He-Ne laser is observed (see fig. 3.1). The modulation of the He-Ne is switched off and the laser is not stabilized to an iodine line, so that the line width is much smaller (a few 10 kHz [83]) than the modulation amplitude of a few MHz of the NICE-OHMS stabilized laser. With a spectrum analyzer the dependence of the peak-to-peak modulation amplitude on the voltage amplitude of the lock-in amplifier was determined to $(6.7 \pm 0.12)\,\mathrm{MHz/V}$.

Different peak-to-peak modulation amplitudes in the range of $\Delta\nu_{\mathrm{wm}}^{\mathrm{Lock}} = 2\text{-}12\,\mathrm{MHz}$ are set and the laser frequency is averaged for about 1 minute. Figure 5.24a shows the frequency deviation of the NICE-OHMS stabilized laser system versus the modulation amplitude $\Delta\nu_{\mathrm{wm}}^{\mathrm{Lock}}$. In this plot the modulation peak-to-peak amplitude of $\Delta\nu_{\mathrm{wm}}^{\mathrm{Lock}} = 6\,\mathrm{MHz}$ is defined as reference and the error bars represent the statistical uncertainty of the frequency measurement. By means of a linear fit a sensitivity coefficient $\xi_{\mathrm{mod}}^{\mathrm{Lock}} =$

(-12.3 ± 0.9) $\frac{\text{kHz}}{\text{MHz}}$ is determined (He-Ne: $\xi_{\text{mod}}^{\text{HeNe}} = (-10\pm0.3)$ $\frac{\text{kHz}}{\text{MHz}}$, [13]). The coefficient is too small to have a significant influence on the absolute frequency stability of the laser, since the amplitude $\Delta\nu_{\text{wm}}^{\text{Lock}}$ is estimated not to vary by more than a few 10 kHz over several hours.

However, this effect leads to a frequency offset, which must be taken into account when referring to the undisturbed frequency of the iodine HFS line.
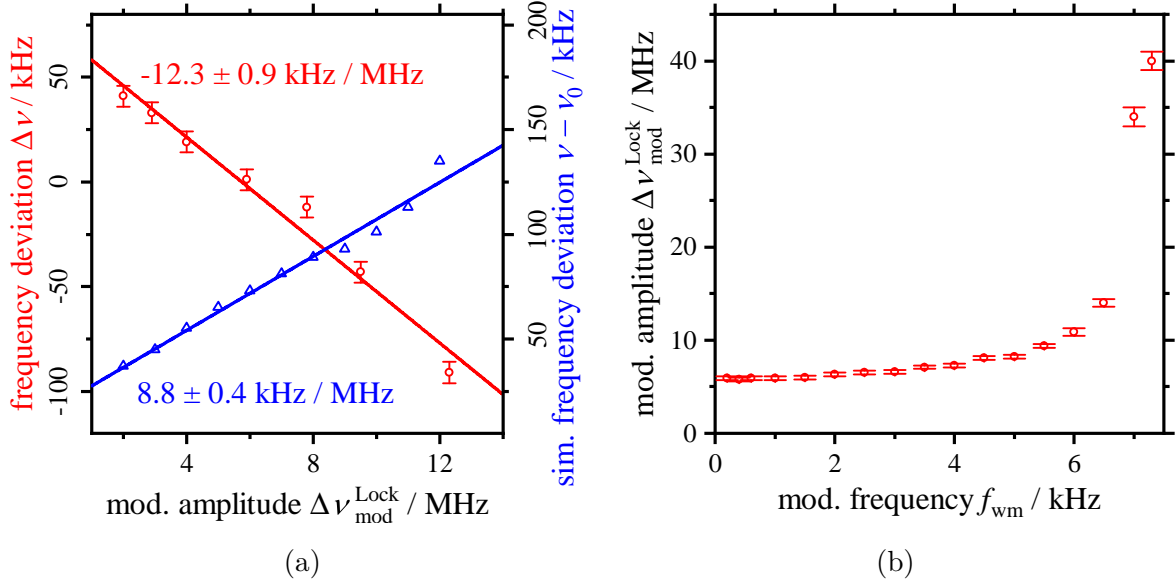

Figure 5.24: Influence of the wavelength modulation parameters on the optical frequency of the laser stabilized with the NICE-OHMS method. In (a) the shift $\Delta\nu$ of the optical frequency due to the change of the peak-to-peak modulation amplitude $\Delta\nu_{\text{wm}}^{\text{Lock}}$ is shown and in (b) the influence of the modulation frequency f_{wm} on the modulation amplitude $\Delta\nu_{\text{wm}}^{\text{Lock}}$.

For comparison, the simulated frequency deviation $\nu - \nu_0$ as a function of the modulation amplitude $\Delta\nu_{\text{wm}}^{\text{Lock}}$ is plotted in figure 5.24a (blue). The magnitude of the simulated frequency deviation is similar, but the sign of the deviation is different $\xi_{\text{mod,sim}}^{\text{Lock}} = (8.8 \pm 0.4)$ $\frac{\text{kHz}}{\text{MHz}}$. How can it come to a different sign, although it can be seen in figure 5.13 that the NICE-OHMS signal, from which the wm-error signal is generated, is comparable between experiment and simulation? In general the frequency deviations are generated by an offset in the wm-NICE-OHMS error signal, which is generated by nonlinearities of the Doppler background. As the amplitude of the frequency modulation $\Delta\nu_{\text{wm}}^{\text{Lock}}$ changes, the range of the sampled background is also varied, thus introducing the influence. To determine the cause of the different sign, the simulated

error signal in the zero-crossing region is shown in figure 5.25 as a function of frequency for different modulation amplitudes $\Delta\nu_{\text{wm}}^{\text{Lock}}$.
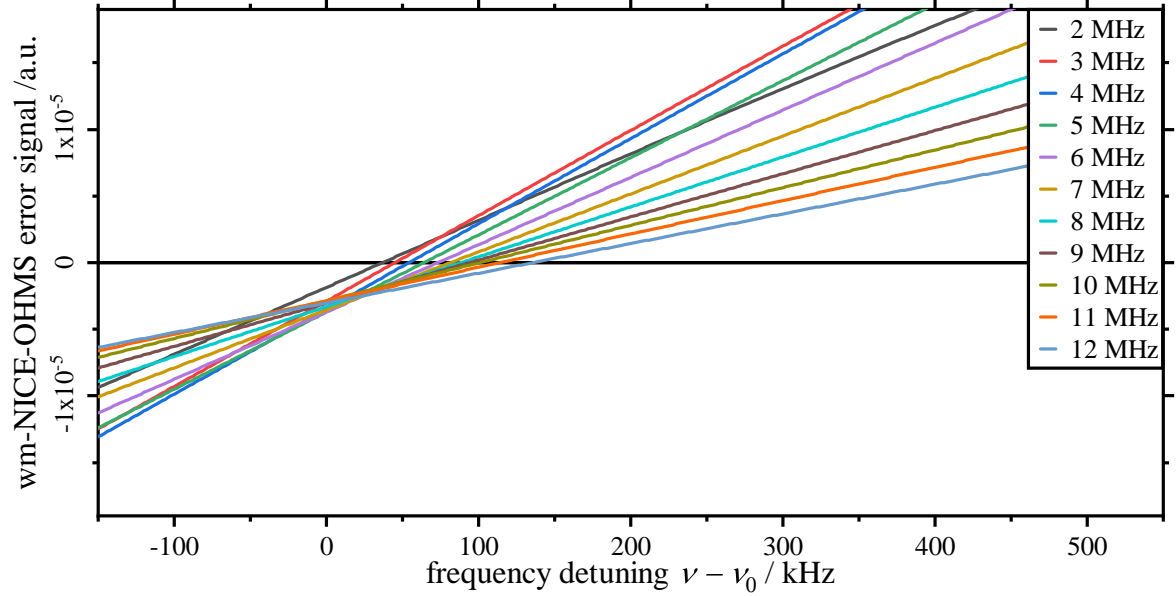

Figure 5.25: Zoom-in close to the zero crossing of the simulated wm-NICE-OHMS error signal for different modulation amplitudes versus frequency deviation from the undisturbed line center.

Figure 5.25 shows that for different modulations amplitudes $\Delta\nu_{\text{wm}}^{\text{Lock}}$ in addition to the offset, the slope of the error signal also changes significantly. Both effects lead to a common intersection point at an offset below the actual zero error signal. If the error signal in the experiment had an additional offset e.g. due to the electronics, the laser could have been locked to an wm-NICE-OHMS error signal below the intersection point shown in figure 5.25 and thus to a different sign of the sensitivity. This could explain the discrepancy between the measured and simulated sensitivity.

To rule out detrimental mechanical resonances of the PZT mirror, the dependence of the modulation frequency $f_{\text{wm}}^{\text{Lock}}$ on the amplitude $\Delta\nu_{\text{wm}}^{\text{Lock}}$ was investigated. A resonance could lead to big sensitivities of environmental parameters which would have an influence on the absolute frequency $\Delta\nu$. The modulation voltage of the lock-in is adjusted so that the amplitude is 6 MHz at low modulation frequencies and for different modulation frequencies in the range of $f_{\text{wm}}^{\text{Lock}} = 0\text{-}10\,\text{kHz}$ the respective amplitudes are determined. The results are shown in Figure 5.24b. At a frequency of $f_{\text{wm}}^{\text{Lock}} = 7.5\,\text{kHz}$, a first resonance of the PZT mirror can be identified. Also at higher frequencies further resonances could be observed. Thus, to stay away from resonances a modulation

frequency $f_{\mathrm{wm}}^{\mathrm{Lock}} < 4\,\mathrm{kHz}$ is used for the setup.

5.3.3 NICE-OHMS Modulation Frequency and FSR

When stabilizing with the NICE-OHMS method, the modulation frequency $f_{\mathrm{mod}}^{\mathrm{FSR}}$ of the FSR should be exactly equal to the FSR of the cavity. If it does not match exactly, the sidebands will not be completely passed by the cavity. Because of the dispersion of the medium, the frequency distance between the upper sideband and the carrier shifts differently compared to the distance between the lower sideband and the carrier. As a result, the balance between the transmission factors $\hat{T}^{\mathrm{cav}}$ (see equation (2.80)) is disturbed and the error signal is affected (see figure 5.11).

To investigate frequency shifts $\Delta\nu$ due to mismatch between modulation frequency and the FSR, the laser is stabilized to the line P(33) "j" using the NICE-OHMS method. The laser frequency is measured by the beat frequency to an iodine stabilized He-Ne laser. In the stabilized state, the modulation frequency $f_{\mathrm{mod}}^{\mathrm{FSR}}$ of the GHz sidebands is varied every few minutes and the change of the average beat frequency is observed. The frequency shifts determined from the beat signal $\Delta\nu$ are plotted against the modulation frequency $f_{\mathrm{mod}}^{\mathrm{FSR}}$ in figure 5.26.
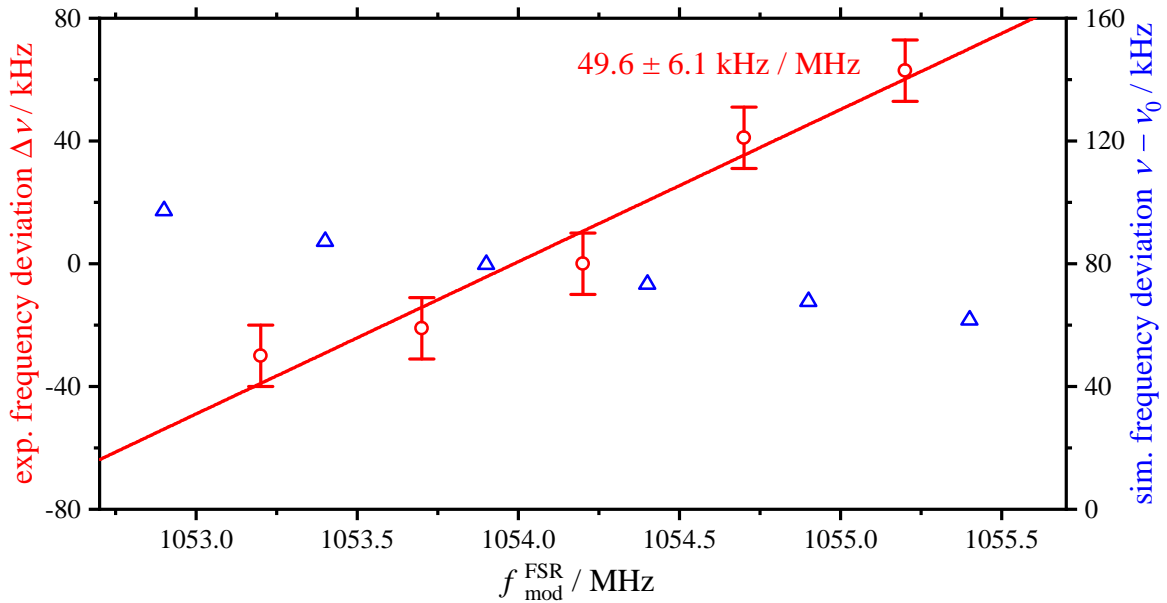

Figure 5.26: Measured (red) and simulated (blue) frequency shift $\Delta\nu$ of the laser locked with NICE-OHMS to iodine line P(33) 6-3 "j" as a function of the set FSR modulation frequency $f_{\mathrm{mod}}^{\mathrm{FSR}}$ with calculated linear regression.

A linear regression is used to determine the sensitivity coefficient for the deviation as $\xi_{\mathrm{mod}}^{\mathrm{FSR}} = (49.6 \pm 6.1)\,\frac{\mathrm{kHz}}{\mathrm{MHz}}$.

In addition, the simulated frequency sensitivity to the FSR modulation frequency $f_{\mathrm{mod}}^{\mathrm{FSR}}$ is also shown in figure 5.26. It is much smaller ($\xi_{\mathrm{mod,Sim}}^{\mathrm{FSR}} = -3.6\,\frac{\mathrm{kHz}}{\mathrm{MHz}}$) thus according to the simulation results should not have a large influence on frequency fluctuations over time. The discrepancy between simulation and experiment are partially be explained by the phase variations due to the high frequency of 1 GHz signals within the electronic components in the form of cable lengths. These variations are not taken into account in the simulation. Investigations have shown that different cable lengths and delays in electronic devices introduce frequency dependent phase shifts in the NICE-OHMS detection phase of 20 °/MHz (approximately 11 m cable). Together with the sensitivity to the NICE-OHMS phase of $\xi_{\mathrm{phase}} = (0.68 \pm 0.05)\,\frac{\mathrm{kHz}}{°}$ (see section 5.3.5) the phase shift would lead to an additional sensitivity of about $20\,\frac{\mathrm{kHz}}{\mathrm{MHz}}$.

5.3.4 Active FSR Tracking

As deviations of the sideband frequency from the FSR lead to changes in the frequency of the stabilized laser, ideally the modulation frequency $f_{\mathrm{mod}}^{\mathrm{FSR}}$ should always be equal to the FSR. However, to vary the frequency of the stabilized laser, the length of the cavity has to be changed. This and environmental influences like temperature and air pressure in turn changes the FSR of the cavity. For this reason, the modulation frequency should be corrected at the same time. To compensate these influences and to ensure that the modulation frequency matches the FSR, the FSR is actively tracked. For this purpose, a dual-frequency modulation (DFM) technique according to DeVoe and Brewer [97] is used.

This method employs the same dual frequency modulation as for the NICE-OHMS, where the carrier frequency is stabilized via PDH to the cavity resonance. From the phase relation between the FSR sideband and the PDH sidebands an amplitude modulation at offsets $f_{\mathrm{mod}}^{\mathrm{FSR}} \pm f_{\mathrm{mod}}^{\mathrm{PDH}}$ arises in the reflected light analogous to the PDH method depending on the frequency mismatch (see figure 5.27). This can be detected by a photo detector mixed with a reference frequency at $f_{\mathrm{mod}}^{\mathrm{FSR}} - f_{\mathrm{mod}}^{\mathrm{PDH}}$ to create an error signal.

Figure 5.28 shows the schematic structure of the stabilization of the modulation frequency on the FSR used in the experiment. In addition to the Quad-DDS at $f_{\mathrm{mod}}^{\mathrm{PDH}}$ for
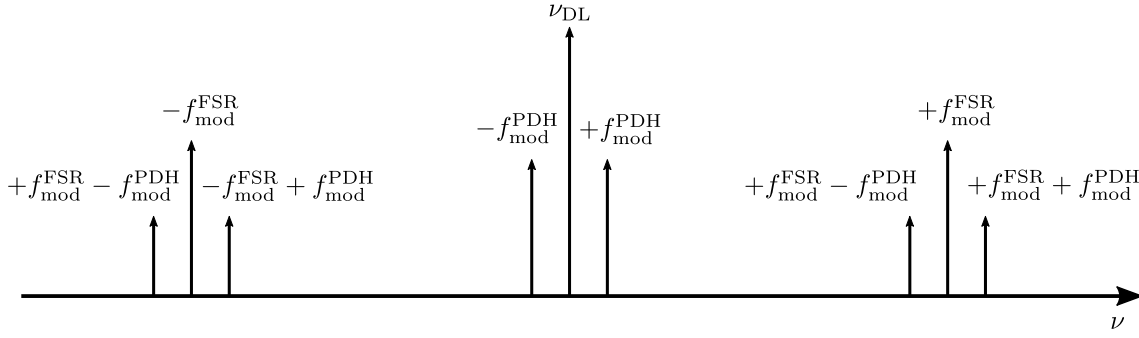
Figure 5.27: Sketch of all frequency components of the frequency modulated laser light. Where ν_{DL} is the frequency of the laser, $f_{\mathrm{mod}}^{\mathrm{PDH}}$ is the frequency of the PDH modulation and $f_{\mathrm{mod}}^{\mathrm{FSR}}$ is the frequency of the FSR modualtion.

PDH and the synthesizer 2 at $f_{\mathrm{mod}}^{\mathrm{FSR}}$ for NICE-OHMS a second phase locked synthesizer 1 is used to produce a reference signal at $f_{\mathrm{mod}}^{\mathrm{FSR}} - f_{\mathrm{mod}}^{\mathrm{PDH}}$.

A phase-frequency comparator is used to compare the phase difference between the two synthesizers with the reference $f_{\mathrm{mod}}^{\mathrm{PDH}}$ from the QDDS. A voltage signal is output to synthesizer 1 to corrected its frequency in such a way that the phase between both synthesizers is equal to the phase of $f_{\mathrm{mod}}^{\mathrm{PDH}}$. Thus a constant phase relation of the reference signal for the FSR lock is maintained.
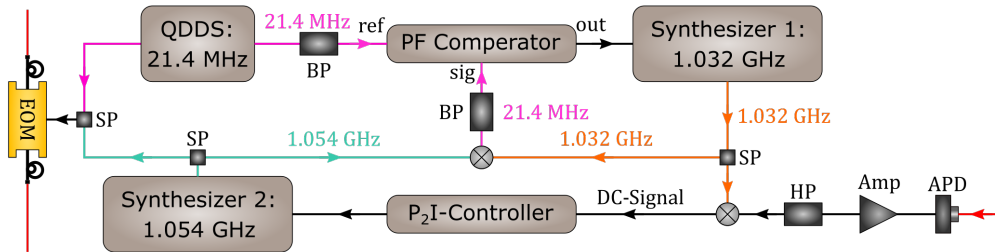
Figure 5.28: Electronic setup for active phase stabilization of the modulation frequency $f_{\mathrm{mod}}^{\mathrm{FSR}}$ (turquoise) on the FSR of the cavity. BP is a band-pass filter, HP a high-pass filter, SP a splitter, Amp an amplifier, APD an avalanche photo diode and PF a phase frequency comparator. PDH frequency $f_{\mathrm{mod}}^{\mathrm{PDH}}$ is shown in purple and the reference signal at $f_{\mathrm{mod}}^{\mathrm{FSR}} - f_{\mathrm{mod}}^{\mathrm{PDH}}$ in orange.

An Avalanche Photo Diode (APD) is used to detect a portion of the light reflected from the cavity. This signal is amplified (Amp), high pass filtered and mixed with the reference signal from synthesizer 1. The mixed signal provides a DC error signal with

which the frequency of synthesizer 2 is stabilized to the curent FSR of the cavity. To keep the error signal at 0, the output of a P$_2$I controller is sent to the tuning input of synthesizer 2. As shown already in figure 5.1 the FSR modulation frequency of synthesizer 2 ($f_{\text{mod}}^{\text{FSR}}$) and the PDH modulation frequency ($f_{\text{mod}}^{\text{PDH}}$) of the QDDS are fed to the EOM via a splitter (SP).

5.3.5 Frequency Sensitivity to the NICE-OHMS Phase

In this section the influence of the phase $\Delta\phi$ between the reference signal and the NICE-OHMS error signal $S_\phi^{\text{NO}}(\phi, \nu)$ (see section 5.1) on the frequency ν_{DL} of the locked laser will be investigated. With this phase it is possible to detect the dispersion ($\phi = 0$) and the absorption part ($\phi = \frac{\pi}{2}$) of the saturated iodine spectrum (see section 2.5.1). If the Doppler broadened transmission is mirror symmetric with respect to the Lamb-dip as in the case of a single absorption line (cf. figure 2.16), the error signal disappears in the resonance region near the Lamb-dip when the absorptive part is considered. However, in the case of iodine, many HFS lines overlap and the Doppler broadened profile is not symmetric. As a result, an absorption signal is still present at the resonance (see figure 2.18). If the wm-NICE-OHMS signal of the lock-in is considered, this effect results in an offset from the zero line if the phase does not perfectly suppress the absorption signal. How is this offset connected with the position of the zero crossing of this signal? If figure 5.29 is considered, simulated wm-NICE-OHMS error signals are shown for two phase positions with a phase difference of $\frac{2}{\pi}$, so that in each case the dispersion (black) or absorption (red) signal is maximal.

Since external influences on the phase are well below 90 °, the effect of small phase changes $\Delta\phi$ of a few ° on the frequency $\Delta\nu_{\text{DL}}$ shall be estimated here. For this purpose the error signal $S_\phi^{\text{NO}}(\phi, \nu)$ is written as the sum of two parts:

$$S_\phi^{\text{NO}}(\phi, \nu) = \cos\phi \cdot S_0(\nu) + \sin\phi \cdot S_{\frac{\pi}{2}}(\nu) \tag{5.7}$$

Here $S_0(\nu) = S_\phi^{\text{NO}}(\phi = 0, \nu)$ is the dispersion part and $S_{\frac{\pi}{2}}(\nu) = S_\phi^{\text{NO}}\left(\phi = \frac{\pi}{2}, \nu\right)$ the absorption part. The zero crossing of the signal $S_\phi^{\text{NO}}(\phi, \nu)$ in the range of the resonance frequency ν_0 is considered. Here it is assumed, that the dispersion part is zero at the resonance frequency ν_0:
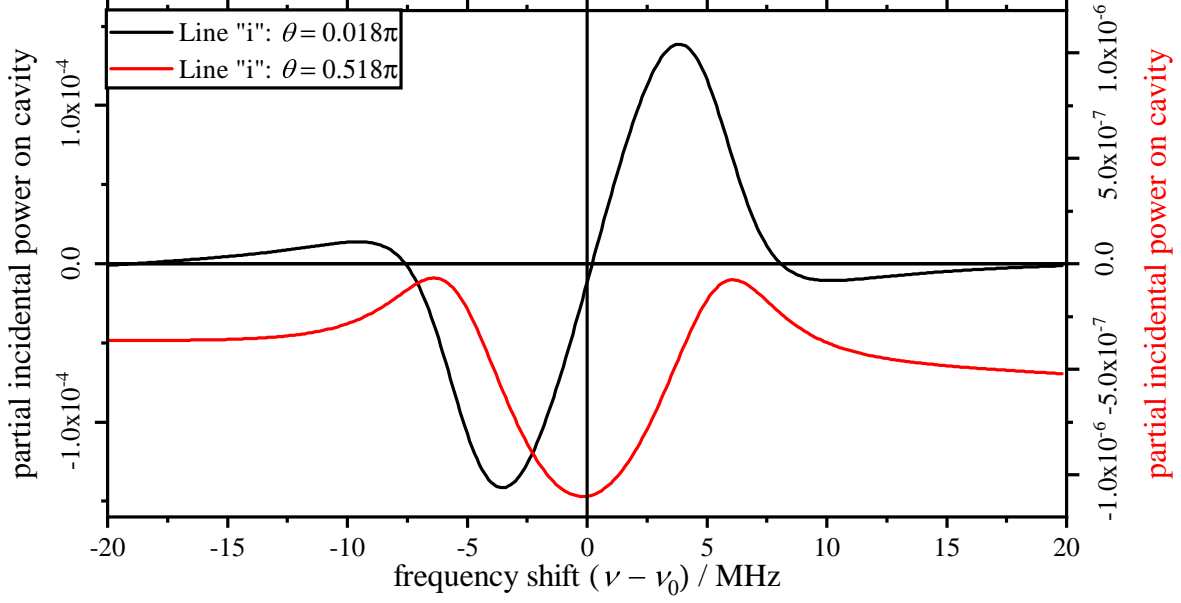
$$S_0(\nu = \nu_0) = 0 \tag{5.8}$$

Figure 5.29: Illustration of the possible offset and the associated frequency shift in the NICE-OHMS error signal of the iodine line P(33) 6-3 "i" due to the Doppler broadened background as a function of phase using a simulation. In each case, the error signal is plotted over a frequency shift for two phase positions shifted by $\pi/2$.

For the error signal with the phase error S_ϕ^{NO}, however, the zero crossing is shifted by the frequency $\Delta\nu$ due to a residual absorption component. This results in

$$S_\phi^{\text{NO}}(\phi, \nu_0 + \Delta\nu) = 0. \tag{5.9}$$

It follows from equations (5.7) and (5.9):

$$S_\phi(\phi, \Delta\nu) = \cos\phi \cdot S_0(\nu_0 + \Delta\nu) + \sin\phi \cdot S_{\frac{\pi}{2}}(\nu_0 + \Delta\nu) = 0 \tag{5.10}$$

In the next step, it is supposed that the absorption part is approximately constant $S_{\frac{\pi}{2}}(\nu_0 + \Delta\nu) \approx S_{\frac{\pi}{2}}(\nu_0)$ for small changes $\Delta\nu$ near the resonance frequency ν_0 and then a Taylor expansion around the resonant frequency ν_0 yields:

$$\cos\phi \cdot \frac{\partial S_0}{\partial \nu} \cdot \Delta\nu = -\sin\phi \cdot S_{\frac{\pi}{2}}(\nu_0). \tag{5.11}$$

Here $S_0(\nu_0) = 0$ is used and $\frac{\partial S_0}{\partial \nu}$ corresponds to the slope of the error signal $S_\phi^{\text{NO}}(\phi, \nu)$ in the area around of the resonant frequency ν_0. Simplified, it results:

$$\Delta\nu = -\tan\phi \cdot \frac{S_{\frac{\pi}{2}}(\nu_0)}{\frac{\partial S_0}{\partial \nu}}. \tag{5.12}$$

The simulation of the error signal in figure 5.29 results in a dispersive signal of $S_{\frac{\pi}{2}}(\nu_0) = -1.1 \cdot 10^{-6}$ and a slope of $\frac{\partial S_0}{\partial \nu} = 5.5 \cdot 10^{-5} \frac{1}{\text{MHz}}$. This results in a simulated frequency shift coefficient due to the phase of $\xi_{\text{phase,sim}} = 350\,\text{Hz}/°$.

To experimentally investigate the influence of the phase on the frequency, the phase of the NICE-OHMS is varied using an electronic phase shifter at the $f_{\text{mod}}^{\text{FSR}}$. The phase shift versus voltage of the phase shifter is determined by using the NICE-OHMS wm-error signal is maximum ($\Delta\phi = 0, \pi$) or zero ($\Delta\phi = \frac{\pi}{2}$). For different phase shifts the frequency deviation compared to an iodine stabilized He-Ne is measured over time. Figure 5.30 shows the frequency deviation plotted over the phase. The frequency at which the error signal is largest has been defined as position $\Delta\phi = 0°$ and $\Delta\nu = 0$.
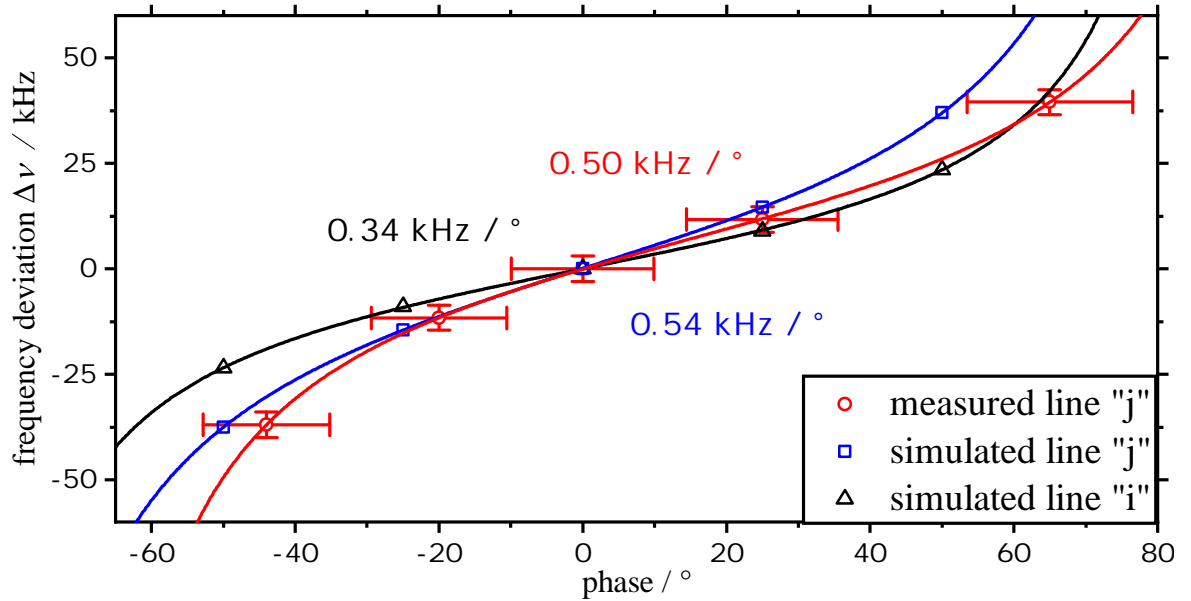
Figure 5.30: Measured and simulated frequency deviation of the light of the laser stabilized with wm-NICE-OHMS to the iodine line P(33) 6-3 "i" due to the phase setting in the NICE-OHMS signal with fit-function based on $\tan\phi$.

Using a fit-function based of equation (5.12) for the measured data of line "j", a phase shift sensitivity coefficient of $\xi_{\text{phase}} = 0.50\,\frac{\text{kHz}}{°}$ is obtained for small phase shifts. For comparison, the frequency deviation $\Delta\nu$ for the HFS lines "i" and "j" is simulated for different phases and is also shown in figure 5.30. Again the fit-function based of equation (5.12) is used for the measured data and for line "i" a simulated coefficient of $\xi_{\text{phase,"i"}} = 0.34\,\frac{\text{kHz}}{°}$ and for line "j" a coefficient of $\xi_{\text{phase,"j"}} = 0.54\,\frac{\text{kHz}}{°}$ is determined. The results of the simulation are comparable with the measured deviations. However, from the function fitted to the observed data, it is found that the phase set at the phase

shifter is shifted by about 14 °, which correspond to an offset of approx. 7 kHz. Thus readjusting of the phase can influence the frequency uncertainty of the stabilized laser system. When the phase change is estimated to a few degrees during a measurement, the frequency changes only by a few kHz (see equation (5.12)). Thus, the measured frequency instabilities of the NICE-OHMS stabilized diode laser cannot be explained by the phase changes investigated here.

5.3.6 Influence of Other Iodine Lines Next to P(33)6-3

In the frequency range of the Doppler broadened line P(33)6-3 other weaker molecular transitions of iodine exist, e.g. the line R(127)11-5, which is used for the stabilization of the He-Ne lasers. Other transitions include P(55)18-9, P(204)16-6, R(64)25-12, R(80)1-0, R(111)19-9, and R(182)17-7. Between the HFS components of the different lines and the P(33)6-3 transition there are frequency spacings of the order of the FSR used in this work and thus of the modulation frequency f_{FSR}. As a result, the dispersion ratio between the sidebands can be influenced and thus also the zero crossing in the error signal of the NICE-OHMS method, especially if narrow Lamb-dips are near the sideband frequencies. To investigate these effects, the frequency ν of the zero crossing in the error signal is determined for all HFS components of the line P(33)6-3 and compared to the unperturbed line center figure 5.31 (red). It is expected that the shift depends on the modulation frequency amplitude $\Delta\nu_{\text{wm}}^{\text{Lock}} = 6\,\text{MHz}$. To identify the influence of the Lamb-dips interaction with the sidebands, this simulation is repeated with the whole Doppler background but with only one single Lamb-dip (blue).

Particularly noticeable differences occur for the HFS lines number 6 ("p"), 9 ("m"), 10 ("l"), 11 ("k") and 19 ("c"). E.g. line P(33)6-3 "p" at ν_6, the frequency difference between the sideband $\nu_6 + f_{\text{FSR}}$ and the HFS component R(64)25-12 "k" is about 800 kHz and to component "g" of the line R(80)1-0 about 200 kHz and is thus substantially smaller than the width of the Lamb-dip (FWHM$\sim$ 6 MHz). The sideband $\nu_{19} - f_{\text{FSR}}$ of P(33)6-3 line "c" has a distance of about 30 kHz to HFS component "m" of line R(111)19-9. The sideband $\nu_{11} + f_{\text{FSR}}$ of the HFS component "k" of the P(33)6-3 line has a larger distance of about 1.2 MHz to the component "g" of the R(64)25-12 line, but the larger frequency offset of the zero crossing can be explained by the adjacent lines "m" and "l" of the P(33)6-3 line. These lines have a small frequency spacing of approx. 14 MHz
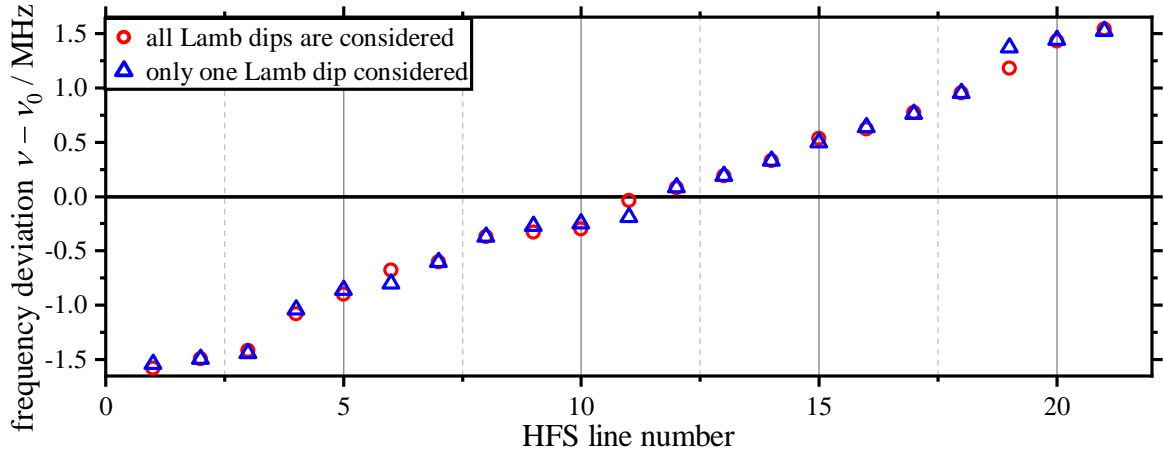
Figure 5.31: Simulated frequency deviation of the laser stabilized on all HFS components ("u"-"a") of the line P(33) 6-3 using the NICE-OHMS method compared to the resonance of the HFS component. In blue only one HFS component as one Lamb-dip on the hole Doppler background is simmulated, whereas in red all HFS components (all Lamb-dips) are taken into account.

and 8 MHz respectively, so that the error signals influence each other due to the line width.

For the frequency stability of the system, the influence from the Lamb-dips of the other lines should have no influence as long as they do not change over time, e.g. from variation of the power. However, both the Lamb-dips and the Doppler background have a significant influence on the frequency accuracy of the NICE-OHMS method and deviations up to 1.5 MHz from the resonance frequency ν_0 are possible. To minimize the influences a shorter cavity could be used so that the FSR becomes larger or the modulation frequency f_{FSR} is chosen in the order of twice the FSR so that the sidebands do not interact with these lines or the Doppler broadened background.

5.3.7 Intracavity Power

The dependence of the depth and width of the Lamb-dips on the saturation parameter can shift the frequency comparable an iodine stabilized He-Ne laser [98]. Thus the power shift coefficient ξ_{pow} for the employed resonator setup and the iodine cell is determined. The laser system is stabilized to the iodine line P(33) "j" using wm-NICE-OHMS and behind the resonator at the position of PD$_3$ see 5.1 the optical power

$P_{\text{cav,out}}$ is measured with a power meter, so that the power inside the cavity P_{cav} can be determined by equation (5.13):

$$P_{\text{cav}} = T_{\text{M}_2} \cdot \frac{1}{K_{\text{PBS}}} \cdot P_{\text{cav,out}}. \tag{5.13}$$

Here K_{PBS} is the splitting factor of the combination of $\lambda/2$-plate and polarizing beam splitter.

To vary the power inside the resonator, the optical power in front of the cavity $P_{\text{cav,in}}$ is changed. This power change is controlled by the AOM by changing the applied RF power. The beat frequency between the comb and the diode laser is measured and every 60 s the optical power in front of the cavity is changed between two fixed values. Care is taken that the power does not vary too much in order to reduce the influence of the optical power change on the detectors of the NICE-OHMS stabilization. Figure 5.32 shows the deviation of the absolute frequency from the CIPM frequency of line "j" $\nu - \nu_0$ plotted against time. At the same time, the optical power within the cavity calculated according to equation (5.13) is plotted.
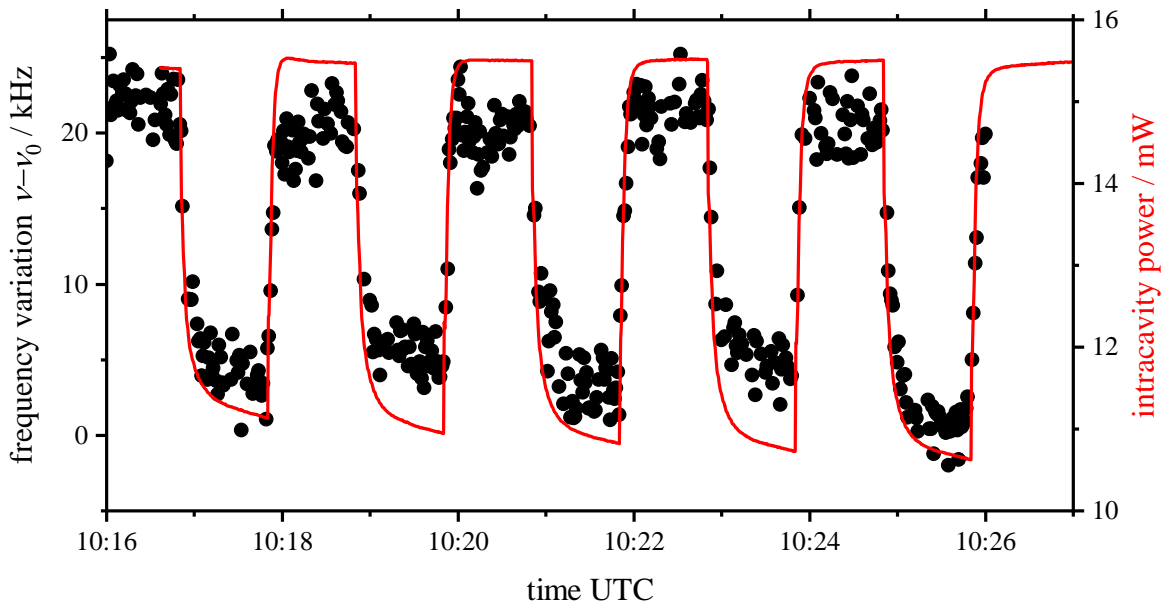
Figure 5.32: Frequency variation $\Delta\nu$ of the NICE-OHMS stabilized laser and corresponding intracavity power.

The power shift coefficient of $\xi_{\text{pow}} = (3.8 \pm 0.5) \frac{\text{kHz}}{\text{mW}}$ is determined from the average values of the frequency between 15 mW and 11 mW. It must be taken into account that the coefficient determined here can only be assumed to be approximately linear in the environment at an intracavity power of approx. 13 mW. As described in chapter 2.2.1,

the value corresponds to a saturation parameter of $S = 1.26$ and non-linear effects can change the sensitivity at other powers. For intracavity power jumps of around 10 mW ($P_{\text{cav,in}} \approx 15\,\text{mW} \rightarrow 5\,\text{mW}$) the coefficient is $\xi_{\text{pow}} = (6.0 \pm 0.3)\,\frac{\text{kHz}}{\text{mW}}$. For jumps of around 14 mW ($P_{\text{cav,in}} \approx 15\,\text{mW} \rightarrow 1\,\text{mW}$) the coefficient is much larger ($\sim 60\,\frac{\text{kHz}}{\text{mW}}$). In the last comparison, however, it must be considered that the power in the cavity becomes so low that the transition is only slightly saturated. The Lamb-dips are therefore only very weak and the entire stabilization system no longer works reliably and is very sensitive to offsets.

Figure 5.33 shows the comparison between the observed frequency deviation ($\nu_{\text{DL}} - \nu_0$) of the diode laser light (blue) and the calculated deviation $\Delta\nu_{\text{pow}}$ due to intracavity power fluctuations (red) over time using a power shift coefficient $\xi_{\text{pow}} = (3.8 \pm 0.5)\,\frac{\text{kHz}}{\text{mW}}$.
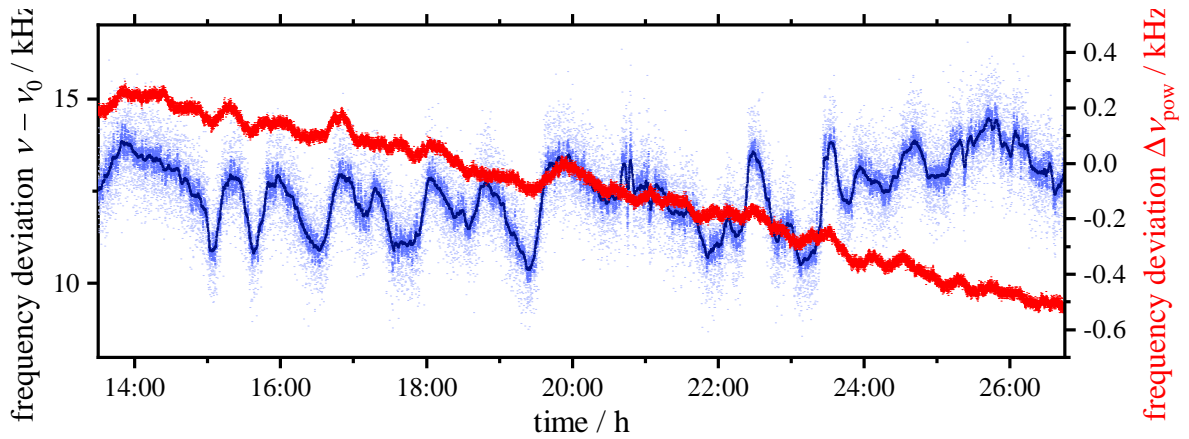
Figure 5.33: Frequency measurement of the diode laser stabilized with NICE-OHMS to the iodine line P(33) 6-3 "j" over time in comparison to the calculated frequency fluctuations from power within the cavity using a coefficient $\xi_{\text{pow}} = (3.8 \pm 0.5)\,\frac{\text{kHz}}{\text{mW}}$. In the light blue, an averaging time of 1 s is shown, whereas in the darker blue shades, averaging is done over 10 s and 100 s.

Based on the measured power the frequency fluctuations are calculated (with $\xi_{\text{pow}} = (3.83 \pm 0.51)\,\frac{\text{kHz}}{\text{mW}}$) and appear much smaller than the observed frequency fluctuations. In addition, the slow frequency drift due to the power decreasing over time can not be detected in the measured frequency of the laser. Therefore, it is concluded that these power changes are not the cause of the frequency fluctuations. Nevertheless correlation on shorter timescales between the intracavity power and the frequency can be seen. This indicates possible etalon effects within the optical path in front of or behind the cavity, because the fluctuations of the frequency and the power occur with the same

phase. Any disturbing etalon would lead to a sinusoidal variation of the frequency and also to a transmission through that etalon as a function of the round-trip phase in this etalon. This phase itself depends via the optical path length on temperature and air pressure. This dependence can be seen in figure 5.18, since the frequency of the observed oscillations is approximately proportional to the rate of temperature change.

5.4 Summary of Experimental Results

	exp. value	sim. value
modulation amplitude $\xi_{\text{mod}}^{\text{Lock}}$	$-12.3 \pm 0.9 \, \frac{\text{kHz}}{\text{MHz}}$	$8.8 \pm 0.4 \, \frac{\text{kHz}}{\text{MHz}}$
modualtion frequency NO $\xi_{\text{mod}}^{\text{FSR}}$	$49.6 \pm 6.1 \, \frac{\text{kHz}}{\text{MHz}}$	$-3.6 \, \frac{\text{kHz}}{\text{MHz}}$
phase ξ_{phase}	$0.50 \, \frac{\text{kHz}}{\circ}$	$0.54 \, \frac{\text{kHz}}{\circ}$
RAM ξ_{RAM}	$0.65 \pm 0.04 \, \frac{\text{kHz}}{\text{mV}}$	-
intracavity power:		
$\quad \xi_{\text{pow}}$ ($15\,\text{mW} \rightarrow 11\,\text{mW}$)	$3.8 \pm 0.5 \, \frac{\text{kHz}}{\text{mW}}$	-
$\quad \xi_{\text{pow}}$ ($15\,\text{mW} \rightarrow 5\,\text{mW}$)	$6.0 \pm 0.3 \, \frac{\text{kHz}}{\text{mW}}$	-
iodine cell parameter [4]:		
$\quad$ wall-temperature	$0.5 \, \frac{\text{kHz}}{\circ\text{C}}$	-
$\quad$ cold-finger temperature	$-15.0 \, \frac{\text{kHz}}{\circ\text{C}}$	-

Table 5.2: Experimentally determined and simulated frequency shift coefficient ξ of the NICE-OHMS method for different systematic effects.

A summary of the various frequency-sensitive parameters that were investigated in the previous sections are summarized in table 5.2 and compared with the simulations. If this sensitivity parameters are considered, it is now clear, that the variations of the environmental and the experimental parameters cannot explain the observed frequency fluctuations.

Despite many built-in isolators, integrated AOM and slightly misaligned optics to prevent back-coupling, the etalon effects mentioned above could not be further reduced. However, it was found that a tight enclosure around the entire setup minimizes influences from the environment in the form of air drafts and pressure changes on the frequency. Depending on day to day performance, the DL Pro could be stabilized up to a maximum of two to three days before the laser fell out of lock due to the limited stable tuning range of the laser diode.

Chapter 6

Conclusion and Outlook

In this thesis, two types of diode lasers stabilized on iodine were investigated to replace helium-neon lasers at a wavelength of 633 nm. One is the "Toptica beta demonstrator" (TBD) as field use system, where the stabilization is based on Doppler broadened spectroscopy, which is intended to replace simple stabilized lasers with 10-MHz-accuracy used in industry, and the other one a high-end system, which is stabilized with the NICE-OHMS method.

The shoe box size TBD laser system achieves a frequency instability of $2 \cdot 10^{-10}$ at an averaging time of 1 s, depending on the selected iodine line. Compared to two-modes- or Zeeman-stabilized He-Ne lasers, it shows a similar instability. The comparison of the measured absolute frequencies of the TBD with the simulated transmission spectra of iodine allows a prediction of the frequency with an accuracy of $\sim 10\,\mathrm{MHz}$. On the basis of the curvature and intensity of the simulated absorption lines of iodine, the theoretical instability of the TBD can also be estimated, which was about a factor of 10 larger than the one observed. With these results, the small size and an optical output power around 5 mW the TBD represents a suitable modern alternative to Zeeman or two-mode stabilized He-Ne lasers at a wavelength of 633 nm.

The diode laser stabilized to Doppler-free hyperfine components of iodine transitions using the NICE-OHMS method is a promising way to replace iodine stabilized He-Ne lasers as a practical realization of the meter. The advantage of stabilizing diode lasers with the NICE-OHMS method over pure saturation spectroscopy is the external cavity. By means of the cavity, higher intensities and long effective absorption length, which are required for the saturation of iodine, can be achieved with smaller iodine cells and less optical power. Likewise, the possible smaller iodine cells can also enable a more compact design. A frequency instability of $1.2 \cdot 10^{-12}$ at an averaging time of 1 s could be demonstrated in this thesis which is four times better than

that of iodine stabilized He-Ne laser and diode lasers previously stabilized with saturated spectroscopy. However, for longer averaging times above 100 s, the observed instability becomes larger than that of an iodine stabilized He-Ne laser. The mean measured frequency of the laser stabilized on the HFS component "j" of the P(33)6-3 line is $\bar{\nu}_{\text{abs}} = 473\,611\,473\,817(28)\,\text{kHz}$ and agrees within the uncertainty with the value recommended by the International Committee for Weights and Measures (CIPM) for the realization of the meter. Although the observed uncertainty of the NICE-OHMS system is comparable to previous diode laser systems, it is nevertheless worse than iodine stabilized He-Ne lasers (10 kHz).

In order to analyze frequency influences, investigations by experimental methods as well as simulations of the sensitive experimental parameters were determined. No single direct cause for the instabilities for larger averaging times and the unprecise reproducibility of the frequency could be found. However, periodic frequency variations under a linear change of e.g. the temperature, points to influences of disturbing etalons in the optical pathway in front of or behind the cavity. Despite excessive use of isolators and an acousto optical modulator the influence of the etalons could not be further reduced. Additionally, the experimental and simulated results also show that the wide Doppler background can influence the stability, by shifting the phase relationship between the carrier and sidebands needed for detection in the NICE-OHMS method due to the dispersion changes that occur from other HFS components.

In conclusion, due to the demonstrated short time frequency instability, the uncertainty on a similar level, the flexibility of the adjusted frequency, the higher output power of the laser and the possible compact design, a diode laser stabilized with the NICE-OHMS method on iodine might still present an alternative to iodine stabilized He-Ne laser as a practical realization of the meter at the wavelength of 633 nm. However, two main problems for the realization were identified. First, the etalon effects occurring in the optical path and the broad Doppler background due to the many hyperfine components of a transition of iodine.

These problems could be addressed by redesigning the experiment as follows. To minimize the etalon effects, additional isolators could be used and special consideration could be given to the alignment of the optical components so that interfering reflections are not in the beam path. Additionally etalon-immune distances could be used to reduce the influences of the etalon effect [99]. A cavity with a smaller mirror spacing could be used, so that the free spectral range (FSR) becomes larger and the sidebands needed for the NICE-OHMS have a larger frequency spacing than the width of the

Doppler background. This can minimize possible influences of the Doppler background dispersion on the error signal. Likewise, by choosing twice the FSR frequency for the sidebands at the current cavity length so that the sidebands are resonant with the 2nd adjacent mode, this problem could be minimized. With these improvements and the results shown in this thesis, it should be possible to establish a diode laser stabilized by the NICE-OHMS method on iodine as a practical realization of the meter at 633 nm.

Bibliography

[1] H. Schnatz, "Länge - die si-basiseinheit meter," *PTB-Mitteilungen*, vol. 122, no. 1, pp. 7–22, 2012.

[2] d. B. d. L. L'Ecole Polytechnique, ed., *Comptes Rendus des séances de la 1er CGPM 1889*, (Quai des Grands-Augustins, 55, France), Gauthier-Villars et Fils, 1890.

[3] H. Barrell, "The metre," *Contemp. Phys.*, vol. 3, no. 6, pp. 415–434, 1962.

[4] T. J. Quinn, "Practical realization of the definition of the metre, including recommended radiations of other optical frequency standards (2001)," *Metrologia*, vol. 40, pp. 103–133, 2003.

[5] T. J. Quinn, "Mise en pratique of the definition of the Metre (1992)," *Metrologia*, vol. 30, pp. 523–541, 1993/94.

[6] Bureau International des Poids et Mesures, "Le Système international d'unités / The International System of Units," Pavillon de Breteuil, F-92310 Sèvres, France, 2019. 9th edition 2019.

[7] G. R. Hanes and K. M. Baird, "I_2 controlled he-ne laser at 633 nm: Preliminary wavelength," *Metrologia*, vol. 5, pp. 32–33, 1969.

[8] G. R. Hanes, K. M. Baird, and J. DeRemiglis, "Stability, reproducibility and absolute wavelength of a 633-nm He-Ne laser stabilized to an iodine hyperfine component," *Appl. Opt.*, vol. 12, pp. 1600–1605, 1973.

[9] A. Lassila, K. Riski, J. Hu, T. Ahola, S. Naicheng, L. Chengyang, P. Balling, J. Blabla, L. Abramova, Y. G. Zakharenko, V. L. Fedorin, A. Chartier, and J.-M. Chartier, "International comparison of He-Ne lasers stabilized with $^{127}I_2$ at $\lambda \approx 633$ nm," *Metrologia*, vol. 37, pp. 701–707, 2000.

[10] J. E. Decker, R. Schödel, and G. Bönsch, "Next-generation Kösters interferometer," in *Recent Developments in Traceable Dimensional Measurements II* (J. E. Decker and N. Brown, eds.), vol. 5190, pp. 14–23, International Society for Optics and Photonics, SPIE, 2003.

[11] G. Jäger, E. Manske, T. Hausotte, A. Müller, and F. Balzer, "Nanopositioning and nanomeasuring machine NPMM-200—a new powerful tool for large-range micro- and nanotechnology," *Surface Topography: Metrology and Properties*, vol. 4, p. 034004, jul 2016.

[12] F. Träger, *Springer Handbook of Lasers and Optics*. Springer, Berlin, Heidelberg, 2012.

[13] BIPM, "Recommended values of standard frequencies." online at https://www.bipm.org/en/publications/mises-en-pratique/standard-frequencies.html, Page last updated: 30 November 2018.

[14] E. J. Zang, T. Kasahara, K. Sakamoto, H. Inaba, Y. Akimoto, X. Chen, N.-C. Shen, and Y. Wang, "External-cavity diode lasers and laser saturation spectroscopy of iodine hyperfine structure near 633 nm," in *1999 International Conference on Industrial Lasers* (F. Gan, H. Weber, Z. Li, and Q. Chen, eds.), vol. 3862, pp. 282 – 286, International Society for Optics and Photonics, SPIE, 1999.

[15] W. Gawlik and J. Zachorowski, "Stabilization of diode-laser frequency to atomic transitions," *Optica Applicata*, vol. 34, pp. 607–618, 2004.

[16] M. Vainio, M. Merimaa, and E. Ikonen, "Iodine spectrometer based on a 633 nm transmission-grating diode laser," *Meas. Sci. Technol.*, vol. 16, no. 6, p. 1305, 2005.

[17] A. Zarka, A. Abou-Zeid, D. Chagniot, J.-M. Chartier, O. Cip, J. Cliche, C. S. Edwards, F. Imkenberg, P. Jedlicka, B. Kabel, A. Lassila, J. Lazar, M. Merimaa, Y. Millerioux, H. Simonsen, M. Têtu, and J.-P. Wallerand, "International comparison of eight semiconductor lasers stabilized on $^{127}I_2$ at $\lambda = 633$ nm," *Metrologia*, vol. 37, no. 4, p. 329, 2000.

[18] G. Blume, D. Jedrzejczyk, J. Pohl, D. Feise, A. Sahm, N. Werner, C. Nölleke, P. Leisching, and K. Paschke, "633-nm single-mode master-oscillator power-

amplifier module," in *Optical Components and Materials XV* (S. Jiang and M. J. F. Digonnet, eds.), vol. 10528, pp. 41 – 51, International Society for Optics and Photonics, SPIE, 2018.

[19] C. Nölleke, P. Leisching, G. Blume, D. Jedrzejczyk, J. Pohl, D. Feise, A. Sahm, and K. Paschke, "Frequency locking of compact laser-diode modules at 633 nm," in *Photonic Instrumentation Engineering V* (Y. G. Soskind, ed.), vol. 10539 of *Proc. SPIE*, pp. 28–33, International Society for Optics and Photonics, SPIE, 2018.

[20] J. Ye, L.-S. Ma, and J. L. Hall, "Sub-Doppler optical frequency reference at 1.064 μm by means of ultrasensitive cavity-enhanced frequency modulation spectroscopy of a C_2HD overtone transition," *Opt. Lett.*, vol. 21, pp. 1000–1002, 1996.

[21] J. Ye, L.-S. Ma, and J. L. Hall, "Ultrasensitive detections in atomic and molecular physics: demonstration in molecular overtone spectroscopy," *J. Opt. Soc. Am. B*, vol. 15, pp. 6–15, 1998.

[22] J. Ye, L.-S. Ma, and J. L. Hall, "High-resolution frequency standard at 1030 nm for Yb:YAG solid-state lasers," *J. Opt. Soc. Am. B*, vol. 17, pp. 927–931, Jun 2000.

[23] A. Foltynowicz, F. Schmidt, W. Ma, and O. Axner, "Noise-immune cavity-enhanced optical heterodyne molecular spectroscopy: Current status and future potential," *Appl. Phys. B*, vol. 92, no. 3, pp. 313–326, 2008.

[24] W. M. Haynes, ed., *CRC Handbook of Chemistry and Physics 96th Edition*. CRC Press, Taylor & Francis Group, 2015.

[25] W. Demtröder, *Molecular Physics: Theoretical Principles and Experimental Methods.* Wiley, 2008. ISBN: 978-3-527-61810-1.

[26] M. Gläser, "Hyperfine components of iodine for optical frequency standards," PTB–Bericht Opt-25, Physikalisch–Technische Bundesanstalt, Braunschweig, 1987.

[27] M. D. Levenson and A. L. Schawlow, "Hyperfine interactions in molecular iodine," *Phys. Rev. A*, vol. 6, pp. 10–20, Jul 1972.

[28] S. Gerstenkorn and P. Luc, "Absolute iodine (I_2) standards measured by means of Fourier transform spectroscopy," *Revue de Physique Apliquée*, vol. 14, pp. 791–794, 1979.

[29] P. Luc, "Molecular constants and Dunham expansion parameters describing the B-X system of the iodine molecule," *J. Mol. Spectrosc.*, vol. 80, no. 1, pp. 41–55, 1980.

[30] J. Tellinghuisen, "Intensity factors for the I_2 B-X band system," *J. Quant. Spectrosc. Radiat. Transfer*, vol. 19, no. 2, pp. 149–161, 1978.

[31] M. Kroll, "Hyperfine structure in the visible molecular-iodine absorption spectrum," *Phys. Rev. Lett.*, vol. 23, pp. 631–633, Sep 1969.

[32] M. Kroll and K. Innes, "Molecular electronic spectroscopy by Fabry-Perot interferometry. effect of nuclear quadrupole interactions on the line widths of the $B^3\Pi_0^+ - X^1\Sigma_g^+$ transition of the I_2 molecule," *J. Mol. Spectrosc.*, vol. 36, no. 2, pp. 295–309, 1970.

[33] B. Bodermann, H. Knöckel, and E. Tiemann, *Basics and usage of the program Iodine Spectrum*, 1999.

[34] B. Bodermann, H. Knöckel, and E. Tiemann, "Widely usable interpolation formulae for hyperfine splittings in the $^{127}I_2$ spectrum," *Eur. Phys. J. D*, vol. 19, pp. 31–44, 2002.

[35] H. Knöckel, B. Bodermann, and E. Tiemann, "High precision description of the rovibronic structure of the I_2 B–X spectrum," *Eur. Phys. J. D*, vol. 28, pp. 199–209, 2004.

[36] R. Honig and H. Hook, "Vapor pressure data for some common gases," *RCA Rev.*, vol. 21, pp. 360–368, September 1960.

[37] G. W. Thomson, "The Antoine equation for vapor-pressure data.," *Chemical Reviews*, vol. 38, no. 1, pp. 1–39, 1946.

[38] L. J. Gillespie and L. H. D. Fraser, "The normal vapor pressure of crystalline iodine," *Journal of the American Chemical Society*, vol. 58, no. 11, pp. 2260–2263, 1936.

[39] W. Demtröder, *Laser Spectroscopy 1*, vol. 1. Berlin, Heidelberg: Springer, 5 ed., 2014.

[40] P. Siddons, C. S. Adams, and I. G. Hughes, "Off-resonance absorption and dispersion in vapours of hot alkali-metal atoms," *J. Phys. B: At. Mol. Phys.*, vol. 42, p. 175004, aug 2009.

[41] W. Demtröder, *Laser Spectroscopy 2*. Berlin, Heidelberg: Springer, 5 ed., 2015.

[42] K. C. Shotton and G. D. Chapman, "Lifetimes of $^{127}I_2$ molecules excited by the 632.8 nm He/Ne laser," *J. Chem. Phys.*, vol. 56, no. 2, pp. 1012–1013, 1972.

[43] A. Brillet and P. Cerez, "Quantitative description of the saturated absorption signal in iodine stabilized He-Ne lasers," *Metrologia*, vol. 13, no. 3, p. 137, 1977.

[44] P. Cerez, A. Brillet, S. Hajdukovic, and N. Man, "Iodine stabilized He-Ne laser with a hot wall iodine cell," *Opt. Commun.*, vol. 21, no. 3, pp. 332–336, 1977.

[45] T. W. Hänsch, M. D. Levenson, and A. L. Schawlow, "Complete hyperfine structure of a molecular iodine line," *Phys. Rev. Lett.*, vol. 26, pp. 946–949, Apr 1971.

[46] S. Doeleman, T. Mai, A. E. E. Rogers, J. G. Hartnett, M. E. Tobar, and N. Nand, "Adapting a cryogenic sapphire oscillator for very long baseline interferometry," *Publ. Astron. Soc. Pac.*, vol. 123, pp. 582–595, 2011.

[47] B. W. Fowler and C. C. Sung, "Doppler and collision-broadening effects in the profile of spectral lines," *J. Opt. Soc. Am.*, vol. 65, pp. 949–951, Aug 1975.

[48] A. K. Hui, B. H. Armstrong, and A. A. Wray, "Rapid computation of the Voigt and complex error functions," *J. Quant. Spectrosc. Radiat. Transfer*, vol. 19, pp. 509 – 516, 1978.

[49] J. M. Supplee, E. E. Whittaker, and W. Lenth, "Theoretical description of frequency modulation and wavelength modulation spectroscopy," *Appl. Opt.*, vol. 33, pp. 6294–6302, 1994.

[50] G. C. Bjorklund, M. D. Levenson, W. Lenth, and C. Ortiz, "Frequency modulation (FM) spectroscopy: Theory of lineshapes and signal-to-noise analysis," *Appl. Phys. B*, vol. 32, pp. 145–152, 1983.

[51] G. C. Bjorklund, "Frequency-modulation spectroscopy: a new method for measuring weak absorptions and dispersions," *Opt. Lett.*, vol. 5, pp. 15–17, 1980.

[52] D. Meschede, *Optik, Licht und Laser.* Teubner Studienbücher, 1999.

[53] H. J. Eichler and J. Eichler, *Laser - Bauformen, Strahlführung, Anwendungen.* Springer Vieweg, Berlin, Heidelberg, 2015.

[54] L. Gianfrani, R. W. Fox, and L. Hollberg, "Cavity-enhanced absorption spectroscopy of molecular oxygen," *J. Opt. Soc. Am. B*, vol. 16, pp. 2247–2254, Dec 1999.

[55] E. D. Black, "An introduction to Pound-Drever-Hall laser frequency stabilization," *Am. J. Phys.*, vol. 69, pp. 79–87, 2001.

[56] R. W. P. Drever, J. L. Hall, F. V. Kowalski, J. Hough, G. M. Ford, A. J. Munley, and H. Ward, "Laser phase and frequency stabilization using an optical resonator," *Appl. Phys. B*, vol. 31, pp. 97–105, 1983.

[57] J. Ye, L.-S. Ma, and J. L. Hall, "Cavity-enhanced frequency modulation spectroscopy: Advancing optical detection sensitivity and laser frequency stabilization," *Proc. SPIE*, vol. 3270, p. 85, 1998.

[58] L.-S. Ma, J. Ye, P. Dubé, and J. L. Hall, "Ultrasensitive frequency-modulation spectroscopy enhanced by a high-finesse optical cavity: theory and application to overtone transitions of C_2H_2 and C_2HD," *J. Opt. Soc. Am. B*, vol. 16, pp. 2255–2268, Dec 1999.

[59] O. Axner, W. Ma, and A. Foltynowicz, "Sub-Doppler dispersion and noise-immune cavity-enhanced optical heterodyne molecular spectroscopy revised," *J. Opt. Soc. Am. B*, vol. 25, pp. 1166–1177, Jul 2008.

[60] O. Axner, P. Ehlers, A. Foltynowicz, I. Silander, and J. Wang, *NICE-OHMS—Frequency Modulation Cavity-Enhanced Spectroscopy—Principles and Performance*, pp. 211–251. Berlin, Heidelberg: Springer Berlin Heidelberg, 2014.

[61] C. Ishibashi and H. Sasada, "Highly sensitive cavity-enhanced sub-Doppler spectroscopy of a molecular overtone band with a 1.66 μm tunable diode laser," *Jpn. J. Appl. Phys.*, vol. 38, pp. 920–922, feb 1999.

[62] C. Ishibashi and H. Sasada, "Near-infrared laser spectrometer with sub-Doppler resolution, high sensitivity, and wide tunability: A case study in the 1.65-μm region of CH$_3$I spectrum," *J. Mol. Spectrosc.*, vol. 200, no. 1, pp. 147–149, 2000.

[63] M. S. Taubman, T. L. Myers, B. D. Cannon, and R. M. Williams, "Stabilization, injection and control of quantum cascade lasers, and their application to chemical sensing in the infrared," *Spectrochimica Acta Part A: Molecular and Biomolecular Spectroscopy*, vol. 60, no. 14, pp. 3457–3468, 2004.

[64] F. M. Schmidt, A. Foltynowicz, W. Ma, and O. Axner, "Fiber-laser-based noise-immune cavity-enhanced optical heterodyne molecular spectrometry for Doppler-broadened detection of C$_2$H$_2$ in the parts per trillion range," *J. Opt. Soc. Am. B*, vol. 24, pp. 1392–1405, Jun 2007.

[65] A. Foltynowicz, W. Ma, and O. Axner, "Characterization of fiber-laser-based sub-Doppler NICE-OHMS for quantitative trace gas detection," *Opt. Express*, vol. 16, pp. 14689–14702, Sep 2008.

[66] J. Hu, E. Ikonen, and K. Riski, "On the nth harmonic locking of the iodine stabilized He-Ne laser," *Opt. Commun.*, vol. 120, pp. 65–70, 1995.

[67] F. Riehle, *Frequency Standards: Basics and Applications*. Weinheim: Wiley-VCH, 2004.

[68] A. J. Wallard, "Frequency stabilization of the helium-neon laser by saturated absorption in iodine vapour," *Journal of Physics Electron.*, vol. 5, pp. 926–930, 1972.

[69] J.-M. Chartier, L. Robertsson, M. Sommer, J. Tschirnich, V. Navratil, R. Gata, B. Pucek, J. Blabla, J. Smydke, M. Ziegler, V. Zeleny, F. Petru, Z. . V. K. Tomanyiczka, E. Banreti, Y. G. Zakharenko, and L. F. Vitushkin, "International comparison of iodine-stabilized helium-neon lasers at $\lambda = 633$ nm involving seven laboratories," *Metrologia*, vol. 28, pp. 19–25, 1991.

[70] E. Benkler, B. Lipphardt, T. Puppe, R. Wilk, F. Rohde, and U. Sterr, "End-to-end topology for fiber comb based optical frequency transfer at the 10^{-21} level," *Opt. Express*, vol. 27, pp. 36886–36902, dec 2019. also see erratum: [100].

[71] R. Holzwarth, T. Udem, T. W. Hänsch, J. C. Knight, W. J. Wadsworth, and P. S. J. Russell, "Optical frequency synthesizer for precision spectroscopy," *Phys. Rev. Lett.*, vol. 85, pp. 2264–2267, 2000.

[72] S. Weyers, V. Gerginov, M. Kazda, J. Rahm, B. Lipphardt, G. Dobrev, and K. Gibble, "Advances in the accuracy, stability, and reliability of the PTB primary fountain clocks," *Metrologia*, vol. 55, no. 6, pp. 789–805, 2018.

[73] R. Schwarz, S. Dörscher, A. Al-Masoudi, E. Benkler, T. Legero, U. Sterr, S. Weyers, J. Rahm, B. Lipphardt, and C. Lisdat, "Long term measurement of the ^{87}Sr clock frequency at the limit of primary Cs clocks," *Phys. Rev. Research*, vol. 2, p. 033242, Aug 2020.

[74] C. Grebing, A. Al-Masoudi, S. Dörscher, S. Häfner, V. Gerginov, S. Weyers, B. Lipphardt, F. Riehle, U. Sterr, and C. Lisdat, "Realization of a timescale with an accurate optical lattice clock," *Optica*, vol. 3, pp. 563–569, 2016.

[75] E. Benkler, C. Lisdat, and U. Sterr, "On the relation between uncertainties of weighted frequency averages and the various types of allan deviations," *Metrologia*, vol. 52, p. 565, 2015.

[76] D. W. Allan, "Statistics of atomic frequency standards," *Proc. IEEE*, vol. 54, pp. 221–230, 1966.

[77] J. A. Barnes, A. R. Chi, L. S. Cutler, D. J. Healey, D. B. Leeson, T. E. McGunigal, J. A. Mullan, W. L. Smith, R. L. Sydnor, R. F. C. Vessot, and G. M. R. Winkler, "Characterization of frequency stability," *IEEE Trans. Instrum. Meas.*, vol. IM-20, pp. 105–120, 1971. see corrections in NIST TN-1337 [101].

[78] D. W. Allan and J. Barnes, "A modified "Allan variance" with increased oscillator characterization ability," in *Proceedings of the 35th Ann. Freq. Control Symposium*, (Ft. Monmouth, NJ 07703), pp. 470–475, Electronic Industries Association, May 1981. For corrections see [101].

[79] S. T. Dawkins, J. J. McFerran, and A. N. Luiten, "Considerations on the measurement of the stability of oscillators with frequency counters," *IEEE Trans. Ultrason. Ferroelectr. Freq. Control*, vol. 54, pp. 918–925, 2007.

[80] F. Krause, E. Benkler, C. Nölleke, P. Leisching, and U. Sterr, "Simple and compact diode laser system stabilized to Doppler-broadened iodine lines at 633 nm," *Appl. Opt.*, vol. 59, pp. 10808–10812, Dec 2020.

[81] U. Tietze and C. Schenk, *Halbleiter-Schaltungstechnik*, vol. 11. Springer Verlag Berlin Heidelberg, 1999.

[82] C. S. Edwards, G. P. Barwood, P. Gill, and W. R. C. Rowley, "A 633 nm iodine-stabilized diode-laser frequency standard," *Metrologia*, vol. 36, no. 1, p. 41, 1999.

[83] P. E. Ciddor and R. M. Duffy, "Two-mode frequency-stabilised He-Ne (633 nm) lasers: studies of short- and long-term stability," *Journal of Physics E: Scientific Instruments*, vol. 16, pp. 1223–1227, dec 1983.

[84] W. R. C. Rowley, "The performance of a longitudinal Zeeman-stabilised He-Ne laser (633 nm) with thermal modulation and control," *Measurement Science and Technology*, vol. 1, pp. 348–351, apr 1990.

[85] C. Affolderbach and G. Mileti, "A compact laser head with high-frequency stability for Rb atomic clocks and optical instrumentation," *Rev. Sci. Instrum.*, vol. 76, no. 7, p. 073108, 2005.

[86] Y. M. Blanter and M. Büttiker, "Shot noise in mesoscopic conductors," *Physics Reports*, vol. 336, no. 1, pp. 1–166, 2000.

[87] D. A. Van Baak and G. Herold, "Response of a lock-in amplifier to noise," *Am. J. Phys.*, vol. 82, no. 8, pp. 785–797, 2014.

[88] I. H. Malitson, "Interspecimen comparison of the refractive index of fused silica," *J. Opt. Soc. Am.*, vol. 55, pp. 1205–1209, 1965.

[89] A. Yariv, *Quantum Electronics.* New York, Oxford: Wiley, third ed., 1989.

[90] D. Walsh, "Nonlinear optics: KTP fiber-coupled phase modulators advance atom interferometry." online at https://www.laserfocusworld.com/test-measurement/test-measurement/article/16547015/nonlinear-optics-ktp-fibercoupled-phase-modulators-advance-atom-interferometry, Page last updated: 11 July 2016.

[91] J. F. Diehl, C. E. Sunderman, J. M. Singley, V. J. Urick, and K. J. Williams, "Control of residual amplitude modulation in lithium niobate phase modulators," *Opt. Express*, vol. 25, pp. 32985–32994, Dec 2017.

[92] J. D. Bierlein, A. Ferretti, L. H. Brixner, and W. Y. Hsu, "Fabrication and characterization of optical waveguides in $KTiOPO_4$," *Appl. Phys. Lett.*, vol. 50, no. 18, pp. 1216–1218, 1987.

[93] A. Razet, J. Gagnière, and P. Juncar, "Hyperfine structure analysis of the 33P (6-3) line of $^{127}I_2$ at 633 nm using a continuous-wave tunable dye laser," *Metrologia*, vol. 30, pp. 61–65, jan 1993.

[94] E. A. Whittaker, M. Gehrtz, and G. C. Bjorklund, "Residual amplitude modulation in laser-optic phase modulation," *J. Opt. Soc. Am. B*, vol. 2, pp. 1320 – 1326, 1985.

[95] A. Foltynowicz, I. Silander, and O. Axner, "Reduction of background signals in fiber-based NICE-OHMS," *J. Opt. Soc. Am. B*, vol. 28, pp. 2797–2805, 2011.

[96] N. C. Wong and J. L. Hall, "Servo control of amplitude modulation in frequency-modulation spectroscopy: demonstration of shot-noise-limited detection," *J. Opt. Soc. Am. B*, vol. 2, pp. 1527–1533, 1985.

[97] R. G. DeVoe and R. G. Brewer, "Laser-frequency division and stabilization," *Phys. Rev. A*, vol. 30, pp. 2827–2829, Nov 1984.

[98] J. Hu, T. Ahola, E. Ikonen, and K. Riski, "Frequency shifts of iodine stabilized He-Ne lasers at higher harmonic order stabilization," *IEEE Trans. Instrum. Meas.*, vol. 46, no. 2, pp. 186–190, 1997.

[99] P. Ehlers, A. C. Johansson, I. Silander, A. Foltynowicz, and O. Axner, "Use of etalon-immune distances to reduce the influence of background signals in frequency-modulation spectroscopy and noise-immune cavity-enhanced optical heterodyne molecular spectroscopy," *J. Opt. Soc. Am. B*, vol. 31, pp. 2938–2945, Dec 2014.

[100] E. Benkler, B. Lipphardt, T. Puppe, R. Wilk, F. Rohde, and U. Sterr, "End-to-end topology for fiber comb based optical frequency transfer at the 10^{-21} level: erratum," *Opt. Express*, vol. 28, no. 10, pp. 15023–15024, 2020.

[101] D. Sullivan, D. Allan, D. Howe, and F. Walls, "Characterization of clocks and oscillators," NIST tech. note 1337, NIST, U.S Department of Commerce, National Institute of Standards and Technology, March 1990. online available at http://tf.nist.gov/cgi-bin/showpubs.pl.

[102] F. Krause, E. Benkler, C. Nölleke, P. Leisching, and U. Sterr, "Iodine-stabilized 633 nm diode lasers for metrology and interferometry (poster)," in *Joint Conference of the IEEE International Frequency Control Symposium and European Frequency and Time Forum (EFTF/IFC)*, (Orlando, FL, USA), IEEE, 2019.

[103] F. Krause, E. Benkler, C. Nölleke, P. Leisching, and U. Sterr, "Iodine-stabilized 633 nm diode lasers for metrology and interferometry (poster)," in *Conference on Lasers and Electro-Optics Europe & European Quantum Electronics Conference*, Optical Society of America, 2019.

[104] F. Krause, E. Benkler, and U. Sterr, "Extended-cavity diode laser at 633 nm stabilized to iodine using noise-immunecavity-enhanced optical heterodyne molecular spectroscopy (nice-ohms) (talk)," in *83. Jahrestagung der DPG und DPG-Frühjahrstagung*, 2019.

List of publications

- F. Krause, E. Benkler, C. Nölleke, P. Leisching, and U. Sterr, "Simple and compact diode laser system stabilized to Doppler-broadened iodine lines at 633 nm," *Appl. Opt.*, vol. 59, pp. 10808–10812, Dec 2020

- F. Krause, E. Benkler, C. Nölleke, P. Leisching, and U. Sterr, "Iodine-stabilized 633 nm diode lasers for metrology and interferometry (poster)," in *Joint Conference of the IEEE International Frequency Control Symposium and European Frequency and Time Forum (EFTF/IFC)*, (Orlando, FL, USA), IEEE, 2019

- F. Krause, E. Benkler, C. Nölleke, P. Leisching, and U. Sterr, "Iodine-stabilized 633 nm diode lasers for metrology and interferometry (poster)," in *Conference on Lasers and Electro-Optics Europe & European Quantum Electronics Conference*, Optical Society of America, 2019

- F. Krause, E. Benkler, and U. Sterr, "Extended-cavity diode laser at 633 nm stabilized to iodine using noise-immunecavity-enhanced optical heterodyne molecular spectroscopy (nice-ohms) (talk)," in *83. Jahrestagung der DPG und DPG-Frühjahrstagung*, 2019

Curriculum vitae

Name	Florian Krause
Address	Bleibtreuweg 2, 38106 Braunschweig
Date of Birth	13.09.1988 in Oldenburg
E-Mail	f_krause@gmx.de

Research

since 09/2016	**PhD Candidate**
	at Physikalisch-Technische Bundesanstalt (PTB)
	Working group: 4.31 Unit of length

Academic Education

10/20012 - 03/2016	**Physics Master of Science**
	at University of Potsdam
	Field of study: Optic and photonic
10/2009 - 09/2012	**Physics Bachelor of Science**
	at Carl von Ossietzky University Oldenburg
	Field of study: Optic and photonic

Acknowledgment

An dieser Stelle möchte ich allen danken, die mich während der Arbeit bei der PTB und der Anfertigung dieser Arbeit unterstützt haben:

- Als Erstes möchte ich mich bei meinem Doktorvater PD Dr. Christian Lisdat, meinen Gutachtern Prof. Dr. Piet O. Schmidt und Assoc. Prof. Dr. Jörg H. Müller und meinem Prüfungsvorsitz Prof. Dr. Klemens Hammerer bedanken.

- Ein besonderen Dank möchte ich Dr. Uwe Sterr für die Betreuung meiner Promotion aussprechen, der mir immer mit Rat und Tat zur Seite stand.

- Auch meinen Kollegen an der PTB möchte ich herzlichst für die Unterstützung, Diskussionen und Beantwortung meiner vielen Fragen während der Arbeit danken. Ein Dank geht an unsere E-Werkstatt bei der Unterstützung mit den elektronischen Komponenten. Ein weiterer Dank geht an unsere Werkstatt bei der Mithilfe der Planung und beim Bau der Cavity. Für die großartige Zusammenarbeit im Labor danke ich Erik Benkler, Clemens Budin und Thomas Legero.

- Ein ganz besonderer Dank geht an meinen langjährigen Büropartner und guten Freund Veit Dahlke für die gemeinsame und spaßige Zeit innerhalb und außerhalb der PTB.

- Für die organisatorischen Angelegenheiten, sei es in Zusammenhang mit der Promotion oder der Bürokratie innerhalb der PTB danke ich Frau Ohlendorf, Susanne Ehrenpfordt und Ute Krüger.

- Meinen Eltern Elviera und Ralf-Peter Krause möchte danken, dass sie mich während des Studiums und der Promotion immer unterstützt haben.

- Zum Schluss danke ich meiner Lebenspartnerin Alexandra Rommel, die mir beim Schreiben der Dissertation immer den Rücken gestärkt hat und immer ein offenes Ohr für mich hatte.